Measurement of the Gluon Density from Jet Rates in Deep Inelastic Scattering

Von der Mathematisch– Naturwissenschaftlichen Fakultät
der Rheinisch– Westfälischen Technischen Hochschule Aachen
genehmigte Dissertation zur Erlangung des akademischen Grades
eines Doktors der Naturwissenschaften

Vorgelegt von

Diplom-Physiker

Martin Hampel

aus Unna

Referent	:	Universitätsprofessor Dr. Ch. Berger
Korreferent	:	Universitätsprofessor Dr. S. Bethke
Tag der mündlichen Prüfung	:	21.02.1997

Für Susan

Everything should be made
as simple as possible.
But not more so.

Albert Einstein

Abstract

A new method is presented to determine the gluon density in the proton from jet production in deep inelastic scattering. By using the technique of Mellin transforms not only for the solution of the scale evolution equation of the parton densities but also for the evaluation of scattering cross sections, the gluon density can be extracted in next-to-leading order (NLO) QCD.

This method is, however, more general, and can be used in situations where a repeated fast numerical evaluation of scattering cross sections for varying parton distribution functions is required.

The Mellin transform technique is applied to a data set consisting of a luminosity of 2.74 pb^{-1} collected with the H1 detector in 1994 to extract the gluon density in NLO from (2+1) jet rates using the JADE algorithm. The momentum fraction domain of $\xi > 0.02$ is covered for this first direct extraction of the gluon density in NLO.

Contents

Chapter 1

Introduction

Since the begin of recorded history, humankind has striven to describe quantitatively the different ways in which matter appears and the forces that act between them by principles that can be experimentally tested and thus to find a starting point to understand nature. In recent times, especially in modern physics of the 19th and 20th century, a more precise and consistent picture of matter has evolved that reaches from the atomic model up to elementary particle physics, the limit of today's knowledge within this area. Here, the theory of relativity on one side and quantum theory on the other play an important role. In modern field theories, special relativity and quantum theory are treated in a common formalism [1, 2, 3].

Today, the so-called "Standard Model" is widely accepted as a description of matter that treats three of the four known forces in a unified way, although more questions must still be answered. Because this model is covered in many textbooks [4, 5, 6, 7], only a cursory discussion will be given here. The "fourth force," gravity, which is described by general relativity, could not be unified with the Standard Model up to now and thus will not be dealt with in the following.

Within quantum theory, which is a precondition for the understanding of processes at very small distances, the concept of interaction replaces the one of force, since here the force between particles is mediated by the exchange of "force quanta." The theoretical machinery of the standard model describes the particles that exist within that model and their interactions. It consists of the fundamental building blocks of matter, as we know them today, leptons and quarks, as well as gauge bosons (spin 1) that mediate interactions. Leptons and quarks are particles of spin 1/2 (fermions) and are classified into left-handed doublets following a $SU(2)$-symmetry group and right-handed singlets, respectively. They are summarized in table 1.1, where the different types of quarks are also denoted as "flavors."

The *top*-quark was recently discovered at Fermilab, Chicago, USA [8, 9] after a search that lasted several decades and involved many different experiments.

The three "forces" within the Standard Model are the strong, the electromagnetic and the weak interaction. The last two are unified to the electroweak interaction, which occurs as well for leptons as for quarks. The corresponding gauge bosons are named γ for the electromagnetic and $W^{\pm}$ and Z^0 for the weak interaction. In the case of γ and Z^0, there are interference terms that do not play an important role except for very high momentum transfers due to the high mass of the Z^0. Their group representation is $SU(2) \times U(1)$. The exchange of a γ or Z^0 is often referred to as neutral current, and $W^{\pm}$ exchange as charged current.

In contrast, the strong interaction does only occur between quarks and gluons. The "charge" of the strong interaction is a state with three degrees of freedom, which is described by "color" in the jargon of the Standard Model, and that are called "green," "blue" and "red," moti-

Leptons:

$$\begin{pmatrix} \nu_e \\ e^- \end{pmatrix}_L \quad \begin{pmatrix} \nu_\mu \\ \mu^- \end{pmatrix}_L \quad \begin{pmatrix} \nu_\tau \\ \tau^- \end{pmatrix}_L$$

$$e^-_R \qquad \mu^-_R \qquad \tau^-_R$$

Quarks:

$$\begin{pmatrix} u \\ d \end{pmatrix}_L \quad \begin{pmatrix} c \\ s \end{pmatrix}_L \quad \begin{pmatrix} t \\ b \end{pmatrix}_L$$

$$\begin{matrix} u_R & c_R & t_R \\ d_R & s_R & b_R \end{matrix}$$

Table 1.1: Classification of leptons and quarks in the Standard Model.

vated by the theory of colors in optics. The exchange particles, the "gluons," carry one color and one anticolor, whereas the representation of the group $SU(3)_C$ describes the combinatorial possibilities of the color states and thus allows for eight different "sorts" of gluons. Due to the non-Abelian nature of the $SU(3)_C$, gluons also interact with each other.

In total, the symmetry group of the Standard Model can be described as the direct product $SU(3)_C \times SU(2) \times U(1)$ of three groups.

Of all the field theories, **Q**uantum **E**lectro **D**ynamics (QED) and **Q**uantum **C**hromo **D**ynamics (QCD) are probably best understood. Due to the fact that the QED coupling constant of the electromagnetic interaction α has a very small value of about 1/137 and can therefore be very well treated in a perturbative approximation by series expansion for relatively large distances, this region was measured with high precision.

Within QCD, the coupling increases with increasing distance due to the non-Abelian gauge group $SU(3)_C$. Thus at some point the binding energy reaches a value that enables new particle-antiparticle-pairs, making it principally impossible to observe free quarks. Demanding states neutral in color means immediately that matter can only appear as so-called "baryons" with three quarks (to which also the proton (uud) and the neutron (udd) belong) or as "mesons" with a quark and an antiquark. Higher combinations are also possible, as well as pure gluon states, the so far unobserved "glueballs." Also called "confinement," this implies in contrast that quarks are virtually free at small distances ("asymptotic freedom").

In this region of asymptotic freedom, a perturbative series expansion is more difficult than in QED. The QCD coupling constant α_S has a larger value at energies that can be reached with today's accelerators, thus reducing the convergence of the series. The color charge of the gluons induces self-interactions in correlation to the non-Abelian character of the $SU(3)_C$ and contributes with additional terms. As soon as the asymptotically free region is left, the coupling increases and makes a perturbative treatment no longer possible. Nevertheless, the progress in the last two decades enabled a good understanding of the QCD processes at small distances.

In order to test the theoretical predictions of the Standard Model and also determine its parameters more exactly, or to have the opportunity to look for "new physics," scattering experiments at particle accelerators and colliders are conducted. Here the scattering of electrons off protons is an interesting option, since electrons are leptons and do not interact strongly, they therefore are able to test the structure of the proton very cleanly.

At the "**D**eutsches **E**lektronen **Sy**nchrotron" DESY in Hamburg, Germany, the "**H**adron-

Elektron-**R**ing-**A**nlage" HERA investigates this type of scattering.[1] Its circumference is 6.3 km and it has two detectors, "H1" and "ZEUS" located at interaction points to detect the particles emerging from collisions. Two additional experiments, "HERMES" and "HERA-B" cover spin physics and b meson physics, which will not be discussed here. A picture of the ring can be found in figure 1.1, and the detector H1 is displayed in figure 1.2.

This thesis is organized as follows: After a short picture of the motivation to measure the gluon density in chapter 2, the theoretical foundations will be laid in chapter 3. The mathematical formalism to overcome the CPU time problem induced by the need to fit the gluon density used here is covered in chapter 4. Then HERA and H1 will be described in chapter 5, after which the Monte-Carlo-Machinery necessary to analyze data is introduced in chapter 6. All this is applied in chapter 7 for the event selection and the display of results in chapter 8. Finally, a conclusion and outlook is given in chapter 9. Several technical appendices terminate the thesis.

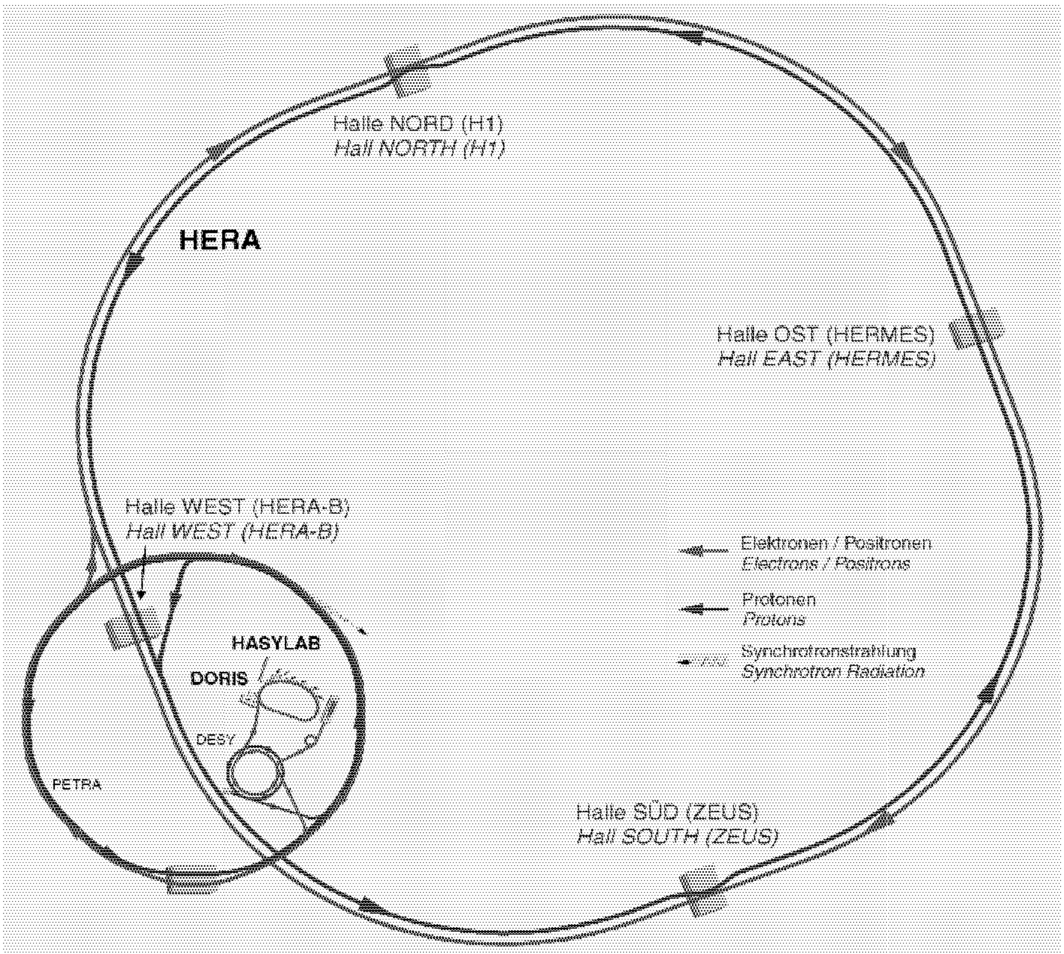

Figure 1.1: The HERA ring.

[1] First collisions were observed in 1991. Since then, the recorded luminosity has increased steadily up to about 4 pb^{-1} in 1994. In 1995, another 5 pb^{-1} of data was taken.

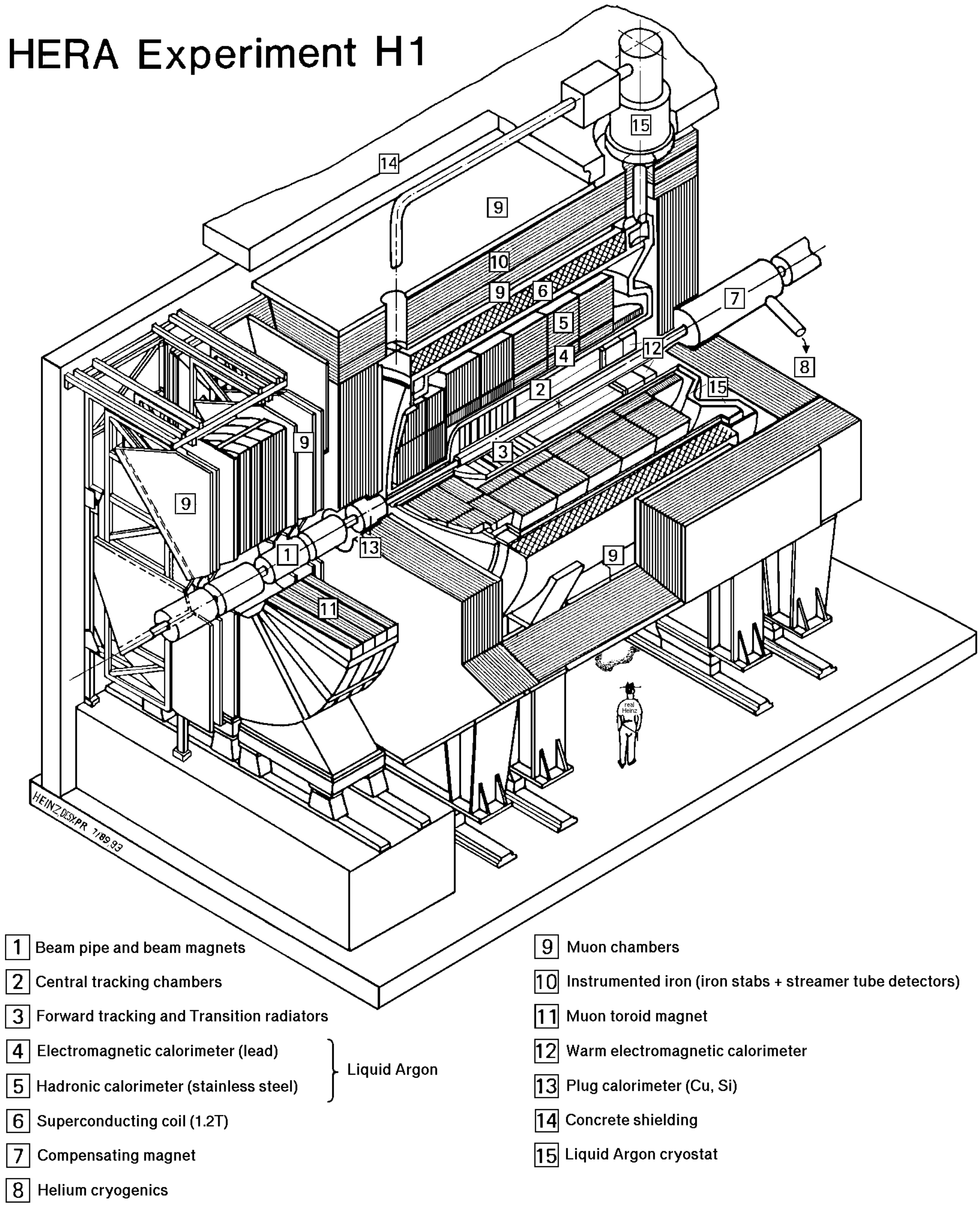

Figure 1.2: The H1 detector.

Chapter 2

Motivation

2.1 HERA and H1 Physics

The electron-proton collider HERA, which has been producing collisions since 1991, provides the opportunity to cover a wide variety of physics. As was outlined in chapter 1, the electron that probes the structure of the proton does not interact strongly. Therefore, it provides a clean testing ground for QCD and structure functions.[1]

HERA is the first collider of this kind, and in contrast to fixed-target experiments, where the hadron (here the proton) is at rest, the protons are accelerated to 820 GeV and hit the electrons (or positrons, respectively), which have an energy of 27.5 GeV, thus amounting to a center-of-mass energy of about 300 GeV. This is equivalent to a fixed-target experiment with an electron energy of 50 TeV. Clearly, the kinematic range covered here is unique, and allows the determination of the proton structure down to $\mathcal{O}(10^{-18}\mathrm{m})$.[2]

For charged current processes, the exchanged $W^{\pm}$ results in the production of a neutrino, which escapes detection. This is an interesting type of physics, and mainly deals with electroweak effects. However, we will concentrate on neutral current exchange. As the kinematic region of interest does not produce a sizeable contribution from Z^0, we will refer to the exchanged boson as the photon γ.

Depending on the absolute virtuality of the exchanged boson, Q^2, three regions can be distinguished. For quasi-real photons, Q^2 is almost zero and constitutes the region of *photoproduction*. Here, the photon can interact either directly with the proton's constituents or show its hadronic structure. Therefore, an abundance of physical questions can be investigated such as the structure of the photon as well as scattering phenomena originating from proton structure.

If Q^2 gets larger (starting at a few GeV^2), one enters the region of **D**eep **I**nelastic **S**cattering (DIS) after a transition range. Due to the increased virtuality of the photon, only the direct contribution accounts, so that a precise test of the constituents of the proton can be made. For example, the proton structure function F_2 can be measured by detecting the scattered electron. This inclusive measurement has been performed with increasing precision [10].

On the other hand, energy flows can be measured and jet physics can be pursued, i.e. taking an exclusive approach. As will be shown later, this allows for the measurement of α_S and the gluon density and provides thus a very sensitive test of perturbative QCD and increases the precision with which these fundamental quantities are known.

[1] The formal concept of the physical quantities mentioned here is developed in chapter 3.

[2] A more detailed discussion of HERA and H1 can be found in chapter 5.

Recently, also *rapidity gaps* have been observed and led to interesting physics [11]. Furthermore, searches for physics beyond the Standard Model have been conducted, as its numerous free parameters hint for a structure of nature beyond it [12, 13]. But so far, the Standard Model has been shown to describe the known phenomena with stunning precision.

An overview over the various physics subjects that are investigated at HERA can be found in [14, 15, 16].

2.2 The Gluon Density

It has been known for a long time that the quarks carry only about half of the proton's momentum, and that gluons account for a large part of the rest [5, 6, 7]. Historically, the parton densities were introduced to describe the probability of quark flavors and gluons to be found in the proton for a certain kinematical region of the scattering. They can be linked to the structure function F_2.[3]

Therefore, an exact knowledge of the gluon density is very important for the description of the proton structure in the light of perturbative QCD. As will be explained later, cross sections consist of a convolution involving the hard subprocess, which can be calculated perturbatively, and parton densities. The divergent part of the cross section calculation can be absorbed in these parton densities and leads to scale dependences. By providing a parameterization, the probability distribution of quarks and gluons can be obtained. As this cannot be calculated *ab initio*, the only way to determine them is the measurement in an experiment.

To higher orders of perturbative QCD, the simple probabilistic picture no longer holds, and a more formal concept has to be followed. It is important to note that explicit scale dependences are reduced in higher orders, and that therefore a determination of the parton densities in **N**ext to **L**eading **O**rder (NLO) is highly desirable.

Apart from the importance in its own right of knowing the gluon density in the proton and thereby understanding proton structure better, applications for future collider design are noteworthy.

One important channel in the search for the *Higgs*-Boson H in hadron collisions is the gluon-gluon fusion process, where two gluons form a H in a heavy quark loop [7]. Clearly, the gluon density enters quadratically in the calculation of the cross section, and a relatively small uncertainty in the gluon density can transform into a huge difference in the cross section. This makes an improved knowledge of the gluon density very interesting for the design of the **L**arge-**H**adron-**C**ollider (LHC) at CERN in Geneva, Switzerland.

So far, different ways to determine the gluon density have been pursued. The most important technique is the use of sum rules in global parton density fits by combining data of numerous experiments. While these fits provide the most complete analysis of world data, they rely on assumptions and can thus constrain the gluon density only indirectly. These fits are currently performed essentially by three different groups, named GRV, CTEQ and MRS [17, 18, 19], and the parameterizations are available in the computer library PDFLIB [20].

Some of the most common parton density parameterizations of the proton are plotted in figure 2.1 for a scale of $Q^2 = 20$ GeV^2. The familiar behaviour of the valence and sea quarks can be seen clearly. The ratios of the parameterizations with the set "MRSG" are shown in

[3] See section 3.3.

figure 2.2 to illustrate the level of uncertainty.[4] Since all global fits use similar sets of data, the results are highly correlated, of course, and the uncertainty is larger than suggested by the plots.

The same parameterizations and relations for the gluon density are shown in figure 2.3. As can be seen, the deviations between the parameterizations are much larger, reinforcing the statement that the gluon is less well known than the quarks. The ratios in the lower plot also show nicely the correlations, i.e. the same qualitative behaviour, stressing the underestimation of uncertainty by the parameterization ratios.

Other measurement methods involve prompt photons produced in hadron collisions by the "Compton-like" subprocess $qg \to \gamma q$. Although this method is direct, it covers mainly the high momentum fraction ξ domain. A recent investigation [21] shows that there is still considerable uncertainty about the size of the gluon density. Therefore, new and more precise measurements of the gluon density are highly desirable.

In recent years, the gluon density was determined using the scaling violation behaviour of F_2 [10], see figure 2.4. This is another indirect measurement, covering rather low ξ values. The ξ region between 0.01 and 0.1 is still not constrained by a dedicated measurement [22].

A direct measurement of the gluon density $g(\xi, \mu_f^2)$ is very much needed. In ep scattering, one can use the fusion of γ and a gluon from the proton, observing the produced particles. This could be a heavy meson, i.e. a heavy quark-antiquark pair. In photoproduction, the hadronic structure of the exchanged photon makes the formation of this heavy meson still very model dependent, and thus a measurement cannot extract the gluon density properly [23]. One alternative would be the direct interaction in *electroprodution*, i.e. at larger virtualities of the exchanged photon. The statistics gathered with this type of interaction so far has not been sufficient to justify an extraction of the gluon density.

The alternative process that is interesting here is the **B**oson-**G**luon-**F**usion (BGF) in DIS, where not mesons are formed, but jets can be observed in the detector. Analyzing these jets can be used to determine the gluon density, provided one knows the competing *QCD-Compton* process well enough to take it into account. A **L**eading **O**rder (LO) determination has been performed by H1 [24].

The idea pursued in this thesis is a NLO measurement of the gluon density using (2+1) jets.[5] As will be shown below, in NLO one cannot correct back to the incoming gluon momentum fraction experimentally anymore, and only a determination via a fit is possible.

The (2+1) jet cross section can be generically written as:[6]

$$\mathrm{d}\sigma_{(2+1)} \sim \left(\mathrm{d}\hat{\sigma}_C \sum_i q_i(\xi, \mu_f^2) + \mathrm{d}\hat{\sigma}_F g(\xi, \mu_f^2) \right) \tag{2.1}$$

This observable can be used to determine the gluon density.[7] In the kinematic region under investigation here, the quark densities are well constrained, and α_S is taken as known.

[4] The c quark ratio for GRV was not plotted, because it is not available directly, but has to be generated dynamically.

[5] A jet can essentially be regarded as energy deposits in the detector stemming from hadronic interactions that are grouped according to a jet algorithm and corrected back to parton level.

[6] Here, $\mathrm{d}\hat{\sigma}_C$ and $\mathrm{d}\hat{\sigma}_F$ denote the hard QCD-Compton and BGF subprocesses, respectively, while $q_i(\xi, \mu_f^2)$ and $g(\xi, \mu_f^2)$ stand for the quark densities and the gluon density. They depend on parton momentum fraction ξ and the factorization scale μ_f^2. See chapter 3.

[7] Strictly speaking, jet rates are used; but this concept will be introduced later, and the underlying idea of the measurement is the same.

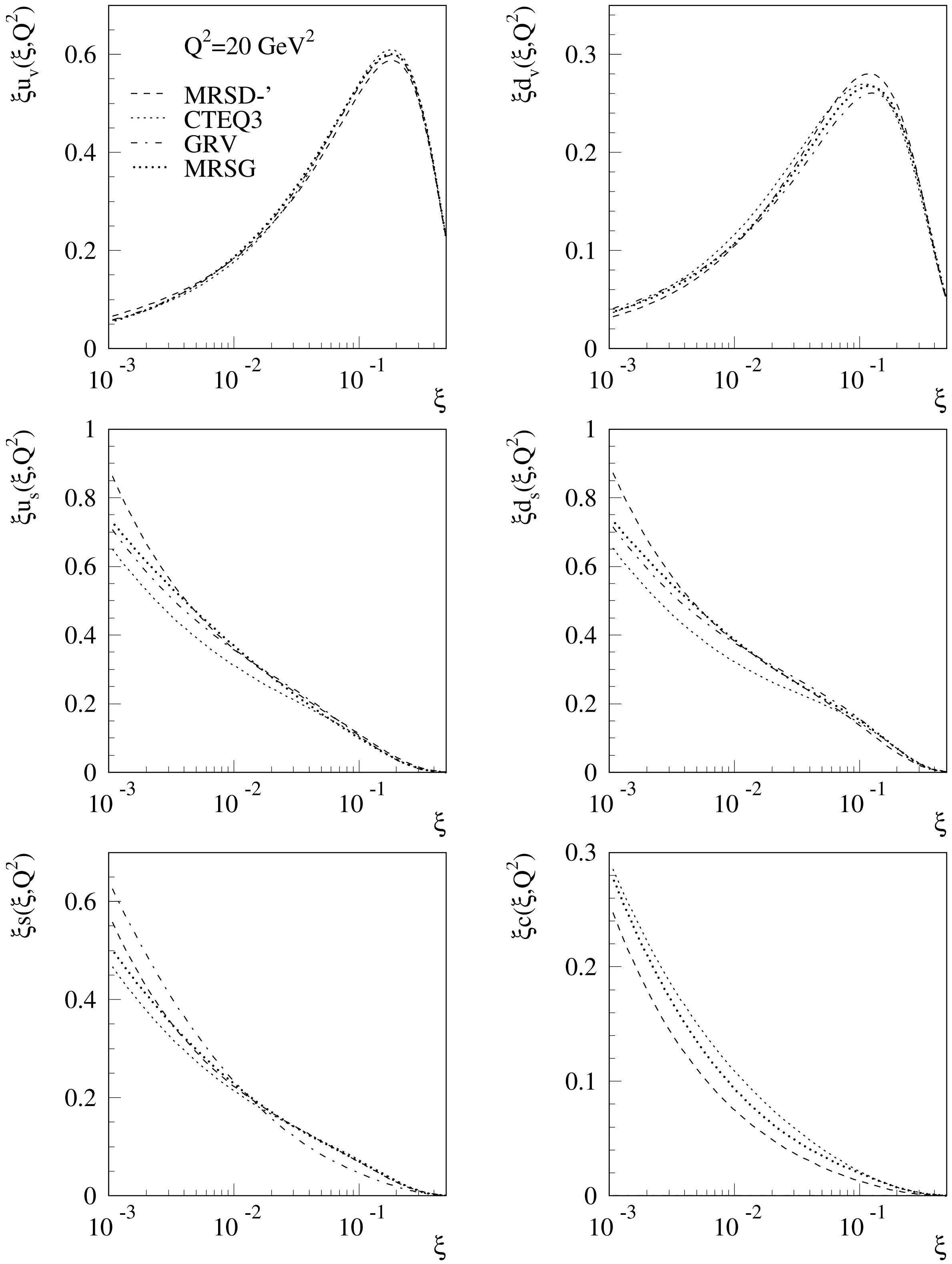

Figure 2.1: Comparison of common quark density parameterizations of the proton for a scale of $Q^2 = 20$ GeV^2. The index v denotes valence quarks, while s stands for the sea quark contribution. Note the different ordinate scales!

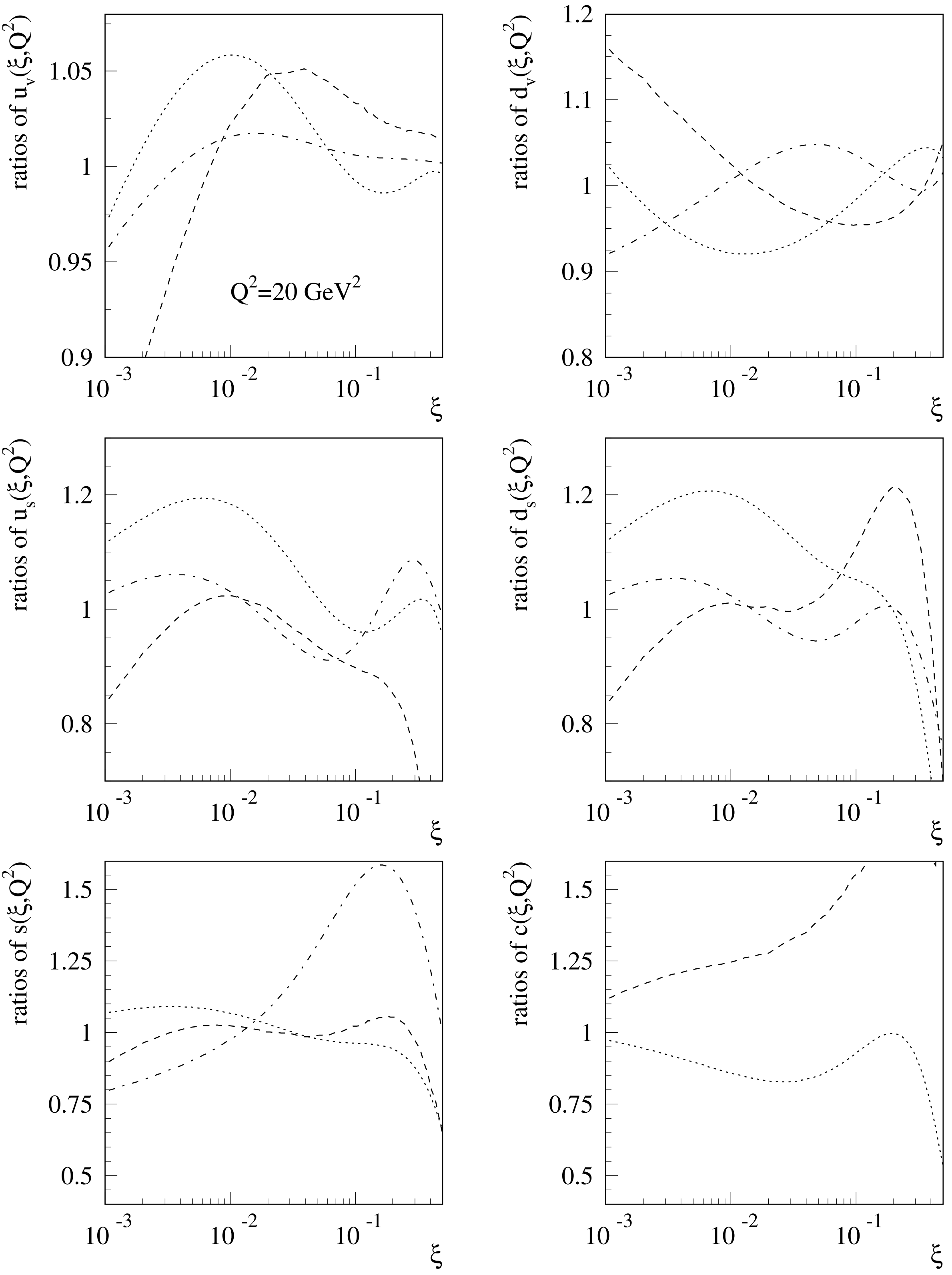

Figure 2.2: Ratios of common quark density parameterizations relative to the set MRSG. The line types are the same as in figure 2.1. Note the different ordinate scales!

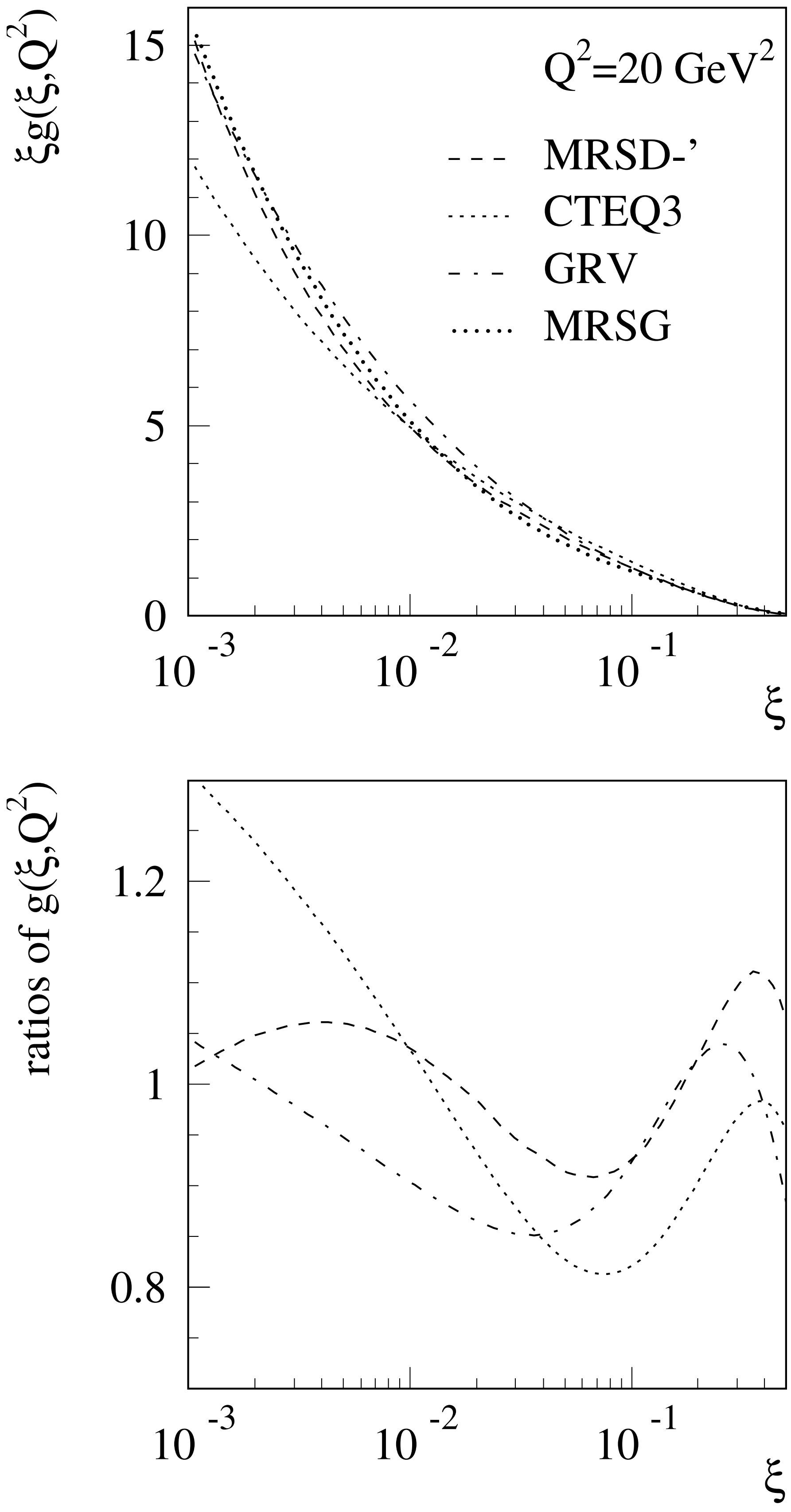

Figure 2.3: Comparison of common gluon density parameterizations (top), and ratios relative to the set MRSG (bottom). Note the different ordinate scales!

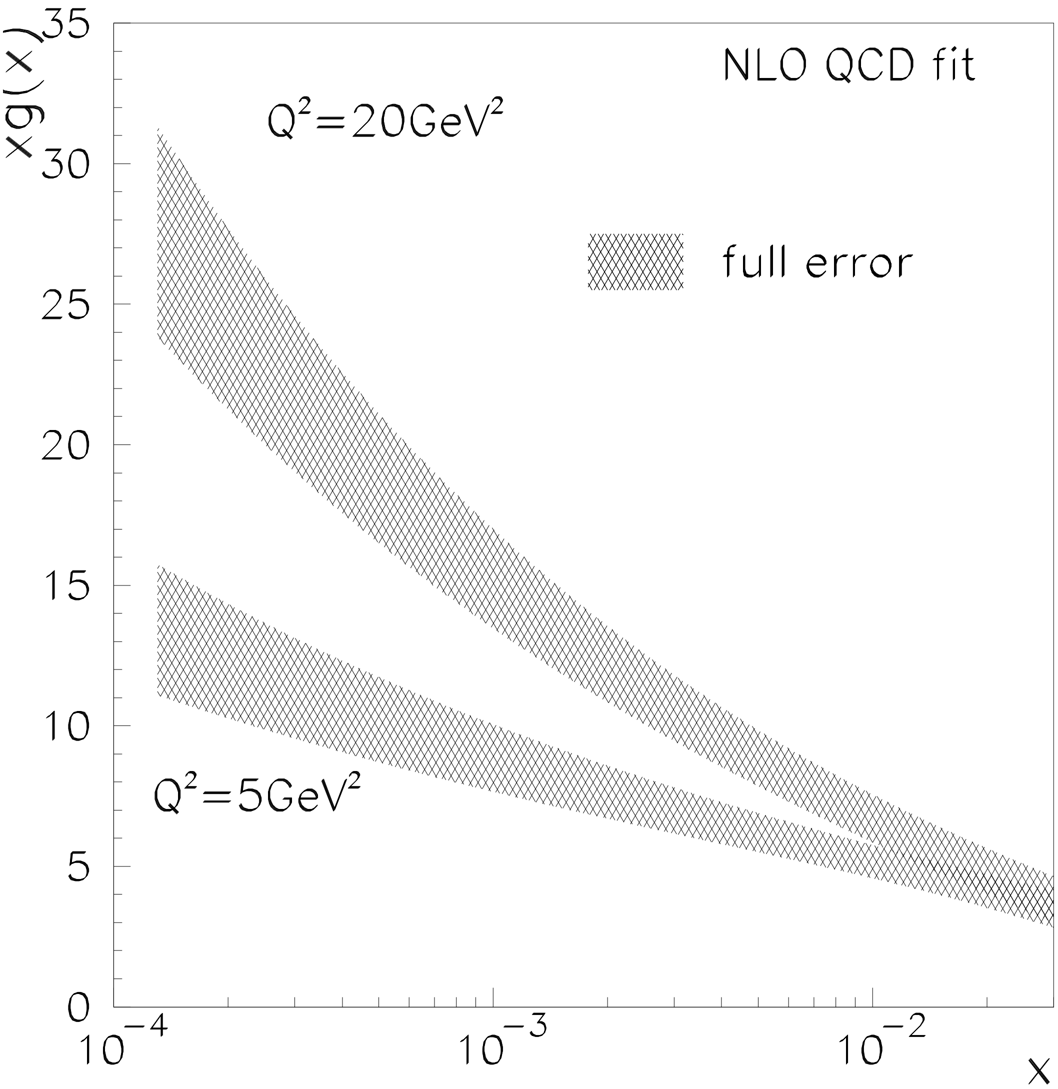

Figure 2.4: The gluon density from scaling violation of F_2; taken from [10].

The employment of the JADE jet algorithm in this analysis restricts the ξ region to between 0.01 and 0.1, which is therefore complementary to the other determinations mentioned. The lower bound stems from the jet definition parameter y_{cut}, since $\xi > y_{cut}$. By the use of different jet algorithms, one will also be able to access lower ξ. The restriction to higher ξ values is imposed by the lack of data in that region and will be reduced with higher luminosity. Both constraints in ξ are not induced by the method itself and can be overcome.

The principle can be turned around, and one can take the parton densities as known, and determine α_S. This has been done already [25], see figure 2.5. (For an overview of α_S determinations, see [26].) In the future, it will be possible to combine both analyses, thus enabling the determination of α_S and $g(\xi, \mu_f^2)$ simultaneously.

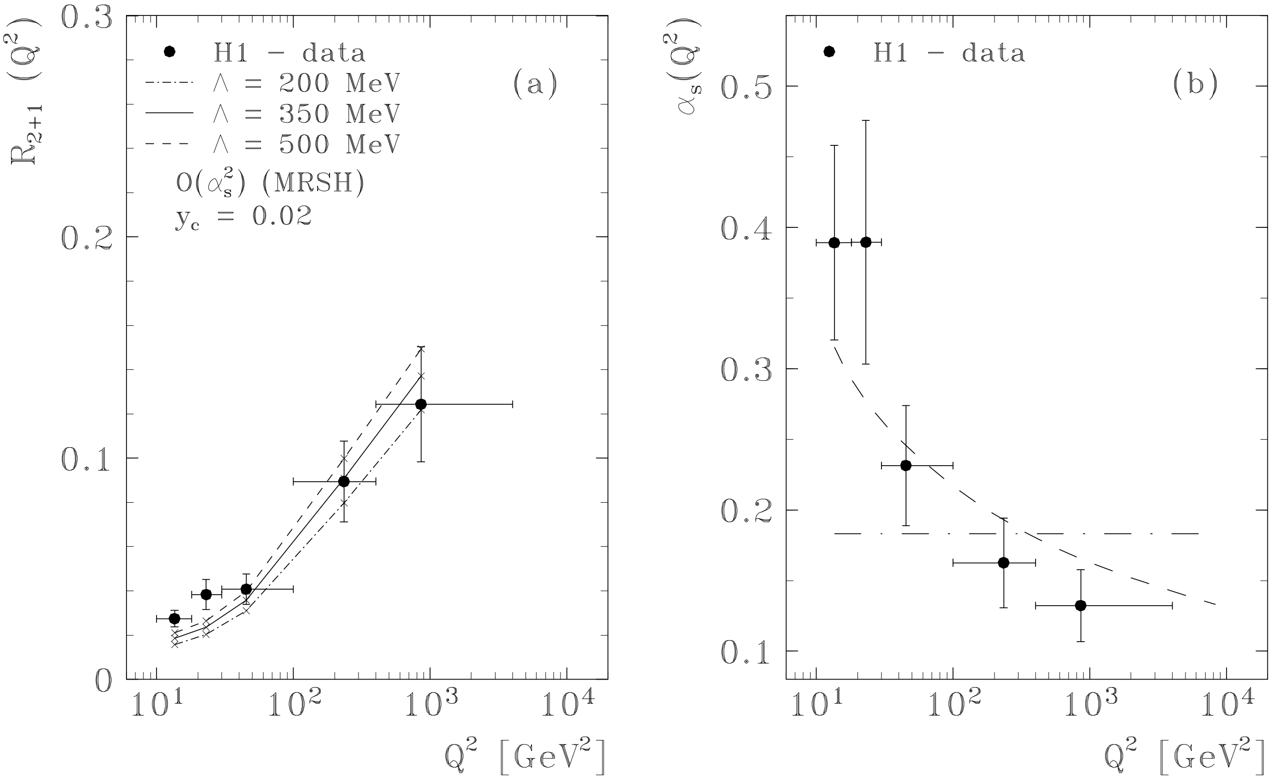

Figure 2.5: (2+1) jet rate (a) and α_S from jets (b); taken from [25]. The lines in (a) illustrate the prediction by the renormalization group equation, the lines in (b) denote the fit to data assuming a running α_S and a scenario with a constant coupling. Only statistical errors are shown.

Chapter 3

Theoretical Overview

All known phenomena observed in elementary particle physics can be explained by the theoretical concepts of quantum field theory, which are used within the Standard Model. The interactions are derived from local gauge invariances of the Lagrangian $\mathcal{L}$ and the application of a quantization procedure of the underlying theory. The request for local gauge invariance results in the formulation of rules for the determination of interaction probabilities. They are analogous to interaction strengths, as in quantum theories only statistical and no deterministic statements can be made.

It can be shown that QED is described by the Lagrangian [5]:

$$\mathcal{L}_{QED} = \overline{\psi}(i\gamma^{\mu}\partial_{\mu} - m)\psi + e\overline{\psi}\gamma^{\mu}A_{\mu}\psi - \frac{1}{4}F_{\mu\nu}F^{\mu\nu} \tag{3.1}$$

Here, ψ denotes a spinor, the γ^{μ} are the Dirac-matrices, e is the charge, m the particle mass, and the four vector potential A_{μ} describes the gauge field of the group $U(1)$, where the field strength tensor is $F_{\mu\nu} = \partial_{\mu}A_{\nu} - \partial_{\nu}A_{\mu}$.

The QCD Lagrangian is [5]:

$$\mathcal{L}_{QCD} = \overline{q}(i\gamma^{\mu}\partial_{\mu} - m)q - g(\overline{q}\gamma^{\mu}T_{a}q)G^{a}_{\mu} - \frac{1}{4}G^{a}_{\mu\nu}G^{\mu\nu}_{a} \tag{3.2}$$

In this equation, q is the quark color field, T_a are the generators of the $SU(3)_C$, and the field strength tensor G describe the associated gauge field.

The weak interaction shall be neglected, as it does not play an important role in the processes of deep inelastic scattering covered in this thesis.[1]

By conducting an experiment, one is, of course, not able to measure the field-theoretical concepts directly, but one can only determine event rates within a certain phase space region. These rates have to be predicted by theory and thus enable a quantitative verification. Historically, the concept of the *cross section* σ evolved which is defined by the number of events N produced by the luminosity L of an experiment:

$$N = L\sigma \tag{3.3}$$

From the field-theoretical point of view, σ contains two components. One is the phase space factor which basically takes into account the number of possible final states of the reaction per energy, but also comprises kinematical contributions. The other is the square of the modulus of

[1] As mentioned before, the contribution to the cross section by the intermediate Z^0 boson is highly suppressed due to its large mass in the kinematical region under investigation.

the scattering matrix element $\mathcal{M}$ which can be derived from the rules mentioned above. To honor Richard P. Feynman, who invented them, they are called *Feynman rules.* A very interesting aspect is not only the mathematical use, but the intuitive meaning of the Feynman graphs set up according to these rules, which illustrate the reaction clearly. One has to be careful, however, to always keep the theoretical meaning in mind in order not to fall for simplistic arguments.

In a symbolic notation, the relation between $\mathcal{M}$ and the differential cross section $\mathrm{d}\sigma$ can be expressed with the Lorentz-invariant phase space factor $\mathrm{d}Lips$ and a flow factor F as [5]:

$$\mathrm{d}\sigma = \frac{|\mathcal{M}|^2}{F}\mathrm{d}Lips \tag{3.4}$$

Thus σ is the integral of $\mathrm{d}\sigma$ over all kinematic variables. To calculate the cross section, one can conduct perturbative calculations in phase space regions, where the coupling constant is small. The matrix element is considered as a series in the coupling constant; typically within QED this is the fine structure constant α, and in QCD the strong coupling constant α_S. The bare cross sections are ultraviolet-divergent but can be renormalized in any order.

3.1 Kinematics at HERA

In order to test the proton structure, scattering reactions of electrons off protons are particularly well suited, since the electron reacts only electroweakly, whereas the quarks of the proton can couple also strongly.[2] This enables clean tests of QCD, because the behaviour on the electron is well understood, and therefore theoretical uncertainties can be kept small. In order to describe a reaction, kinematical variables are used, which are defined preferably as Lorentz-invariant, so they can be used in all reference frames. Here, always unpolarized particles are assumed.

The four vector used for the kinematical description is of the form:

$$p^\mu \equiv (E, \vec{p}) \tag{3.5}$$

The square of a four vector, the invariant mass square, is defined as:

$$p^\mu p_\mu = p^2 \equiv m^2 = E^2 - |\vec{p}|^2 \tag{3.6}$$

In the high energy approximation, which is valid in the kinematical region under consideration, the particle masses can be neglected. Only the proton mass ($m_P = 938$ MeV [27]), being three orders of magnitude larger than the electron mass ($m_e = 0.511$ MeV), is sometimes taken into account. Thus the invariant squared center of mass energy s (with incoming proton four momentum vector P, massless) is given by

$$s = (p_e + P)^2 \approx 4E_e E_P. \tag{3.7}$$

On the electron side, a photon is radiated and participates in the hard scattering subprocess, as depicted in figure 3.1. Its four momentum $q = (p_e - p_{e'})$ is spacelike and thus the invariant q^2 negative. Therefore one defines:

$$Q^2 \equiv -q^2 = -(p_e - p_{e'})^2 \approx 2E_e E_{e'}(1 + \cos\theta_{e'}) \tag{3.8}$$

[2]In the following, the term "electron" will be used generically for both electrons and positrons. Even though a large part of the 1994 data sample was collected with positrons, the underlying jet physics is the same.

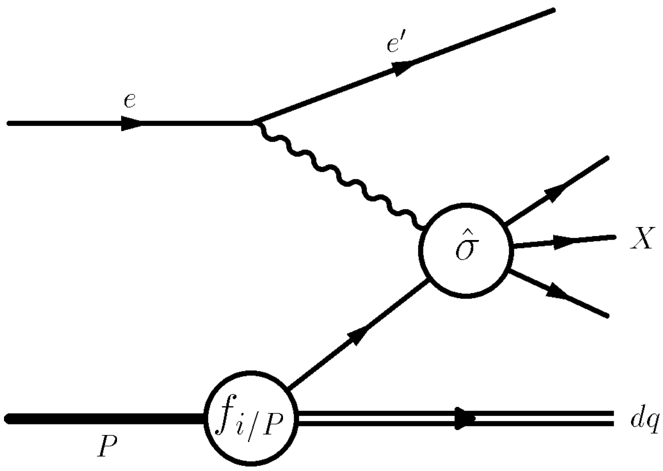

Figure 3.1: Generic graph for DIS reactions.

Here, $\theta_{e'}$ is the angle between the incoming proton- and scattered electron three momentum vector (H1 convention).

Furthermore, the invariant scale variable Bjorken-x and the the variable y are important, which are defined by products of four momenta fulfilling $0 \leq (x, y) \leq 1$:

$$x \equiv \frac{Q^2}{2P \cdot q} \tag{3.9}$$

$$y \equiv \frac{P \cdot q}{P \cdot p_e} \tag{3.10}$$

The invariant mass W of the hadronic system lies between m_P and $\sqrt{s}$:

$$W^2 \equiv (q + P)^2 = Q^2 \frac{1 - x}{x} + m_P^2 \tag{3.11}$$

From these quantities one can derive a relation that is convenient for further consideration:

$$Q^2 = 2xyp_e \cdot P = xy(s - m_P^2) \approx xys \tag{3.12}$$

Additional quantities will be introduced in the course of the thesis in order to describe the hard subprocess and the kinematics associated with it.

3.2 Kinematical Reconstruction

An overview of the kinematical situation at HERA energies is given in figure 3.2. Isolines of the following quantities are plotted in the (x, Q^2) plane:[3]

E_e	Energy of the scattered electron
θ_e	Polar angle of the scattered electron
E_T	Transverse energy of the scattered electron
E_J	Energy of the struck quark as computed in the Parton Model
θ_J	Polar angle of the struck quark as computed in the Parton Model
W^2	Square of the invariant mass of the hadronic final state

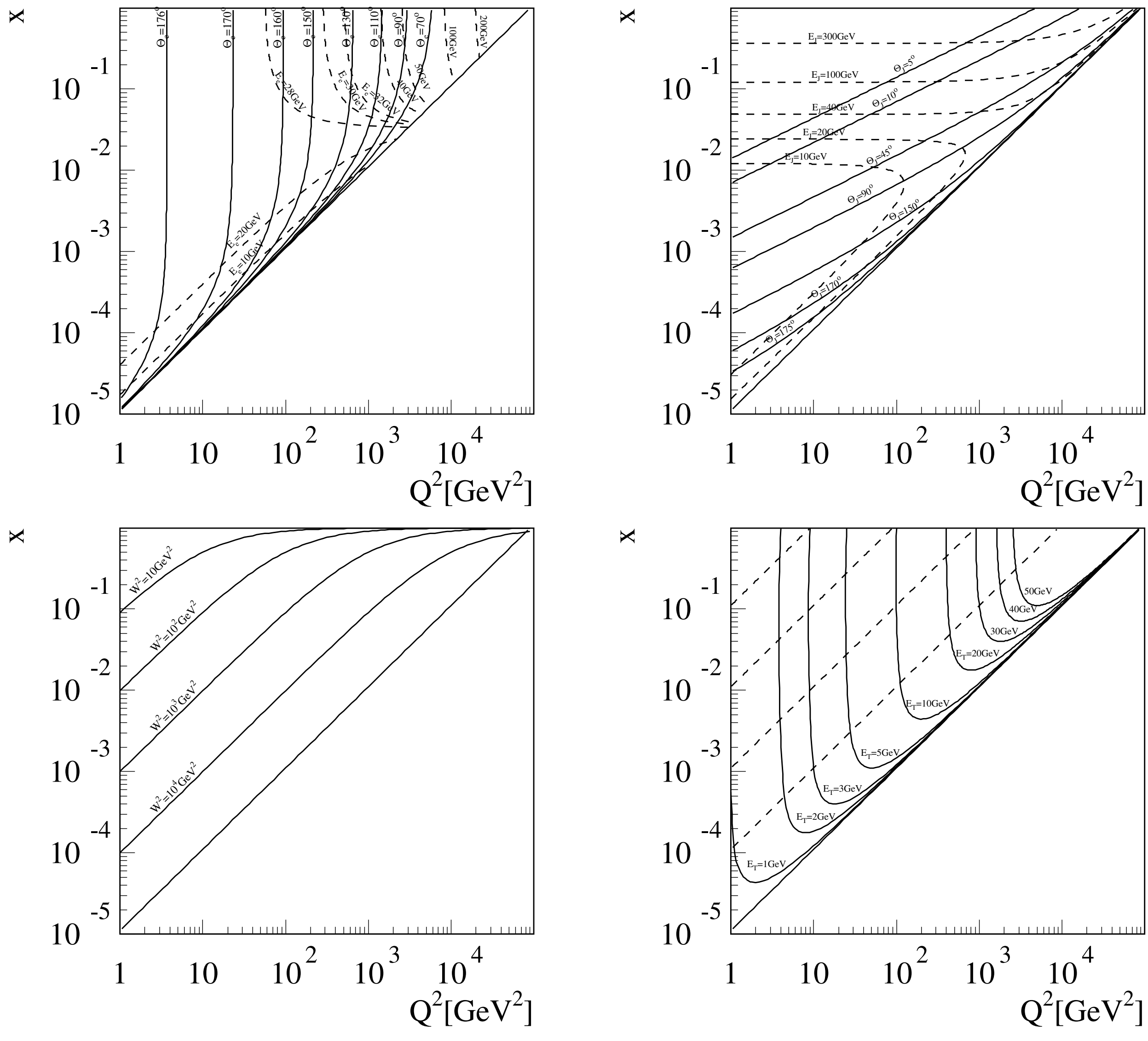

Figure 3.2: Isolines of kinematical quantities in the (x, Q^2) plane. The definition of the quantities can be found above the figure. In the lower right plot, the dashed lines constitute lines of constant y. Note that the nomenclature E_e, θ_e and θ_J is used in this plot only!

[3]The primes " ' " are left out in this figure for better readability.

The reconstruction of the basic kinematical variables can be achieved in different ways by using different measured quantities, since the system is overconstrained. Depending on the variable under consideration, the optimal method can be different. A discussion of useful reconstruction methods can be found in [14, 28, 29]. Only a short overview will be given now for the methods used in this analysis.

A general procedure is to measure y and Q^2 first and derive the other quantities from there. Using the *electron-only method*, one finds:

$$y_e = 1 - \frac{E_{e'}}{E_e} \sin^2 \frac{\theta_{e'}}{2} \tag{3.13}$$

$$Q_e^2 = 4 E_e E_{e'} \cos^2 \frac{\theta_{e'}}{2} \tag{3.14}$$

This method gives a very good Q^2 reconstruction and a good reconstruction of x for higher y, with a rapid degradation at low y because of equation 3.12.

Using the angles of the scattered electron and of the struck quark θ_{jet} (assumed to be given in the QPM, i.e. using all hadronic clusters in the detector and determining from them the angle θ_{jet}), the *double angle method* yields:

$$y_{da} = \frac{\sin\theta_{e'}(1-\cos\theta_{jet})}{\sin\theta_{jet} + \sin\theta_{e'} - \sin(\theta_{e'}+\theta_{jet})} \tag{3.15}$$

$$Q_{da}^2 = 4E_e^2 \frac{\sin\theta_{jet}(1+\cos\theta_{e'})}{\sin\theta_{jet} + \sin\theta_{e'} - \sin(\theta_{e'}+\theta_{jet})} \tag{3.16}$$

This method is more suited to reconstruct x. Mixtures of both and other methods can be applied to optimize the quality of the reconstruction.

3.3 Cross sections

In deep inelastic scattering of electrons off protons a series expansion is performed within QED and QCD. The expansion is performed in α and α_S, assuming that the chosen dynamical region in the quark phase space can be seen as one where the quark is "asymptotically free" and thus can enable a perturbative description. The expansion in α is done only to $\mathcal{O}(\alpha)$. As two parameters have to be taken into account simultaneously, a closer look at the series is in order.

In figure 3.1, the principal topology of deep inelastic scattering was shown already. We are primarily concerned with the exchange of a photon (or Z^0) with a quark of the hadronic system.[4]

In the QPM, one can picture the proton to move with an infinite momentum (therefore the frame is often denoted by "infinite momentum frame"), thus "freezing" the quarks and gluons in their state when hit by the electron. The partons are essentially moving in parallel and have (almost) no transverse momentum with respect to the beam axis. This can be motivated by the Lorentz-contraction, yielding a "disk-like" proton and can be regarded as a very good approximation for HERA energies. Then, the interactions that occur between the quark and electron before the collision can be neglected and one can assume that only one quark participates in the hard subprocess. The other constituents of the proton essentially function as "spectators" and are not influenced much by the primary collision.[5] In the QCD improved QPM, higher orders can be calculated.

[4] A somewhat closer look at radiative corrections will be given in section 6.4.

[5] The spectator quarks are denoted by "dq" in the Feynman graphs.

After the hard interaction, the participating partons move with large transverse momenta with respect to each other. Once they reach the distance of about 1 fm, the asymptotic freedom is not valid anymore and the color forces between the proton remnant and the other hadronic components become large. As within these particles, transverse momenta persist, they continue to break up into new particles, until the prevailing energy does not suffice anymore. This constitutes "fragmentation." Following the color flow, the particles group to "white" units and form hadrons. A "jet" emerges that can be recorded in the detector.

In figure 3.3, the process to order α_S^0 in QCD is pictured. To order α_S, the two generic Feynman diagrams are displayed in figures 3.4 and 3.5, the so called "QCD-Compton-" and "Boson-Gluon-Fusion-"graph, respectively. The LO cross sections are given in [30], and a discussion of this LO cross section can be found in [31]. Therefore, the different terms of the cross section will be discussed only briefly here.

The complete cross section is formed by integrating over the differential cross section in the phase space region under consideration. The differential cross section, in turn, is a product of the flow factor Γ_t for the transversal polarization of the exchanged photon induced by the electron, the hard subprocess $\hat{\sigma}$ and the parton densities $f_{i/p}$, i.e. q_i and g:[6]

$$\frac{\mathrm{d}\sigma_{QPM}}{\mathrm{d}y\,\mathrm{d}Q^2} = \frac{2\pi\alpha^2}{Q^4}\frac{1+(1-y)^2}{y}\,F_2 = \Gamma_t\,\sigma_{t,QPM} \tag{3.17}$$

$$\sigma_{t,QPM} = \frac{4\pi^2\alpha}{Q^2}\,F_2 \tag{3.18}$$

This uses the definition of the structure function F_2 and the quark charge squares e_f^2 for flavors f:

$$F_2 = x\sum_f e_f^2\,q_f(\xi,\mu_f^2) \tag{3.19}$$

For the QCD-Compton and Boson-Gluon-Fusion cross section, one can write after integrating over the internal degrees of freedom for the hard subprocess [31]:

$$\frac{\mathrm{d}\sigma_{(2+1)-jet}}{\mathrm{d}\xi\,\mathrm{d}Q^2\,\mathrm{d}y} = \frac{\mathrm{d}\sigma_C}{\mathrm{d}\xi\,\mathrm{d}Q^2\,\mathrm{d}y} + \frac{\mathrm{d}\sigma_F}{\mathrm{d}\xi\,\mathrm{d}Q^2\,\mathrm{d}y} \tag{3.20}$$

Summing over particles and antiparticles for the QCD-Compton- and over particles for the Boson-Gluon-Fusion-process, one obtains:

$$\frac{\mathrm{d}\sigma_C}{\mathrm{d}\xi\,\mathrm{d}Q^2\,\mathrm{d}y} = \Gamma_t\,\mathrm{d}\hat{\sigma}_C \sum_{j\in\{f,\overline{f}\}} e_j^2\,q_j(\xi,\mu_f^2) \tag{3.21}$$

$$\frac{\mathrm{d}\sigma_F}{\mathrm{d}\xi\,\mathrm{d}Q^2\,\mathrm{d}y} = \Gamma_t\,\mathrm{d}\hat{\sigma}_F \sum_{j\in\{f\}} e_j^2\,g(\xi,\mu_f^2) \tag{3.22}$$

It is important to note that $\mathrm{d}\hat{\sigma}_F$, $\mathrm{d}\hat{\sigma}_C \sim \alpha_S(Q^2)$. It is well known that the cross sections contain divergences [31]. Massless quarks result in divergences that are absorbed in the process-independent parton densities together with additional divergences in the renormalization procedure. In the final state, soft and collinear partons produce "mass singularities" and

[6]In higher orders of α_S, also the longitudinal polarization of the photon contributes to a flow factor Γ_l. For the sake of simplicity, Γ_l and the corresponding σ_l has been neglected in the notation.

"infrared singularities" that have to be cut out of the phase space and also taken into account by the chosen jet algorithm. The most important algorithms will be described in section 3.4.

As we will be mainly interested in convolutions involving the parton momentum fraction ξ, the generic notation

$$\sigma = \int \mathrm{d}\xi \left[f_{q/p}(\xi,\mu^2)\,\sigma_q(\xi,\mu^2) + f_{g/p}(\xi,\mu^2)\sigma_g(\xi,\mu^2) \right]. \tag{3.23}$$

shall be adopted [32]. Besides the indicated dependence on ξ and μ, σ_q and σ_g also depend on other variables such as the absolute electron four-momentum transfer squared Q^2 and the momenta of the outgoing partons.[7]

In leading order (LO), the prescription for the extraction of $f_{g/p}$ from jet cross sections in deep inelastic scattering reactions is very intuitive. Experimentally the outgoing partons from the hard scattering reactions are identified with jets. The QCD-Compton-scattering and BGF reactions lead to (2+1) jet final states, where the notation accounts for the two outgoing jets from the hard scattering process and the jet in the proton fragmentation region. The calculated contribution

$$\sigma^{\mathrm{LO}}_{C,2+1} = \int \mathrm{d}\xi\, f_{q/p}(\xi,\mu^2)\,\hat{\sigma}_C(\xi) \tag{3.24}$$

from Compton scattering can be subtracted from the measured cross section

$$\sigma^{\mathrm{LO}}_{2+1} = \int \mathrm{d}\xi \left[f_{q/p}(\xi,\mu^2)\,\hat{\sigma}_C(\xi) + f_{g/p}(\xi,\mu)\hat{\sigma}_F(\xi) \right], \tag{3.25}$$

and thus $f_{g/p}(\xi,\mu^2)$ can be determined in LO by a direct unfolding, since in this case ξ can be expressed in terms of measurable quantities as

$$\xi = x\left(1 + \frac{\hat{s}}{Q^2}\right), \tag{3.26}$$

where $\hat{s}$ is the invariant mass squared of the system of the two current jets. An analysis based on this principle can be found in [24].

In NLO this simple picture is destroyed. Aside from the virtual corrections to the Born processes in figures 3.4 and 3.5, real corrections have to be added. An example of a virtual vertex correction diagram is given in figure 3.6. Diagrams of the type shown in fig. 3.7 can also lead to (2+1) jet configurations:

If the gluon attached to the outgoing quark is soft or collinear to the quark, the diagram constitutes a correction to the BGF process. If, on the other hand, this gluon is hard and the outgoing antiquark is soft or collinear to the incoming gluon, then this configuration can be said to be a correction to the QCD-Compton scattering reaction. In the latter case, the collinear or soft antiquark forms a jet with the proton remnant, and the cross section has to be integrated over all momenta of the antiquark according to a specific jet definition scheme. Collinear singularities that do not cancel against corresponding singularities from the virtual corrections have to be absorbed into renormalized parton densities. Depending on the factorization scheme chosen, finite subtracted pieces remain. The factorization theorems of perturbative QCD guarantee that the cross section can be written in the form of equation (3.23). However, beyond the leading order, the arbitrary momentum of collinear partons renders the variable ξ unobservable, because the mass-factorized parton-level cross sections are in general distributions, not regular

[7]Here and in the following we do not explicitly display the dependence on the renormalization scale μ_r and identify μ_f with μ.

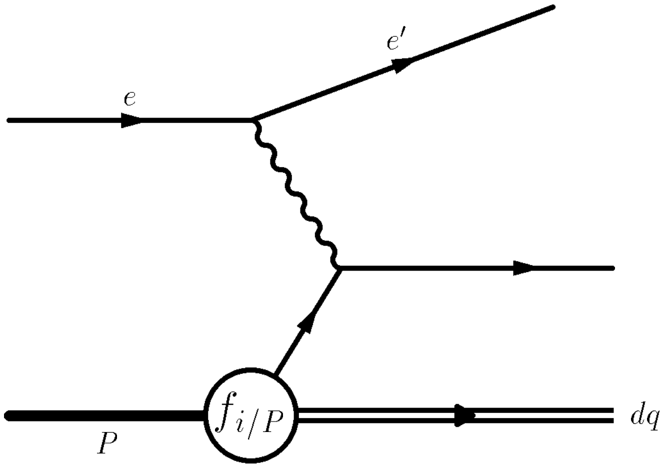

Figure 3.3: **Q**uark **P**arton **M**odel (QPM) Feynman graph.

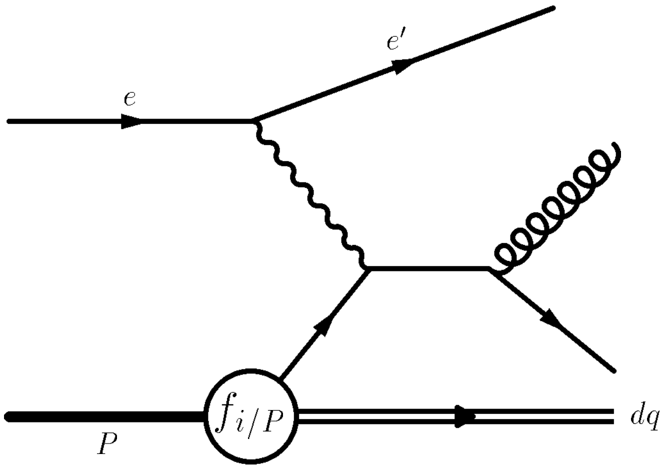

Figure 3.4: Generic diagram for the *QCD-Compton*-process.

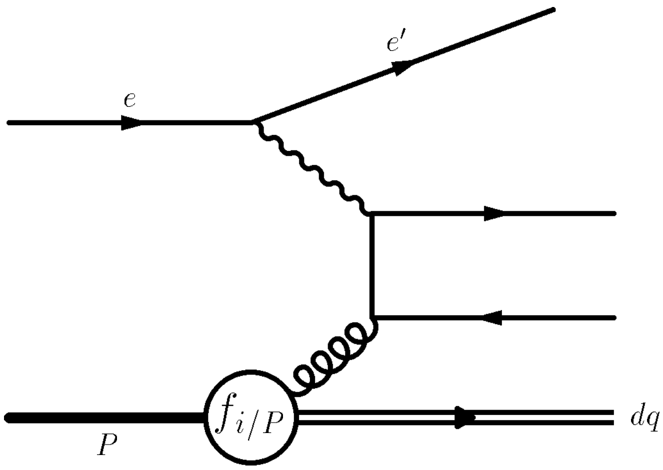

Figure 3.5: Generic diagram for the **B**oson-**G**luon-**F**usion-process (BGF).

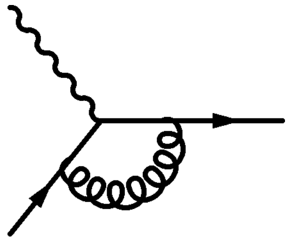

Figure 3.6: Example of a virtual correction diagram.

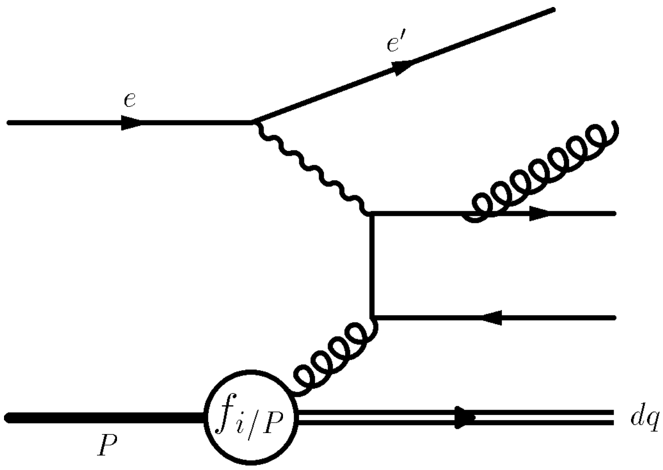

Figure 3.7: Example of a diagram corresponding to a NLO real correction.

functions, and the simple and straightforward method described above can therefore not be applied. A physical consequence is that the distinction between the QCD-Compton- and BGF processes becomes meaningless. Related to this is the fact that quark and gluon densities mix in the Altarelli-Parisi scale evolution (see section 3.8).

A determination of the gluon density in NLO is very desirable. In LO the partonic cross sections σ_q and σ_g (in short denoted by σ_i) do not depend on μ, as already indicated in equation (3.25),[8] and the $f_{i/p}$ (as short-hand for $f_{q/p}$ and $f_{g/p}$) are the solutions of the LO Altarelli-Parisi evolution equation, where the leading logarithmic terms in the scale μ are summed up. In any finite order of perturbation theory, the scattering cross section σ depends explicitly on the factorization scale μ, this scale dependence being due to uncalculated higher-order terms. The scale dependence is particularly strong in the LO case, because there no compensation can take place between $f_{i/p}$ and σ_i. To a great extent this problem is, for many processes, reduced in NLO, where explicit terms $\sim \ln \mu^2$ in σ_i compensate the μ-dependence of $f_{i/p}$ such that the variation is of higher order in the strong coupling constant α_s. For reliable theoretical predictions, a NLO analysis of scale-dependent quantities is therefore mandatory.

The only way to achieve a direct NLO determination of $f_{g/p}$ is to parameterize the function $f_{g/p}$ at a given scale μ_0, to evolve it to a value of μ where the cross section is measured, say $\mu = Q$, and to fit the parameters of $f_{g/p}$ with respect to suitable infrared safe observables, e.g. the (2+1) jet cross section in various bins of x. A severe practical problem is that the

[8]To stress the focus on the parton that induces the interaction, σ_C will be referred to as σ_q and σ_F as σ_g.

Q^2 [GeV^2]	σ_q [pb]	σ_g [pb]
10 ... 14	2.67	6.46
14 ... 18	6.00	15.26
18 ... 25	9.52	23.71
25 ... 40	16.40	39.01
40 ... 100	30.08	63.39
100 ... 300	15.29	17.45
300 ... 700	22.36	17.01
700 ... 4000	17.88	6.57

Table 3.1: Comparison of NLO gluon and quark induced (2+1) jet cross sections, calculated with PROJET. The cuts used are described in chapter 7. The parton density parameterization is MRSH.

cross section σ has to be evaluated repeatedly for every choice of parameters for $f_{g/p}$. Monte Carlo methods allow the application of arbitrary cuts on final-state particle momenta, as is necessary in order to take detector acceptance cuts properly into account, but these methods are prohibitively slow. A fast numerical method for the repeated application of this procedure is indispensable.

It should be noted that the sensitivity of the measurement depends on the influence of the gluon induced part of the (2+1) jet cross section. Therefore a region in phase space is desirable where the gluon induced part is larger than the quark induced contribution. This is typically the case for low Q^2 and low x. Since $\xi > 0.01$ in the analysis discussed here, one would like to choose a low Q^2 region, as is motivated by the cross sections of table 3.1. Unfortunately, the effects of higher orders are large there, so that a compromise is necessary. Furthermore, a region which is compatible with the α_S measurement [25] implies rather large Q^2. Since the analysis conducted here does not subtract the quark induced part directly, but implements this into a fit, the sensitivity is somewhat, but not significantly, reduced.

3.4 Jet Algorithms

After a hard scattering has taken place, higher order effects and the hadronization procedure produce an abundance of particles that proceed through the detector and are further showered there. In order to calculate jets from observed quantities in the detector (or in theoretical models on e.g. hadron level), one has to combine the four vectors under consideration according to a jet algorithm. This algorithm is arbitrary to some degree, since it is given by defining a procedure. For different types of particle collisions, different algorithms were motivated and developed. In e^+e^- physics, the JADE algorithm was favoured, while hadronic collisions like in $p\overline{p}$ favour the cone algorithm.

With the advent of HERA, it was argued that ep collisions lie somewhat "in between" both types of physics. Depending on the point of view, either the leptonic or hadronic part of the interaction was seen as being most important for the choice of algorithm. Therefore, the first calculations to $\mathcal{O}(\alpha_S^2)$ were performed in the modified JADE jet definition scheme [42].

It has been argued that jet algorithms have to be factorizable. This discussion can be followed in [33, 34].

scheme	m_{ij}^2	recombination	remarks
JADE	$2E_iE_j(1-\cos\theta_{ij})$	$p_k = p_i + p_j$	m_{ij}^2 neglects individual masses
E	$(p_i+p_j)^2$	$p_k = p_i + p_j$	Lorentz invariant
E0	$(p_i+p_j)^2$	$E_k = (E_i + E_j)$ $\vec{p}_k = \frac{E_k}{\|\vec{p}_i+\vec{p}_j\|}(\vec{p}_i + \vec{p}_j)$	$\vec{p}$ not conserved
P	$(p_i+p_j)^2$	$\vec{p}_k = \vec{p}_i + \vec{p}_j,\ E_k = \mid \vec{p}_k \mid$	E not conserved
P0	$(p_i+p_j)^2$	$\vec{p}_k = \vec{p}_i + \vec{p}_j,\ E_k = \mid \vec{p}_k \mid$	same as P, but scale updated after each combination

Table 3.2: Recombination schemes of the JADE algorithm; taken from [37].

3.4.1 The JADE Algorithm

Inspired by e^+e^-, the modified JADE algorithm is a cluster algorithm, defined in the following way [35]:

- Define a *precluster* of longitudinal momentum p_r given by the missing longitudinal momentum of the event.

- Apply the JADE cluster algorithm [36] to the set of momenta $\{p_1, \ldots, p_n, p_r\}$, where $p_1, \ldots, p_n$ are the momenta of the hadrons visible in the detector. The resolution criterion is $m_{ij}^2 = 2p_ip_j > y_{cut}M^2$. Here M^2 is a mass scale and y_{cut} is the resolution parameter.

In the case of a theoretical calculation, p_r is directly given by the momentum fraction of the proton not carried by the incident parton, and $p_1, \ldots, p_n$ are the momenta of the partons in the final state. In the following, we choose W^2, the squared total hadronic energy, as the mass scale M^2, since the proton remnant is included in the jet definition.

Because, except for the JADE and E scheme, one operates with massless quantities, a recombination scheme has to be applied to render the clustered objects massless. The different recombination schemes can be found in table 3.2.

Earlier investigations showed that NLO corrections are small, only if the cutoff parameter y_{cut} is of the order of 0.01 [37]. Because $\xi > y_{cut}$, as is obvious from equations 3.26 and 3.11 in combination with the definition of y_{cut}, the choice of this jet algorithm restricts the kinematical region where the parton densities can be probed.

3.4.2 The k_t Algorithm

The k_t algorithm [38] is also a cluster algorithm, performed in the Breit frame. The Breit frame is defined as the frame of reference in which the energy deposit of the electron vanishes. This results in a back-to-back collision of the virtual boson and the scattered parton. The three momentum of the parton is thus reversed in the QPM.

A difference to the JADE algorithm lies in a two step procedure to separate the hard subprocess jets from the remnant jet first, and to resolve the jets in the hard subprocess according to a chosen cutoff parameter in a second step. In addition, the proton direction enters the calculation directly.

The first step is mediated by

$$y_{ip} = 2(1 - \cos\theta_{ip})\frac{E_i^2}{M^2} \tag{3.27}$$

and

$$y_{ij} = 2(1 - \cos\theta_{ij})\frac{\min(E_i^2, E_j^2)}{M^2}. \tag{3.28}$$

Here, θ_{ip} denotes the angle between the object under consideration and the proton direction p. This clustering is continued until $\min(y_{ip}, y_{ij})$ exceeds unity.

In the second step, y_{ij} is computed for all (i, j), and the jets are combined until $\min(y_{ij})$ is larger than a cutoff parameter y_c.

This algorithm was developed for e^+e^- scattering first and later modified for ep collisions. It is also called the *Durham* algorithm.

3.4.3 The Cone Algorithm

The cone algorithm was developed for $p\overline{p}$ data and defines a cone in (η, φ) space. The pseudorapidity η is defined by

$$\eta \equiv -\log(\tan\frac{\theta}{2}), \tag{3.29}$$

while φ is the azimuthal angle.

The cone algorithm is not a cluster algorithm like the JADE and the k_t algorithm. Energy deposits in the detector above a threshold are summed up around a cone of $R = \sqrt{\delta\eta^2 + \delta\varphi^2}$. Common values for R lie between 0.7 and 1. In addition, choices have to be made for the energy threshold, and the minimum energy with which the sum is counted as a jet. An effort to standardize cone jet algorithms led to the *snowmass accord*. Further information can be found in [39].

3.5 Jet Rates

For the determination of the gluon density and α_S, the (2+1) jet cross section is important. However, the measurement of this observable requires the careful analysis of the normalization, i.e. the understanding of detector efficiencies and acceptance, trigger conditions and similar influences. By defining a ratio

$$R_{2+1} \equiv \frac{\sigma_{2+1}}{\sigma_{1+1} + \tilde{\sigma}_{2+1}} \tag{3.30}$$

this problem is almost completely eliminated, since the quantities mentioned above cancel.

This ratio can be defined in several ways; here the ratio of (2+1) jets over the sum of (2+1) and (1+1) jets is chosen.[9] It is important to note that in order to ensure the cancelation effect, the denominator has to consist of an observable that passes selection criteria.

The expression $\tilde{\sigma}_{2+1}$ denotes the (2+1) jet cross section which includes (2+1) events that are later classified as (1+1) events due to jet acceptance cuts. An example is the case for a θ_{jet} cut, where one jet lies in the angular region being cut away. It is sufficient to calculate $\tilde{\sigma}_{2+1}$ to $\mathcal{O}(\alpha_S)$, i.e. in LO, while σ_{2+1} and σ_{1+1} have to be calculated to NLO, i.e. $\mathcal{O}(\alpha_S^2)$ and $\mathcal{O}(\alpha_S)$, respectively, for R_{2+1} to be NLO.

If one wants to determine the jet rate experimentally, one has to correct back from the detector to the parton level. The modeling of the simulation chain from the parton to detector level will be described in chapter 6. The straightforward method is to correct back with the help of a correction factor that describes the ratio of detected jets over jets on the parton level, obtained from a Monte Carlo simulation program. This program has to be able to describe the jet rates consistent with data. A more sophisticated method using a matrix formalism has been investigated in [40], but for the present analysis, the correction factor method is sufficient [25] and will be applied.

3.6 Cross Section Integration Programs

3.6.1 PROJET

The first program that was able to integrate cross sections to $\mathcal{O}(\alpha_S^2)$ was PROJET [41]. It uses the cross sections of [42] and calculates virtual and real corrections. An event record of four vectors is supplied, so that phase space cuts can be freely chosen in addition to the integration variables. The integration is done according to the VEGAS algorithm [43, 44].

PROJET calculates NLO cross sections with massless partons in the $\overline{MS}$ renormalization scheme and the JADE algorithm. The method chosen for the regularization of the cross section is the phase space slicing method. This method results, however, in a recombination scheme of the partons in the jet definition process that cannot be mapped unambiguously to one recombination scheme as discussed in table 3.2. Furthermore, terms proportional to $y_{cut} \cdot W^2/\text{scale}^2$ are neglected.

As will be shown in chapter 4, one can calculate Mellin moments by replacing the parton densities and ensure that also negative contribution to the integration are taken into account correctly.

There exists another program that uses the same cross section calculations, DISJET [45], which yields the same cross sections as PROJET. However, the program is not as flexible in applying user chosen phase space cuts and was therefore not used here.

3.6.2 MEPJET

Recently, the integration program MEPJET [46] has become available. It offers the choice of the JADE, k_t or cone jet algorithm and also does not make the approximations of PROJET and DISJET. In order to gain this flexibility, the jet definition is split into two steps. First, a very small cone[10] is put around the partons under consideration to absorb singularities. In a second

[9] As has been shown before [37], higher jet multiplicities can be neglected in the phase space region considered here.

[10] This cone is not to be confused with the cone jet algorithm!

step, the jet algorithm is applied on these summed quantities. If the cutoff parameter for the cone is chosen small enough, it can be shown that the resulting cross section is independent of it.

Technically, the crossing function technique is needed, which makes it necessary to redefine the parton distributions in the calculation process and map them in beforehand. This makes the definition of Mellin transforms very difficult and cumbersome, as every point in the complex moment plane would have to be mapped to a complete set of crossing functions.

Due to the small cone size needed, the program is very slow and needs about 100 to 1000 times more CPU time than PROJET. Since the calculation of moments is intended to reduce the CPU overhead, this performance is clearly too slow for being used for a gluon density fit at the present stage.

The program does constitute an improvement in accuracy and enables studies with different recombination schemes and jet algorithms. Since it is the only program at the moment, the results have to be taken with caution, as it cannot be cross-checked to other methods. This will hopefully improve in the future with the advent of additional programs, like the announced release of the program DISENT, using the dipole formalism [47].

3.7 Parton Densities

The collinear divergences that arise in the renormalization procedure and that do not cancel against virtual corrections have to be absorbed in parton densities, see the discussion in section 3.3. Since they can only be measured, a parameterization is defined at a starting scale Q_0^2, and the determination for other scales is performed via *Altarelli-Parisi* evolution. For a useful parameterization, at least 3 parameters are necessary [17, 18, 19]. In the further discussion, the factorization scale μ will always be identified with Q^2.

It should be kept in mind that it is very important to compute cross sections using the same factorization procedure for parton densities and the hard subprocess cross section. The parton densities have to be of the appropriate order for the cross sections to be meaningful [48, 49]. Otherwise, the results are inconsistent.

An important consequence of the definition procedure is that the parton densities are universal, i.e. they do not depend on the process under investigation. Therefore, they can also be used e.g. for $p\overline{p}$ scattering. Of course, higher order parton densities are always scheme dependent.

Since the analysis presented here will compute cross sections at different bins in Q^2 and evaluate parton densities at these different scales, it is important to take a closer look at the principles governing this behaviour of the parton densities.

3.8 Altarelli-Parisi-Evolution

The behaviour of parton densities $f_{i/p}(\xi, Q^2)$ is governed by the evolution described by an integro-differential equation, the "Altarelli-Parisi equation." As soon as the parton density for a "starting scale" is given, the evolution to other scales is completely fixed.

3.8.1 Altarelli-Parisi-Equations

If one applies a gluon correction to the struck quark as pictured in figure 3.8, the structure function F_2 is modified to [7]:

$$x^{-1}F_2 = \sum e_q^2 \int \frac{\mathrm{d}w}{w}\, q(w) \left[\delta\left(1 - \frac{x}{w}\right) + \frac{\alpha_S}{2\pi}\, P_{qq}\left(\frac{x}{w}\right) \ln\left(\frac{Q^2}{\mu^2}\right)\right] \tag{3.31}$$

The splitting function P_{qq} is given by

$$P_{qq}(z) = \frac{4}{3}\left(\frac{1+z^2}{1-z}\right)_+ , \tag{3.32}$$

where

$$z = \frac{x}{w}. \tag{3.33}$$

The "+"-prescription has to be applied to this function [7]. It function describes the splitting of a quark into a quark and a gluon. Other splitting functions can be calculated analogously [5, 7]:

$$P_{qg}(z) = \frac{1}{2}\left[z^2 + (1-z)^2\right] \tag{3.34}$$

$$P_{gq}(z) = \frac{4}{3}\frac{1+(1-z)^2}{z} \tag{3.35}$$

$$P_{gg}(z) = 6\left[\frac{z}{(1-z)_+} + \frac{1-z}{z} + z(1-z) + \left(\frac{11}{12} - \frac{f}{18}\right)\delta(1-z)\right] \tag{3.36}$$

Here f denotes the number of active quark flavors. To lowest order, the splitting functions P_{ij} can be interpreted as a probability that a parton i is radiated from parton j. After the absorption of infrared singularities into the bare parton distributions, this behaviour can be rewritten for quark and gluon radiation into the "Altarelli-Parisi equations:"

$$\frac{\mathrm{d}q_i(x,Q^2)}{\mathrm{d}(\ln Q^2)} = \frac{\alpha_S(Q^2)}{2\pi}\int_x^1 \frac{\mathrm{d}w}{w}\left[q_i(w,Q^2)\, P_{qq}\left(\frac{x}{w}\right) + g(w,Q^2)\, P_{qg}\left(\frac{x}{w}\right)\right] \tag{3.37}$$

$$\frac{\mathrm{d}g(x,Q^2)}{\mathrm{d}(\ln Q^2)} = \frac{\alpha_S(Q^2)}{2\pi}\int_x^1 \frac{\mathrm{d}w}{w}\left[\sum_i q_i(w,Q^2)\, P_{gq}\left(\frac{x}{w}\right) + g(w,Q^2)\, P_{gg}\left(\frac{x}{w}\right)\right] \tag{3.38}$$

In leading order, the "one loop approximation," diagrams contribute. It is interesting to note some useful properties of the splitting functions:

$$P_{\overline{q}g}(z) = P_{qg}(z) \tag{3.39}$$

$$P_{g\overline{q}}(z) = P_{gq}(z) \tag{3.40}$$

Momentum conservation at the splitting vertex gives (for $z < 1$):

$$P_{qg}(z) = P_{qg}(1-z) \tag{3.41}$$

$$P_{gg}(z) = P_{gg}(1-z) \tag{3.42}$$

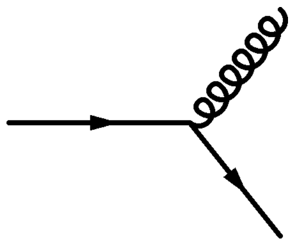

Figure 3.8: Generic diagram for gluon radiation.

$$P_{qq}(z) = P_{gq}(1-z) \tag{3.43}$$

The integral of $P_{qq}(z)$ over all z vanishes:

$$\int_0^1 \mathrm{d}z\, P_{qq}(z) = 0 \tag{3.44}$$

This is equivalent to the relations:

$$\int_0^1 (u - \overline{u})\,\mathrm{d}z = 2, \quad \int_0^1 \left(d - \overline{d}\right)\mathrm{d}z = 1 \tag{3.45}$$

$$S = \int_0^1 \mathrm{d}z\,[s(z) - \overline{s}(z)] = 0 \tag{3.46}$$

$$C = \int_0^1 \mathrm{d}z\,[c(z) - \overline{c}(z)] = 0 \tag{3.47}$$

Momentum conservation implies the sum rule

$$\int_0^1 \mathrm{d}z\, z\left[\sum q(z,Q^2) + g(z,Q^2)\right] = 1 \tag{3.48}$$

as well as

$$\int_0^1 \mathrm{d}z\,[P_{qq}(z) + P_{gq}(z)] = 0, \quad \int_0^1 \mathrm{d}z\,[2f\, P_{qg}(z) + P_{gg}(z)] = 0. \tag{3.49}$$

Another important relation is the Baryon number sum rule:

$$B = \int_0^1 \mathrm{d}z\,\frac{1}{3}\,[u(z) - \overline{u}(z) + d(z) - \overline{d}(z) + s(z) - \overline{s}(z) + c(z) - \overline{c}(z)] = 1 \tag{3.50}$$

The NLO splitting functions are bulky, and will not be presented here; the references can be found in [50]. They involve "two loop" diagrams.

3.8.2 Solving the Altarelli-Parisi Equations

With the Altarelli-Parisi equations, one can derive the behaviour of a given parton distribution $q_i(\xi, Q^2)$ and $g(\xi, Q^2)$ with the change of Q^2, provided they are known at some start value $Q^2 = Q_0^2$, and $Q^2 \gg \Lambda_{QCD}^2$. This is an explicit violation of the Bjorken scaling of structure functions predicted by the simple parton model [7]. Λ_{QCD} is the QCD scale that is introduced in the renormalization procedure and has to be determined by an experiment.

To simplify the discussion of the evolution equations, it is convenient to redefine the dependence of $\alpha_S(Q^2)$ on Λ_{QCD}:

$$t \equiv \ln(Q^2/\Lambda^2_{QCD}) \tag{3.51}$$

Introducing the symbolic notation

$$P_{qq} \otimes q_i = \int_x^1 \frac{\mathrm{d}w}{w} P_{qq}\left(\frac{x}{w}\right) q_i(w,t)\,, \tag{3.52}$$

and similarly for other convolutions, one can rewrite equations 3.37 and 3.38 as:

$$\frac{\mathrm{d}q_i}{\mathrm{d}t}(x,t) = \frac{\alpha_S(t)}{2\pi}[P_{qq} \otimes q_i + P_{qg} \otimes g] \tag{3.53}$$

$$\frac{\mathrm{d}g}{\mathrm{d}t}(x,t) = \frac{\alpha_S(t)}{2\pi}[P_{gq} \otimes \sum_i q_i + P_{gg} \otimes g] \tag{3.54}$$

The solution of these integro-differential equations makes the specification of starting conditions necessary at $t = t_0$. The usual approach is to parameterize a distribution at this starting scale around 2–5 GeV^2 and then fit the parameterization to data by numerically evolving the parameterization, i.e. solving the Altarelli-Parisi equations.

These equations assume the quarks to be massless. The simplest approach for taking heavy quarks into account is to decouple them from the equations below a threshold and include the contribution, once the mass threshold is passed. This includes the adaption of the quark number parameter f.

The GRV parameterization takes a different approach [17]. The valence quarks are parameterized according to basic sum rules at $Q_0^2 = 4$ GeV^2 and then evolved backwards to 0.34 GeV^2, where the sea quark and gluon evolution is assumed to start by dynamical evolution. Then the evolution to the scale Q^2 under consideration is performed.

To solve the evolution equations, it is useful to separate the quark densities into linear combinations of the following distributions. Define *singlet distributions*

$$q^S(x,t) = \sum_i (q_i + \overline{q}_i), \tag{3.55}$$

summed over all active flavors $i = 1, 2, \ldots, f$. There are many *nonsinglet distributions*, including

$$u_v = u - \overline{u},\;\; d_v = d - \overline{d},\;\; q_i^{NS} = q_i - (2f)^{-1} q^S, \tag{3.56}$$

and linear combinations thereof. They all fulfill the relations [7]:

$$\frac{\mathrm{d}q^{NS}}{\mathrm{d}t}(x,t) = \frac{\alpha_S(t)}{2\pi} P_{qq} \otimes q^{NS} \tag{3.57}$$

$$\frac{\mathrm{d}q^S}{\mathrm{d}t}(x,t) = \frac{\alpha_S(t)}{2\pi}[P_{qq} \otimes q^S + 2f P_{qg} \otimes g] \tag{3.58}$$

$$\frac{\mathrm{d}g}{\mathrm{d}t}(x,t) = \frac{\alpha_S(t)}{2\pi}[P_{gq} \otimes q^S + 2f P_{gg} \otimes g] \tag{3.59}$$

The numerical integration of equations 3.57 to 3.59 can be either performed directly by stepwise numerical evaluation, or a transformation to a moment space, e.g. the Mellin moment space.

It can be shown [7], that the Mellin moments can be mapped to *Fourier transforms*, where fast numerical programs for inverting the moments exist. The calculation performed by GRV uses a direct inversion method of Mellin moments which will be used in the following [51, 52, 53].

Another difference between the evolution in x space (i.e. the direct numerical evolution) and the computation of a Mellin moment evolution is that the parameterizations are not formally to the same order, since the evolution in moment space has to use a slightly different definition of the terms that are taken into account, resulting in differences to **N**ext-to-**N**ext-to-**L**eading **O**rder (NNLO). Recent progress has allowed for a clarification and standardization [54, 55].

It should be noted that one property of the splitting functions and thus the evolution is the fact that sea quark densities rise with decreasing ξ. This is, of course, expected intuitively, since the probability for the production of quark-antiquark pairs and gluons rises accordingly. It is an open question whether a saturation effect occurs at some point and how this saturation will manifest itself.

Chapter 4

The Mellin Transform Technique

As was motivated in the chapters before, a NLO determination of the gluon density for arbitrary factorization schemes can only be achieved via a fit. The problem that arises when a fit to some jet observable is performed consists of the CPU time requirements in repeatedly evaluating the adapted cross sections. One wishes to parameterize a gluon density, evolve it to the scale at which it enters the cross section calculation and then integrate the cross section by applying additional phase space cuts. This process has to be iterated until the fit procedure converges. Unfortunately, the NLO calculation by a Monte Carlo integration is quite slow,[1] not allowing for a manageable amount of computing time to complete the fitting task, especially since an optimization of the analysis requires repeated running of different fits, and the determination of errors needs additional calculations.

Therefore, the Mellin transform technique was developed to decouple the integration of the hard cross section part and the parton density evolution. By doing this, the time consuming integration step has to be performed only once, while the modification of parton densities and the subsequent computation of the cross section can be done fast in a separate fitting procedure. Any other transformation could have achieved the same goal, as long as the underlying mathematical requirements are fulfilled.

It should be kept in mind that the method works universally also for quark densities. However, since they are well known in the kinematical region under consideration and since each parton density requires an additional set of Mellin transforms, the quark densities are assumed as known and the error induced by their uncertainty is absorbed into the systematic error. This means that the quark induced (2+1) jet cross section is integrated directly.

This method can, in principle, also be applied to other jet observables and a modification to e.g. $\overline{p}p$ collisions seems easily possible.

The formal derivation of the method is presented in [32]. Here, an overview over the method and its implementation is presented. Additional details can be found in appendix A.

[1] The numerical calculation of one cross section needs about 1 minute of CPU time on an SGI Challenge processor in LO, and about 10 minutes in NLO with PROJET.

4.1 The Mellin Transform Technique for Non-Factorizing Cross Sections

The Mellin transform technique allows for a quick numerical evaluation of integrals of the form

$$\Sigma(x) \; = \; \int_x^1 \frac{\mathrm{d}\xi}{\xi} \, f_{i/p}(\xi) \, \sigma_i\left(\frac{x}{\xi}, x\right) \tag{4.1}$$

in the case where σ_i is independent of its second argument x, on the basis of the moments defined by

$$F_n \; \equiv \; \int_0^1 \frac{\mathrm{d}x}{x} \, x^n \; F(x) \tag{4.2}$$

for an arbitrary function F and (complex) n. The moments of the function Σ are then given by

$$\Sigma_n \; = \; f_{i/p,n} \, \sigma_{i,n}. \tag{4.3}$$

The functional dependence of Σ can be recovered from the moments Σ_n by an inverse Mellin transform. An expression of the form of equation 4.1 will be called to be of the *factorizable type* if the only dependence on x in the arguments of σ_i is via x/ξ. In the application which we have in mind, $f_{i/p}$ is a parton density, whereas σ_i is an expression for a mass-factorized parton-level scattering cross section. In general, acceptance cuts and non-factorizable jet algorithms introduce an explicit dependence of σ_i on x. Moreover, the expression for $\Sigma(x)$ is integrated over a certain range of x. This might suggest that the Mellin transform technique cannot be applied. However, this is not the case. As is shown in [32], one can still use this technique, provided one finds a suitable moment definition.

Assume a fixed Q^2-bin (i.e. a fixed factorization scale), then let $a_1, \ldots, a_k$ be the experimental boundaries of the intervals in the Bjorken variable x for which the cross sections are measured. To proceed, we define

$$\Sigma_a \; \equiv \; \int_a^1 \mathrm{d}x \, \Sigma(x). \tag{4.4}$$

The integral over a specified interval $[a_i, a_{i+1}]$ in x is then simply given by

$$\int_{a_i}^{a_{i+1}} \mathrm{d}x \, \Sigma(x) = \Sigma_{a_i} - \Sigma_{a_{i+1}}. \tag{4.5}$$

It should be noted that this can be a numerical disadvantage, since depending on the phase space region, large numbers might be subtracted numerically to yield a small number. Even though the integration error on the individual integrals is small, the difference could bear a much larger uncertainty. Therefore, one has to make sure that subsequent bins of similar size are avoided, if one wants to calculate bins that do not reach to 1 in x.

Define a function

$$h_a(u) \; \equiv \; \begin{cases} \displaystyle\int_a^{a/u} \mathrm{d}x \, \sigma_i\left(\frac{x}{a/u}, x\right), & \text{if} \quad u \geq a \\ \qquad\qquad 0, & \text{if} \quad u < a \end{cases} \tag{4.6}$$

and its moments in the variable u

$$h_{an} \; \equiv \; \int_0^1 \frac{\mathrm{d}u}{u} \, u^n \, h_a(u). \tag{4.7}$$

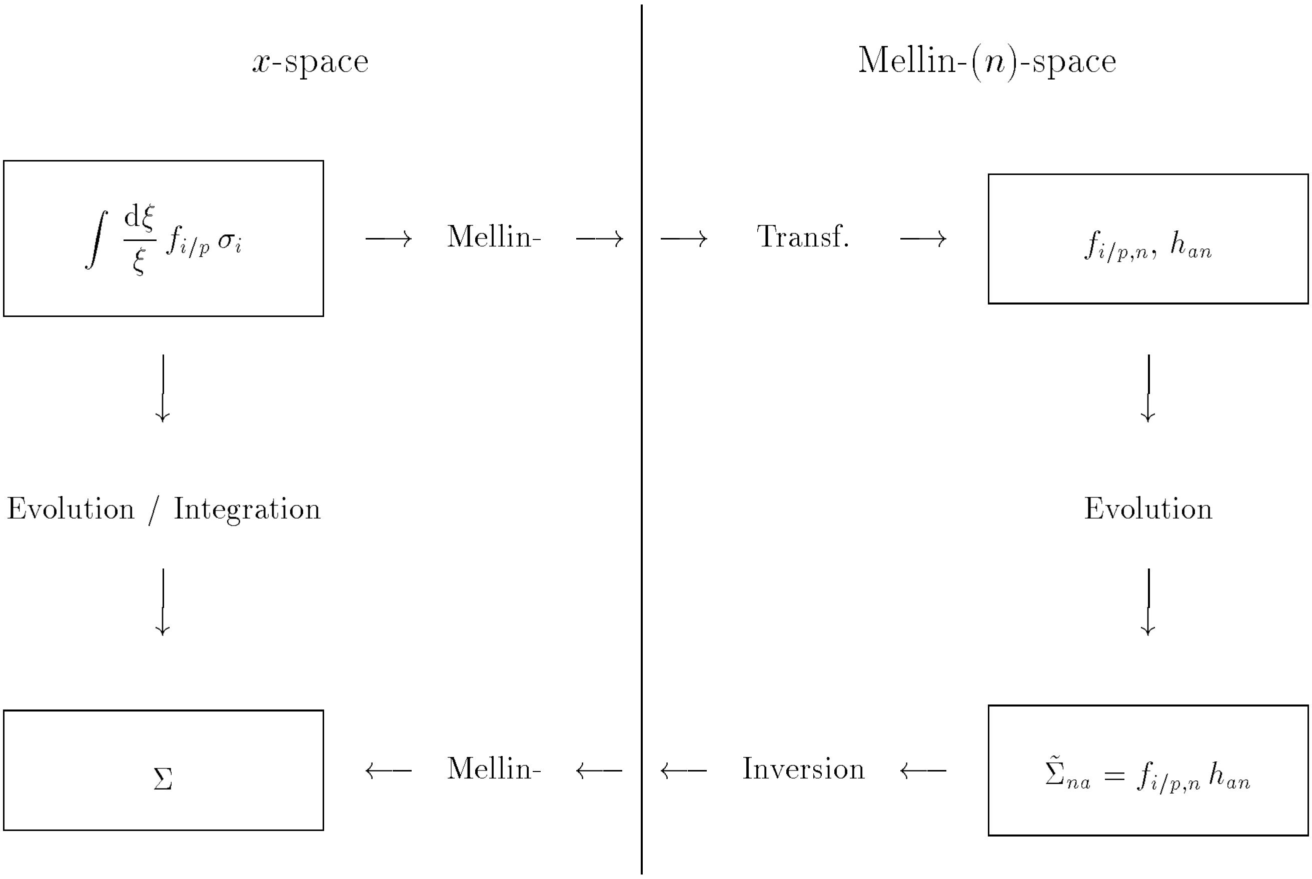

Figure 4.1: Simplified picture of the procedure to calculate the cross section $\Sigma(x)$ using Mellin transforms.

It is shown in appendix A that an explicit expression for h_{an} is

$$h_{an} \;=\; \int_a^1 \mathrm{d}x \int_x^1 \frac{\mathrm{d}\xi}{\xi} \left(\frac{a}{\xi}\right)^n \sigma_i\left(\frac{x}{\xi}, x\right). \tag{4.8}$$

The h_{an} are thus the Σ_a with the parton density $f_{i/p}(\xi)$ replaced by $(a/\xi)^n$. They can be determined numerically by means of a Monte Carlo integration. In general, for complex n, the quantity $(a/\xi)^n$ has to be split into its real and imaginary part.

Define

$$\Sigma_{ab} \;\equiv\; \int_a^1 \frac{\mathrm{d}\xi}{\xi} f_{i/p}(\xi)\, h_b\left(\frac{a}{\xi}\right) \tag{4.9}$$

and determine the moments of Σ_{ab} with respect to the variable a:

$$\tilde{\Sigma}_{nb} \;\equiv\; \int_0^1 \frac{\mathrm{d}a}{a}\, a^n\, \Sigma_{ab}. \tag{4.10}$$

Obviously, $\Sigma_a = \Sigma_{aa}$. Then the key relation of the method can be easily derived [32]:

$$\tilde{\Sigma}_{nb} = f_{i/p,n}\, h_{bn} \tag{4.11}$$

This means that for a given parameterization of $f_{i/p}$ in terms of its moments $f_{i/p,n}$ the cross section Σ_a can be determined by forming the moments $\tilde{\Sigma}_{na} = f_{i/p,n}\, h_{an}$ and a subsequent inverse Mellin transform in the variable n, evaluated at a. A schematic overview of the cross section calculation procedure by Mellin transforms is shown in figure 4.1.

This method of determining the cross section introduces the inconvenience that the moments h_{an} have to be determined for every boundary separately. However, due to the large number of cross section evaluations in the fitting procedure, this method is far more efficient than a direct integration of the cross section for every parton density parameterization separately.

The calculation of moments is possible by a numerical cross section integration program like PROJET. One has to take into account, however, that negative contributions to the integral have to be allowed, since the moments are complex numbers and therefore have to be assembled by its real and imaginary part.

For the calculation by PROJET, the Mellin moments are split into their real and imaginary parts by splitting the expression $(a/\xi)^n$ (see equation 4.8):

$$\begin{aligned} \left(\frac{a}{\xi}\right)^n &= \zeta^n \\ &= \zeta^{re^{i\varphi}} \\ &= \zeta^{r\cos\varphi}\left[(\cos(\ln(\zeta)\, r\sin\varphi)) + i\ (\sin(\ln(\zeta)\, r\sin\varphi))\right] \end{aligned} \tag{4.12}$$

4.2 From Parton Moments to Observables

Once the moments h_{an} have been calculated, one needs to determine the evolved moments of the parton density $f_{i/p,n}$ by an Altarelli-Parisi evolution and to invert the product $\tilde{\Sigma}_{na}$.

Let us now consider the inverse transformation of the moments given by equation 4.2, which is a special case of the general Mellin transformation for functions $F(x)$ vanishing identically at $x > 1$. If $F(x)$ is piecewise smooth for $x > 0$, the corresponding Mellin inversion reads

$$F(x) = \frac{1}{2\pi i}\int_{c-i\infty}^{c+i\infty} \mathrm{d}n\, x^{-n} F_n, \tag{4.13}$$

where the real number c has to be chosen such that $\int_0^1 dx\, x^{c-1} F(x)$ is absolutely convergent [56]. Hence c has to lie to the right of the rightmost singularity n_{max} of F_n. The contour of the integration in equation 4.13 is displayed in fig. 4.2 and denoted by $\mathcal{C}_0$. Also shown is a deformed route $\mathcal{C}_1$, yielding the same result as long as no singularities n_i of F_n are enclosed by $\mathcal{C}_0 - \mathcal{C}_1$. For example, for the LO and NLO evolution of structure functions, the n_i are real with $n_i < n_{max} < c$, and this requirement is fulfilled automatically.

It is useful to rewrite equation 4.13 as an integration over a real variable. We are concerned with functions obeying $F_n^* = F_{n^*}$, where '$*$' denotes the complex conjugation. Then it is easy to show that equation 4.13 yields, for the contour characterized by the abscissa c and the angle ϕ in fig. 4.2:

$$F(x) = \frac{1}{\pi}\int_0^\infty \mathrm{d}z\, \mathrm{Im}\left[\exp(i\phi)\, x^{-c-z\exp(i\phi)} F_{n=c+z\exp(i\phi)}\right]. \tag{4.14}$$

It is obvious from the discussion given above that the integral does not depend on c and ϕ. However, for an efficient numerical evaluation a suitable choice of these parameters is very useful. For example, it is advantageous to choose $\phi > \pi/2$ in case F_n is a known analytical

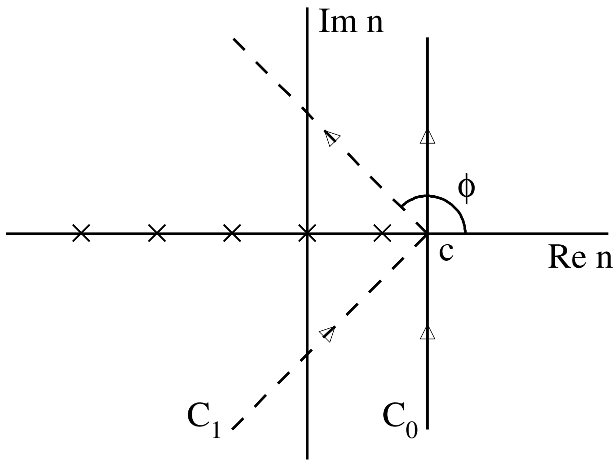

Figure 4.2: Integration contours of the Mellin inversion in equation 4.13, leading to the inversion formulae of equations 4.14 and 4.15 for the routes $\mathcal{C}_0$ and $\mathcal{C}_1$, respectively. The crosses schematically denote the singularities of F_n.

function, especially if this function does not fall off very rapidly for $|n| \to \infty$. The factor $\exp\left(z \log \frac{1}{x} \cos\phi\right)$ then introduces an exponential dampening of the integrand (which rapidly oscillates at small x) with increasing z, thereby allowing for a smaller upper limit z_{max} in the numerical implementation of equation 4.14. This procedure has been employed for the inversion of moments of parton densities and structure functions for the proton and the photon, e.g. in [51, 52] and [53], respectively.

In general, however, the moments of the partonic cross section can only be calculated numerically using equation 4.2, because no analytic continuation to small $\mathrm{Re}\, n$, where the integral does not exist, is at our disposal. Likewise, in our case these moments are given by equation 4.8 and do not behave uniformly for $|n| \to \infty$. Especially, they grow exponentially along $\mathcal{C}_1$. Therefore, we will use the 'textbook contour' $\mathcal{C}_0$ in the following and, with $\phi = \pi/2$, equation 4.14 simplifies to

$$F(x) = \frac{1}{\pi} \int_0^\infty \mathrm{d}z \; \mathrm{Re}\left[x^{-c-iz} F_{n=c+iz}\right] . \tag{4.15}$$

We have applications in mind where $F_n = f_{i/p,n} h_{an}$, see equation 4.11, and the numerical evaluation of the moments h_{an} in equation 4.8 is *very* time-consuming. Taking a different upper limit z_{max} of the numerical z-integration or number of points for the integral at each step in the integration process is practically unfeasible in such a case. Instead, we want to fix z_{max} at a value as small as possible in order to allow for an evaluation of equation 4.15 with a rather small number of fixed moments.

As is estimated in [32], z_{max} lies somewhere between 6.0 and 8.0 depending on x. In this analysis, $z_{max} = 9$ yielded a sufficiently accurate convergence behaviour, i.e. the cross sections were calculated up to an accuracy of 1%.

The integral equation 4.15, truncated at z_{max}, can now be performed by using a sufficiently large number of fixed support points, e.g. by a sum of 8-point Gaussian quadratures, see [57] for the weights and support points. A table of the support points used for this analysis can be found in appendix B.

4.3 Application to Jet Physics at HERA

To illustrate how the Mellin transform method can be used to fit the gluon density $f_{g/p}$, the gluon-induced (2+1) jet cross sections were calculated in several bins for 820 GeV protons and 27.6 GeV electrons. Quark contributions were set to zero explicitly in the parton distribution function to reduce the number of moments needed for this case study.

The program PROJET [41] based on the NLO matrix elements from [42] was used, this allows to calculate jet cross sections in LO and NLO in the modified JADE scheme, as discussed in chapter 3. In the case of a theoretical calculation, p_r is directly given by the momentum fraction of the proton not carried by the incident parton, and $p_1, \ldots, p_n$ are the momenta of the partons in the final state. In the following, we choose W^2, the squared total hadronic energy, as the mass scale M^2, since the proton remnant is included in the jet definition.

The integration routine used in PROJET is VEGAS [43, 44]. As is desirable for an experimental measurement, the phase space was binned in Q^2 and x according to equation 4.4; the bins are given in tables 4.1 and 4.2. In addition, the following typical H1 detector cuts were applied, for which the motivation is explained in chapter 7:

- The invariant mass squared of the hadronic system W^2 was required to be larger than $5000\,\mathrm{GeV}^2$.
- The jet resolution cut y_{cut} was set to 0.02. Lowering this value significantly below 0.01 causes NLO corrections to dominate and leads to unphysical cross sections. It is important to note that $\xi \geq y_{cut}$ as a consequence of the applied modified JADE algorithm. The region $\xi > 0.01$ is however very interesting [22] for a precise determination of $f_{g/p}$, see also [21].
- The jets were required to lie in the polar angle range of $10° \leq \theta_{jet} \leq 145°$.
- For bins with $Q^2 \leq 100\,\mathrm{GeV}^2$, the scattered electron had to have an energy of $E_{e'} \geq 14\,\mathrm{GeV}$ and the polar angle had to lie within the range of $160° \leq \theta_{e'} \leq 172.5°$.
- In the bins with $Q^2 \geq 100\,\mathrm{GeV}^2$, the scaled photon energy y in the proton rest system had to be $y \leq 0.7$ and the scattered electron was required to have $10° \leq \theta_{e'} \leq 148°$.

In this list, angles and energies are defined in the laboratory frame, and angles are given with respect to the direction of the incoming proton. For each bin, 32 complex Mellin moments were calculated according to the prescription described in section 4.1, see equation 4.8. In all calculations, α_s was computed to second order, and the NLO gluon distribution function of [52] was employed.

A good convergence of the numerical calculations was found for $c = 1.8$, $\phi = \pi/2$ and $z_{max} = 9$, with a higher density of support points at lower z, as the influence is greatest there. For comparison, the cross section was also calculated directly, see equation 4.4. After inverting the product of the hard subprocess and evolved gluon density moments at the average Q^2, the results were found to coincide at the per cent level. The detailed results can be found in tables 4.1 and 4.2. In most bins, convergence was reached at $z_{max} = 3$ (corresponding to 16 moments), the additional moments were used for safety. The convergence of the LO cross section was much faster than in the NLO case, as for a given number of support points in VEGAS, the LO

	x							
Q^2 [GeV^2]	$10^{-4}\ldots 1$		$10^{-3}\ldots 1$		$10^{-2}\ldots 1$		$10^{-1}\ldots 1$	
10 … 14	62.80	61.64	28.09	28.74	—	—	—	—
14 … 18	70.64	69.72	50.95	49.97	—	—	—	—
18 … 25	85.82	84.89	71.03	69.80	—	—	—	—
25 … 40	109.9	108.8	101.9	101.1	—	—	—	—
40 … 100	—	—	123.8	124.4	14.51	14.43	—	—
100 … 300	—	—	31.96	32.18	14.69	14.76	—	—
300 … 700	—	—	28.97	29.23	25.18	25.42	—	—
700 … 4000	—	—	—	—	10.22	10.12	0.96	0.93

Table 4.1: Comparison of cross sections with LO matrix elements[2] (in [pb]) obtained by integrating directly (left columns) or using the Mellin transform method (right columns).

	x							
Q^2 [GeV^2]	$10^{-4}\ldots 1$		$10^{-3}\ldots 1$		$10^{-2}\ldots 1$		$10^{-1}\ldots 1$	
10 … 14	58.48	57.25	26.60	26.00	—	—	—	—
14 … 18	66.57	65.90	47.22	46.69	—	—	—	—
18 … 25	82.48	81.65	67.99	66.87	—	—	—	—
25 … 40	108.1	107.4	100.4	99.71	—	—	—	—
40 … 100	—	—	126.1	125.6	14.07	13.96	—	—
100 … 300	—	—	34.86	34.52	15.51	15.31	—	—
300 … 700	—	—	31.34	31.51	27.01	27.19	—	—
700 … 4000	—	—	—	—	11.18	11.19	0.99	0.97

Table 4.2: Comparison of NLO cross sections (in [pb]) obtained by integrating directly (left columns) or using the Mellin transform method (right columns).

integration is more accurate due to the simpler integration kernel. The method works well for both LO and NLO.

The number of points in the Monte Carlo integration was chosen such that the error returned by VEGAS was less than 1%. This number is, however, only a rough estimate [43, 44], and the achieved accuracy was studied by repeating the calculation for different random number generator seeds. The direct integrations performed here had a statistical variation of 2–3%. The partonic cross section from the Mellin transform method is implicitly integrated repeatedly by the calculation of the moments, which smoothes out statistical variations. The results were found to be more stable than the direct integration, which varied around the result obtained by the moment inversion. Even drastic errors of single moments or setting single moments to zero could be tolerated and led to a reproducible result. We conclude that this method is numerically very stable and that the accuracy is of the order of 1%. Increasing the accuracy requires increasing the number of support points for the integration, which would result in a

[2]Here, 'LO' means that the matrix elements were calculated in LO, but α_s and the parton distribution functions in NLO to facilitate a comparison with the results of table 4.2. For a physically meaningful comparison of the LO with the NLO, α_s and the parton distribution functions should be calculated in LO, if they are used in conjunction with the LO matrix elements.

dramatic increase in CPU time.[3] One has to keep in mind that an additional error source arises from the Mellin transform method, as for each experimental bin in x one has to calculate the difference of the cross sections depending on the bin boundaries in equation 4.5, leading to error propagation.

4.4 Fitting the Gluon Density

The extraction of the gluon density can be performed via a χ^2 fit. Defining an observable ω, χ^2 is given by:[4]

$$\chi^2 = \sum_i \frac{(\omega(i) - \varpi(i))^2}{\omega_\sigma(i)^2} \tag{4.16}$$

Here, i denotes the number of independent measurements, which in the case of fitting cross sections or jet rates can be identified with the number of bins in which the measurement takes place. ω_σ is the uncertainty of the measurement; in the following, one standard deviation will be assumed for the error, if applicable. $\varpi(i)$ stands for the mean of the function ω, or in the case of a measurement, this translates to the fit of a theoretically motivated function ω to the measurement ϖ. Therefore, a different notation is frequently chosen to describe the different variables and functions under consideration.

To determine the "best" value of ω, the function χ^2 has to be minimized [58]. Since normally this minimization procedure cannot be done analytically, numerical procedures have to be employed. The most common program package used is MINUIT [59], which is widely tested and will also be applied in this work. In [58, 59], further mathematical details about χ^2 fitting can be found.

The procedure for fitting the gluon density involves the parameterization of $g(\xi, Q^2)$ at the input scale $Q_0^2 = 4$ GeV^2, as is done with the MRS parameterizations. For the fitting purpose pursued here, the GRV procedure of parameterizing the valence quarks at 4 GeV^2 and subsequently evolving "backwards" to 0.34 GeV^2, where the onset of sea quark and gluon density is dynamically generated, is less desirable, since the backward evolution and the longer evolution distance for gluons reduces the sensitivity of the fit. Nevertheless, the evolution of MRSD-' type parameterizations will be done in moment space, in contrast to the x space evolution normally performed by MRS, as discussed in chapter 3.

Thus, the ansatz

$$g(\xi, Q_0^2) = A_N \xi^\alpha (1-\xi)^\beta (1+\gamma\xi) \tag{4.17}$$

was made at $Q_0^2 = 4$ GeV^2, and the calculation of the gluon induced cross section was performed as described in section 4.3, by evolving equation 4.17 to the scale Q^2 under consideration in moment space and inverting the moment product.

To show that a known gluon density parameterization could be fitted back, gluon induced (2+1) jet cross sections defined by MRSD-' [60, 61] were calculated with the cuts described above. It should be noted, that for the purpose of demonstrating the applicability of the fit, the exact definition of the phase space is not of importance, as long as the function to be fitted (i.e. the cross section) is treated in the same way as the underlying calculation (i.e. the direct integration by PROJET). The same applies for the error determination. Since we deal with

[3] The numerical calculation of one moment needed about 2 minutes of CPU time on an SGI Challenge processor in LO, and about 20 minutes in NLO.

[4] To avoid confusion with cross section variables, the common notation of σ for errors was replaced by ω_σ.

parameter	min	max	MRSD-'
α	-0.7	-0.1	-0.5
β	4.0	7.0	5.3
γ	0.0	20.0	10.6

Table 4.3: Parameter range used for the fitting procedure in comparison to MRSD-' values.

functions that can in principle be calculated to arbitrary precision, an error determination does not make sense at this point. ω_σ was therefore set to 1, as it only rescales χ^2 and does not affect the fit itself. It is, however, important to check whether the accuracy with which the gluon density is reproduced is similar to the integration accuracy of the cross section. This can be achieved by comparing the resulting gluon density with the parameterization that shall be reproduced and make sure that the ratio is close to 1.

The normalization constant A_N is given by sum rules provided the quark densities are given at Q_0^2. Since they are well known in the region under consideration and the difference between all common parameterizations are small, the quarks of MRSD-' were always used [60, 61]. The error induced by this assumption can be neglected.

To exclude physically meaningless parameter values, the allowed parameter-space was restricted as described in table 4.3. This removes unwanted χ^2 minima and ensures that unphysical solutions for the gluon density are avoided. In addition, it is important to choose a proper initial step width for the fit, since otherwise the calculation of the error matrix by using derivatives of the χ^2 function can become numerically unstable and can cause convergence problems.

For the purpose of fitting, the NLO (2+1) jet cross section is decomposed into the quark induced and the gluon induced part. The quark induced contribution can be integrated directly by PROJET, while the gluon induced cross section is calculated by the Mellin transform method and is modified by the fit. This sum is compared to the direct integral of the complete (2+1) jet cross section by PROJET in the fitting procedure. One bin in Q^2 was chosen.

As can be seen in figure 4.3, the gluon density is well reproduced and also the ratio between the original and the fitted gluon density is of the order of 1%, and thus more accurate than the integration accuracy of PROJET. This can be explained, as mentioned previously in section 4.3, by the additional accuracy gained through the repeated calculation of moment integrals, which averages out statistical fluctuations.

Furthermore, it should be noted, that the region actually fitted is only for $\xi > y_{cut}$, i.e. the plot of the gluon density for smaller ξ is an extrapolation. Nevertheless, the agreement is still excellent, although the ratio is getting worse, as one would expect from such an extrapolation.

To show that also jet rates can be reproduced, the procedure was repeated with the jet rate definition of equation 3.30. The calculation of the jet rate requires the computation of two sets of moments per bin for the gluon induced parts of σ_{2+1} and $\tilde{\sigma}_{2+1}$. Both are modified in the fitting procedure. The quark induced parts are integrated directly.

As can be seen from figure 4.4, the gluon density is again reproduced, although the deviation increases slightly. This is due to the larger number of cross sections that have to be computed. In addition, two sets of moments have to be evaluated, and a ratio of cross sections is calculated.

Another demonstration of the sensitivity of the fit can be obtained by introducing an additional point at $\xi = 0.005$ and $Q^2 = 20$ GeV^2 with an extremely high or low gluon density, respectively. In figure 4.5 (top), a gluon density of 20 was assumed at the additional point in one fit, and in the bottom plot, a value of 1 was assumed. As can be clearly seen, the fit is distorted in the direction of the additional point. Since these fits are rather extreme, they also illustrate the parameter range that can be covered with the boundaries of table 4.3, although the error treatment described below also allows additional deviations.

These scenario calculations and fits show that it is possible to use the Mellin transform technique to fit the gluon density from jets.

To summarize the fitting procedure for further reference, the most important steps are repeated here:

- For each bin in Q^2, calculate the quark induced cross sections directly with PROJET.
- For each bin in Q^2, calculate the Mellin transforms for the gluon induced part of the cross section for σ_{2+1} and $\tilde{\sigma}_{2+1}$.
- In the fit, the ansatz 4.17 is modified by varying the parameter set α, β, γ. The normalization A_N is fixed by the chosen quark density parameterization.
- Transform the gluon density ansatz 4.17 into Mellin moment space and perform the evolution to the desired scale. The sum rules are automatically fulfilled.
- Compute the product of equation 4.3 and invert it.
- Compose the jet rate from the individual cross section contributions.
- Compare the jet rate to corrected data and vary the parameters, if necessary.

4.5 Error Treatment

In order to determine an error of the fit, the straightforward method of using the MINOS option of [59] is not feasible, since the three parameter fit of jet rates is a rather complex mathematical problem, and it turns out that the MINOS procedure does not converge, nor does it produce an error estimate. The reason is essentially that it is not easily possible to compute error matrices with the parameters varied such that χ^2 is increased by 1 because of the location of the local minimum that constitutes the solution of the fit. If the χ^2 function rises by less than 1 before it decreases again in any direction of parameter-space, this procedure does not produce a solution. A more detailed discussion of stability and error determination issues will be given in section 8.3.

In order to overcome that difficulty, one can use an estimation procedure that uses the parabolic error of the three parameters given by the fit. This error is defined as the change of the parameter necessary to increase χ^2 by 1, for each parameter separately. The difference to the "full" mathematical error treatment lies in the fact that correlations between the parameters are not taken into account. Additionally, it is assumed that χ^2 varies parabolically with the variation of a parameter, hence the expression. This can be achieved with the HESSE option in [59]. The parabolic approximation is calculated from finite differences, which implies a dependence of this procedure of the behaviour of the χ^2-function around the minimum.

This error estimate is an upper bound to the "true" error by MINOS, and can therefore be taken as a measure. The estimate produces an error band around the fit value for any given scale Q^2 in the ξ range under consideration by taking all permutations of $\alpha \pm \Delta\alpha$, $\beta \pm \Delta\beta$, and $\gamma \pm \Delta\gamma$ at Q_0^2, evolving to the scale Q^2 and taking the spread as the error.

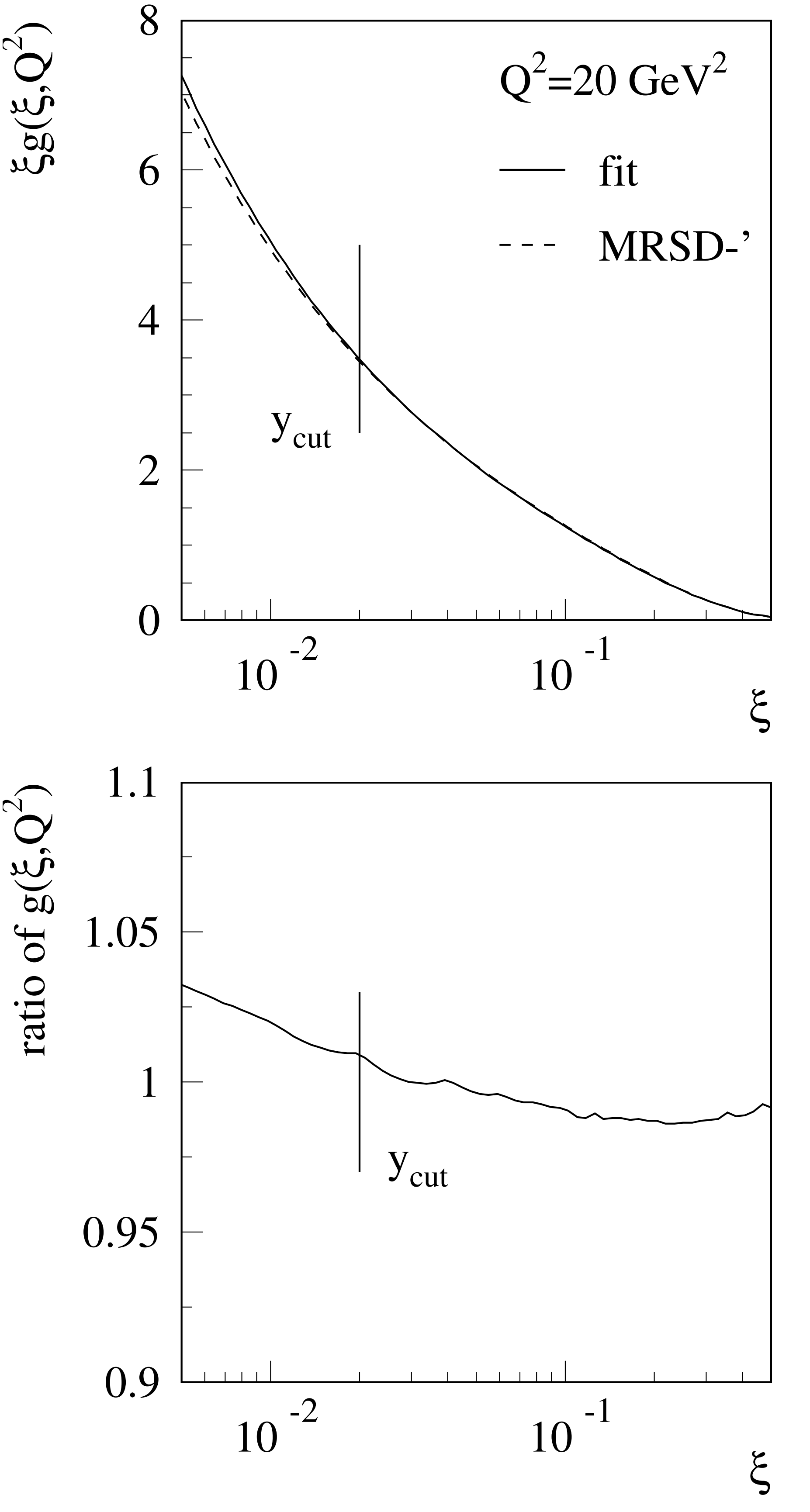

Figure 4.3: Comparison of fitted gluon density from known σ_{2+1} with MRSD-' (top) and the ratio (bottom).

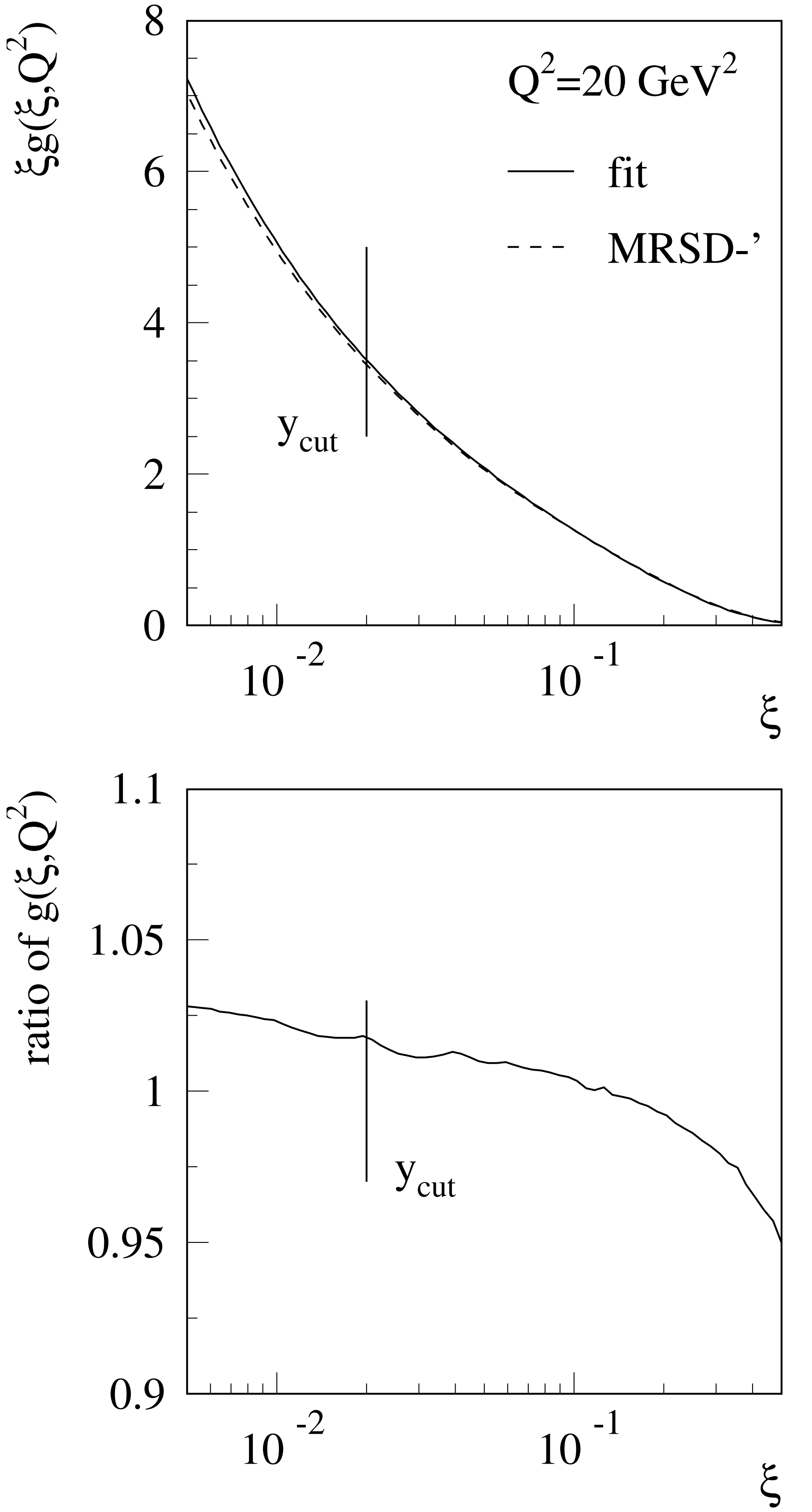

Figure 4.4: Comparison of fitted gluon density from known R_{2+1} with MRSD-' (top) and the ratio (bottom).

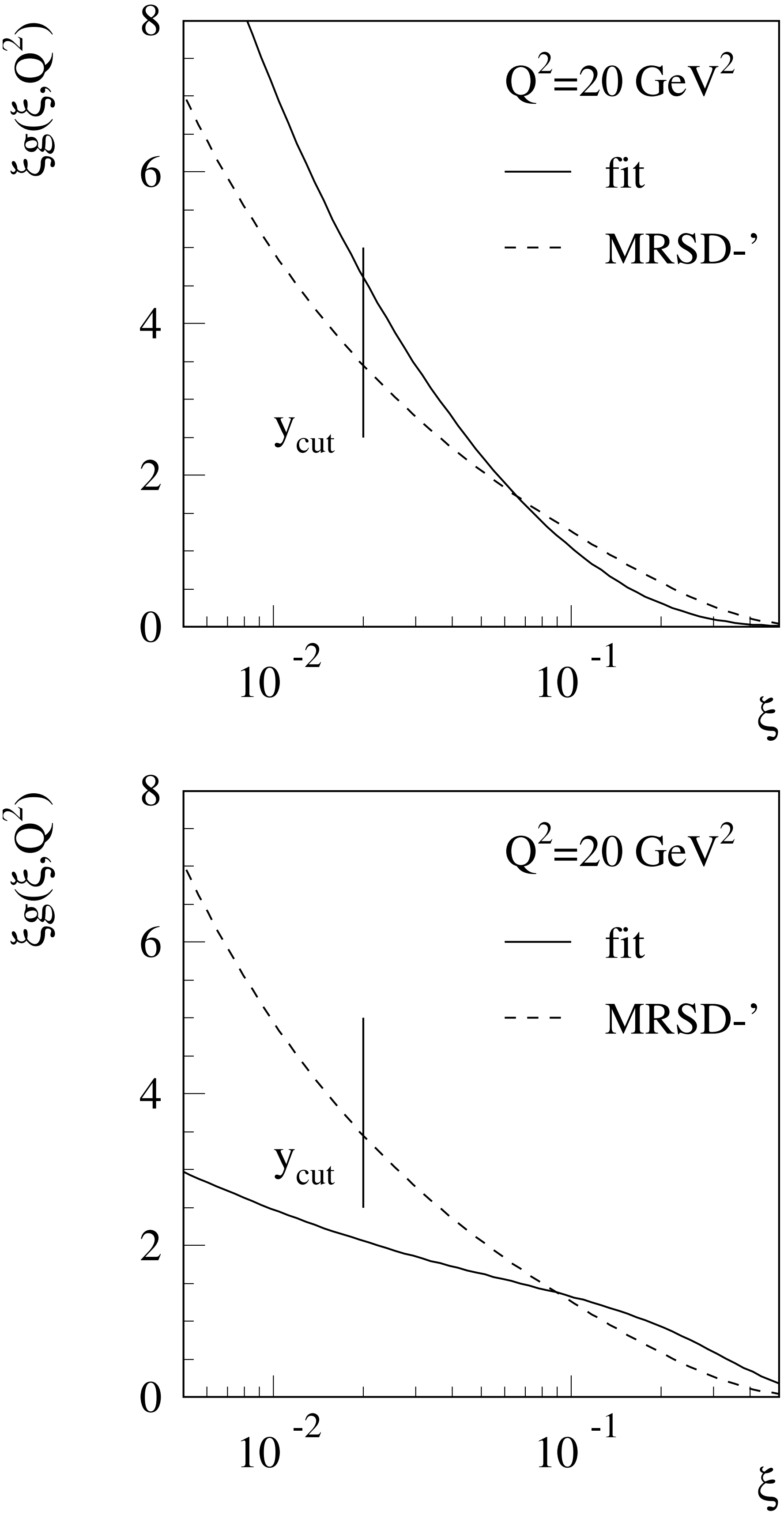

Figure 4.5: Demonstration of the fit sensitivity by introducing extreme additional points at $\xi = 0.005$. In the upper plot, a large contribution was added and increased the fit, while in the lower plot, a small point bent the fit downwards.

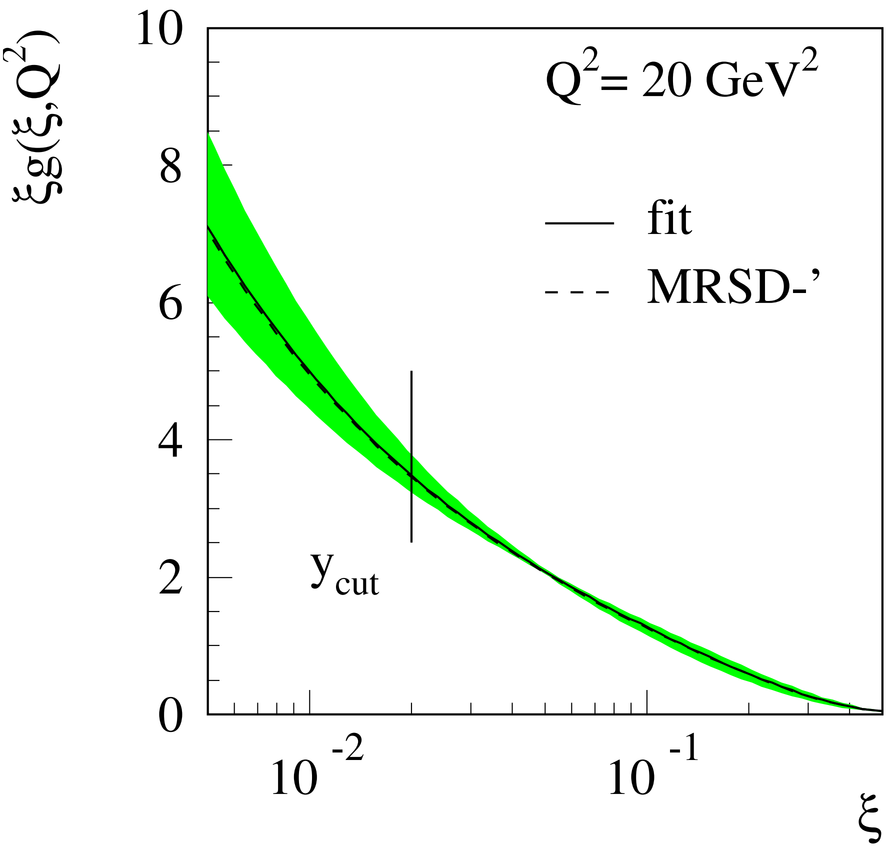

Figure 4.6: Comparison of fitted gluon density from known R_{2+1} with MRSD-' by introducing a $\sim 5\%$ error into the fit, which resulted in the shaded area.

Since so far, no data, but well known functions were fitted back, the choice of the error was arbitrary. Taking not only one bin in Q^2, but several, and distorting the jet rate fed to the fit artificially by about 5%, while introducing a 5 % error into the fit, the error band shown in figure 4.6 was obtained. As can be seen, the band opens up with decreasing ξ in the ξ region where the fit was extrapolated, as one would expect in a region where no constraints are imposed by the input to the fit. This underlines the confidence in the method.

Chapter 5

HERA and H1

The HERA collider, which is shown in figure 1.1 and already briefly mentioned in chapters 1 and 2, shall be described in some more detail to mention facts that are relevant to the analysis of DIS data. The same applies to the description of the H1 detector. A detailed discussion of the H1 apparatus can be found elsewhere [62], where also references are given for HERA.

Since the analysis presented here uses only the positron runs of 1994, only these conditions will be covered.

5.1 The HERA Machine

In order to reach the high energies that HERA was designed for, the magnetic fields used to keep particles on track must be quite strong. Both beams are accelerated in the same tunnel, using superconducting magnets for the protons ($B = 4.68$ T). The particles are arranged in bunches separated by 96 ns, having a design length of 11 cm (electrons) and 0.8 cm (protons). Some of these bunches, the so called "pilot bunches," have no colliding partner in order to study background conditions. The 1994 positron runs used 153 proton and 153 positron bunches combined with 15 positron and 17 proton pilot bunches. This setup led to currents of typically 41 mA for protons and 17 mA for positrons. The specific luminosity was about $1.4 \cdot 10^{30}$ cm^{-2}s^{-1} on average.

5.2 The H1 Detector

A picture of the H1 detector can be found in figure 1.2 where the components described below are clearly visible. Because of the higher proton energy compared to electrons (and positrons), the center of mass system is moving along the proton direction, and therefore the detector has an asymmetric shape along the axis.

The luminosity system is set up at $z = -33$ m to detect electrons scattered through the Bethe-Heitler reaction $ep \to e'\gamma p$ and to detect photons at $z = -100$ m, using a crystal calorimeter which has an energy resolution of $\sigma(E)/E \approx 0.10\sqrt{E/\mathrm{GeV}}$. The electron angle is less than 5 mrad with respect to the beam direction.

The two components of the detector being most important for the analysis described here are the **L**iquid **Ar**gon Calorimeter (LAr) [63] and the **B**ackward **E**lectro**m**agnetic **C**alorimeter (BEMC), positioned around the tracking chambers.

5.2.1 The Tracking Chambers

The detector consists of tracking devices located around the beampipe to record tracks of the charged particles emerging from the interaction point. Here, the **C**entral **T**racking chamber (CT) and a **F**orward **T**racking (FT) device together with a **B**ackward multiwire **P**roportional **C**hamber (BPC) cover the polar angle range of $7° < \theta < 175°$.

Due to the finite bunch length, the vertex has to be determined by the tracking chambers, as it may deviate from the nominal interaction point up to ± 50 cm. This and the measurement from the BPC are combined to a determination of the electron scattering angle with a resolution of about 6 mrad.

5.2.2 The Liquid Argon Calorimeter

In the LAr, the scattered electrons and also hadrons deposit most of their energy, and leaking energy can be measured in the instrumented iron which is located in the return yoke of the superconducting solenoid. The solenoid itself provides a uniform magnetic field of 1.15 T parallel to the beam axis in the region where the tracking chambers are situated.

The LAr covers the polar angle range of $4° < \theta < 153°$ and the azimuthal range completely. It is composed of an **e**lectro**m**agnetic **c**alorimeter (EMC) and a **ha**dronic **c**alorimeter (HAC) section, where the EMC contains lead absorbers equivalent to a depth of 20–30 radiation lengths and the HAC is built of steel absorbers. Overall, the depth of the LAr lies in the range of 4.5–8 hadronic interaction lengths. The calorimeter is highly segmented in both parts, comprising around 45000 geometric cells, which have an electronic noise per channel of 10–30 MeV, as expressed in 1σ equivalent energy. In testbeam measurements, it has been shown that the LAr calorimeter modules have energy resolutions of $\sigma(E)/E \approx 0.12\sqrt{E/\mathrm{GeV}} \oplus 0.01$ for electrons and of $\sigma(E)/E \approx 0.5\sqrt{E/\mathrm{GeV}} \oplus 0.02$ for charged pions [62, 64]. These references also describe the energy reconstruction.

The hadronic energy scale and resolution are known to a precision of 4% from the balance of transverse momentum between hadronic jets and 20% from the measurement of the scattered electron in DIS events. The absolute energy scale uncertainty for electrons is about 3%.

5.2.3 The Backward Electromagnetic Calorimeter

The BEMC is mainly used to trigger on electrons and measure them in DIS processes with low Q^2. It has 22 radiation lengths and covers the polar range of $151° < \theta < 177°$ in the backward region of the calorimeter, which corresponds to an acceptance region for Q^2 of about $5 \leq Q^2 \leq 100$ GeV^2. The energy resolution has been determined to be about $\sigma(E)/E \approx 0.10\sqrt{E/\mathrm{GeV}}$ with a constant contribution of 3%. Adjusting the observed energy spectrum to the kinematic peak (the region in phase space where the outgoing electron has roughly the same energy as the incident) reduces this uncertainty to 1%.

Additionally, a scintillator hodoscope is assembled behind the BEMC to veto background events caused by protons by comparing the arrival time to the nominally expected.

Chapter 6

The Monte-Carlo Machinery

The description of particle collisions needs techniques to unfold the observed particle tracks and energies in the detector back to hadronic and also partonic level. Since there is no such procedure to perform this backward correction directly, one has to rely on Monte-Carlo techniques to describe the collision with a theoretical model on the parton level, then perform a hadronization process according to model assumptions and subsequently simulate the passage of the particles through the detector.

The simulated events thus obtained can be fed into the same reconstruction software that also deals with the actual data events recorded by the detector, and by comparing both, conclusions can be derived about the accuracy of the assumed models. In an iterative process, the different steps in the simulation chain can be modified and "tuned" to data.

However, a "physical understanding" of the data is achieved only when theories can be tested by data, or physical quantities like QCD parameters are determined by using the simulation information to correct to hadron and/or parton level and then performing a comparison to the actual underlying theoretical assumptions.

The events generated are chosen by a pseudo random procedure governed by the cross section of the process and the phase space under study. A more detailed discussion of LO QCD event generators can be found in [31].

All generators mentioned here are available in the so-called "H1-standard", which constitutes an interface to the detector simulation software. The cross section integration programs PROJET, DISJET and MEPJET are not event generators in that sense.

6.1 LEPTO

The event generator program LEPTO 6.3 [65] includes a LO description of the matrix element plus a modeling of higher orders by matching **I**nitial **S**tate and **F**inal **S**tate **P**arton **S**howers (ISPS, and FSPS, respectively) to the four vector kinematics of the generated event. It integrates the total and the (2+1) parton cross section to $\mathcal{O}(\alpha_S)$, i.e. the QCD-Compton- and BGF-events as pictured in figures 3.4 and 3.5. The difference between the total cross section and the (2+1) jet events is attributed to (1+1) events, which can be interpreted like in figure 3.3. Furthermore, the longitudinal structure function F_L can be included into the calculation, yielding the $\mathcal{O}(\alpha_S)$ total cross section. Additional effects such as target mass and "higher twist" effects can be chosen, too.

The (2+1) parton cross sections are calculated in an adaptive way by building a grid which is used as a probability distribution in choosing the required kinematical variables pseudorandomly. The absorption of divergences is done in a phenomenological way, and the parton distributions of the PDFLIB [20] are included to calculate the cross section.

6.1.1 Parton Showers

To approximate the effects of higher orders in the perturbative expansion of the cross section calculation and to take soft interactions into account, parton showers are used. They can be implemented in the initial state, where gluons are radiated off the incoming parton to the hard interaction, and they can be applied to the outgoing state, where partons leaving the hard interaction radiate e.g. gluons, which subsequently shower additional particles.

A parton close to mass shell in the incoming nucleon can start a parton shower by becoming increasingly off-shell with a space-like behaviour ($m^2 < 0$), while the parton radiated is on-shell or time-like ($m^2 > 0$). The parton emitting the cascade then enters the hard subprocess being space-like, while the outcoming partons are either on-shell ($m^2 \approx 0$) or time-like. There, another cascade can be started. The termination of the showering has to be included as a cutoff parameter, which is typically in the range of a m_0^2 of about 1 GeV^2.

The splitting of the partons in the showers is governed by leading logarithm approximations of perturbative QCD and Altarelli-Parisi splitting functions, applying angular ordering (i.e. decreasing opening angles in subsequent branches).

The initial state case is "matched" backwards to ensure four vector momentum conservation. This is a modeling procedure which traces the virtuality of the incoming parton back from the hard interaction with decreasing virtuality down to the on-shell partons in the incoming nucleon.

More details can be found in [65]. The use of a LO matrix element plus the implementation of parton showers is often referred to as the "MEPS model."

6.1.2 Hadronization

The outgoing quarks and gluons of the hard subprocess and the parton showers have to hadronize in order to form color singlets, i.e. hadrons that enter into the detector simulation.

The method used here is the "Lund String" model, where a color string between the colored partons is spanned, denoting the force that exists between them. While the particles are moving apart, the "tension" increases, until the energy is large enough to form new parton-antiparton pairs. This process is repeated until no new particles can emerge because their rest mass is larger than the energy of the string. The model is implemented in JETSET 7.4 [66]. A discussion of the color interactions in the final state can be found in [31].

6.2 SMURF

Another Monte-Carlo event generator that calculates cross sections to $\mathcal{O}(\alpha_S)$ is SMURF [31].[1] It computes the cross sections independently and builds a probability grid in parameter-space, so that the generation of events can be conducted according to that grid for every process separately. This has the advantage of being able to study each process independently, and to make detailed phase space and stability studies.

A concise treatment of FSPS in the JETSET framework is implemented; however, there are no ISPS available so far which are necessary to describe DIS data.

[1] "**S**cattering **M**onte-Carlo **U**sing **R**efined **F**eatures."

6.3 Other Models

There are other models that are trying to describe the hard subprocess and also the subsequent fragmentation and the showering, respectively. Two of them are the **C**olor **D**ipole **M**odel (CDM) implemented in ARIADNE [67], and the cluster fragmentation model provided in HERWIG [68].

The CDM makes the assumption that the color forces between the colored particles can be interpreted as dipoles that radiate and by the virtue of this mechanism create the showering effect. HERWIG assumes clusters that are formed after the hard interaction by the arrangements of color singlets. They are then fragmented and hadronized according to a hadron selection algorithm, taking into account their quantum numbers.

The CDM is used within the LEPTO framework, and has so far failed to describe (2+1) jet rates with sufficient accuracy to be used for a measurement. The same applies to the cluster fragmentation model. They are being constantly improved, and there might be a better agreement between the predictions and data in the future. At the moment, they provide a valuable tool to estimate the systematic error incurred by the model dependence due to the use of one specific model.

6.4 DJANGO

The event generator program DJANGO6 [69] combines the hadronic description of the hard scattering process in the MEPS model and the $\mathcal{O}(\alpha)$ corrections on the leptonic side. They were originally included in the program HERACLES, and DJANGO forms an interface between LEPTO and HERACLES. The photon emission on the quark side is not yet available.

Especially for high y and low x, the corrections due to QED corrections can be sizable, and the phase space can be distorted to a large degree. Therefore, it is desirable to have a procedure to account for the correction and implement it in the event generator.

The $\mathcal{O}(\alpha)$ corrections can be grouped into three different categories following the poles that appear in the calculation of the corrections:

- **I**nitial **S**tate **R**adiation (ISR), see figure 6.1.
- **F**inal **S**tate **R**adiation (FSR), see figure 6.2.
- The so called "Compton contribution."

Additionally, the one loop corrections account for a virtual vertex correction at the emission vertex of the exchange boson. The Compton contribution plays only a minor role in radiative corrections and is often neglected.

It should be noted that the ISR and FSR both cover the whole radiation phase space, but are peaked collinear to the emitting lepton. This interpretation of the phase space is meaningful only in the leading logarithmic approximation. Beyond the leading logarithmic approximation, the separation is not unique! The photon emitted from ISR will in most cases move parallel to the incoming lepton. The FSR photon will most likely be parallel to the outgoing lepton.

In both cases (and in this approximation), the four momentum of the exchanged boson will be reduced. Therefore, the modeling of these processes can be performed in a two step procedure. First, the cross section for ISR and FSR is calculated (by taking into account approximations and cutoffs for the collinear poles), and then the reduced four momentum of the exchange boson

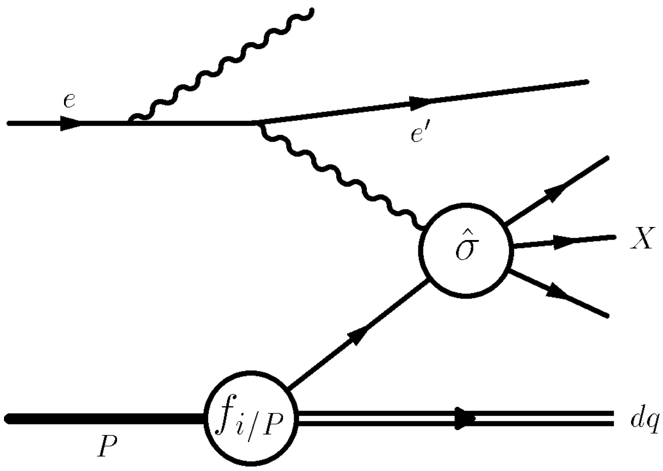

Figure 6.1: Generic diagram of QED initial state radiation.

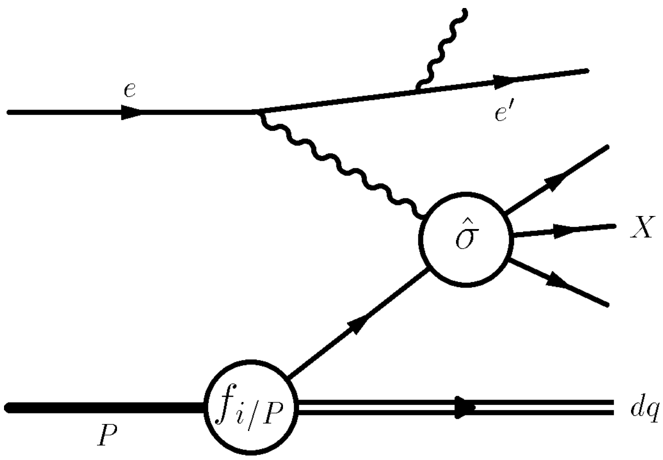

Figure 6.2: Generic diagram of QED final state radiation.

will be interfaced to LEPTO, which treats this interaction essentially as a process at lower energy.

So far, DJANGO has not been used in the description of the data, since this interfacing has only become reliable recently, after removing ambiguities in the treatment of common parameters, such that DJANGO with radiation switched off could result in the same cross sections as LEPTO. It has been shown, however, that in the phase space region typically chosen for jet analyses, the influence of radiative corrections is small, typically less than 5% (see also [25]). This could be confirmed for the analysis presented here.

6.5 Comparisons

The LO cross sections of the programs described above should agree within the integration accuracy of typically a few per cent. Comparisons between SMURF and LEPTO were performed in [31]. The discrepancies pictured in chapter 4 of [31] could be resolved by ensuring the consistent treatment of α.

LEPTO and DJANGO6 without radiative corrections were compared and yielded agreement once the different treatment of mass thresholds in the BGF cross section calculation was implemented in DJANGO6. One has to make sure, however, that not only the real, but also the virtual radiative corrections are switched off.

The comparison between LEPTO, SMURF and PROJET (in LO) resulted in good agreement.

In all the comparisons mentioned, the conditions have to be equal, of course, in order to ensure valid results. Frequent mistakes are made by not aligning the following items:

- The parton density functions have to be identical. Cutoffs and approximations have to be treated consistently.
- The phase space cuts have to be identical and internal cuts have to be analogous.
- α and α_S have to be calculated to identical orders, respectively, and Λ_{QCD} has to be the same.
- The jet definition scheme and the cutoff to regulate divergences has to be the same. This refers particularly to LEPTO, which has different ways to treat the cutoff and might therefore not cover the same phase space region.
- If a large phase space region is to be covered, one has to make sure that the integration accuracy is still sufficient. If necessary and possible, the number of support points has to be increased.
- The threshold for heavy quark production and the number of flavors used have to be the same for the programs compared.

Chapter 7

Event Selection

The analysis presented here relies on the data taken by the H1 detector in the year 1994. After applying basic criteria, the data sample amounted to 2.74 pb^{-1}. This sample is the same as also used for the α_S analysis [70, 71, 72].

7.1 Data Sample and Event Selection Cuts

The construction of the H1 detector as described in chapter 5 makes it necessary to distinguish between two subsamples that roughly correspond to the kinematic range $Q^2 < 100$ GeV^2 as covered by the BEMC, and $Q^2 > 100$ GeV^2, which is covered by the LAr.

Both subsamples had to fulfill the following basic requirements:

- The event vertex had to lie within ± 30 cm around the maximum in the vertex distribution, which was at $z = +5$ cm.
- $W^2 > 5000$ GeV^2. This cut ensures that the two hard jets have an invariant mass squared of at least 100 GeV^2 for (2+1) jet events, if $y_{cut} > 0.02$. Here, W^2 was calculated using the double angle method, relying on the angle of the scattered electron and the angle of the total hadronic system and not on the jet multiplicity.

For the BEMC-sample, the requirements were:

- The absolute four momentum transfer Q^2 had to lie within the range 10 GeV$^2 < Q^2 <$ 100 GeV^2.
- The polar angle of the scattered electron had to fulfill $160° < \theta_{e'} < 173°$.
- The energy of the scattered electron $E_{e'}$ had to be larger than 14 GeV. This cut corresponds to $y \lesssim 0.5$ and thus eliminates background from photoproduction. As motivated in section 6.4, radiative DIS events are also largely suppressed and radiative corrections to the cross section are kept small.

The LAr-sample had to meet the following criteria:

- $Q^2 > 100$ GeV^2.
- $E_{e'} > 11$ GeV.

- $y < 0.7$, again to suppress photoproduction and radiative DIS events.

- $10^\circ < \theta_{e'} < 150^\circ$. This cut ensures that the scattered electron is truly contained in the LAr and that the transition region between the LAr and the BEMC is avoided.

- The quantity $\delta = \sum_{clus}(E - P_z)$ had to meet the requirement 38 GeV $< \delta <$ 70 GeV. Here, E is the energy and P_z the longitudinal momentum of the detector cluster. The lower cut excludes events where the scattered electron stemming from photoproduction remains inside the beam pipe. Similar to the cut in y, this cut also suppresses radiative corrections to the cross section.

For both samples, Q^2 and y were calculated from the energy and the polar angle of the scattered electron. After these cuts, the sample contained 32482 events for $Q^2 < 100$ GeV^2 and 6127 events for $Q^2 > 100$ GeV^2.

7.2 Jet Analysis

The jet analysis was performed using the modified JADE algorithm as described in section 3.4.1. To ensure that the NLO corrections are smaller than 30 % for all values of x and Q^2, y_{cut} was set to 0.02. In order to contain the jet event fully in the LAr, where the hadronic energy is well measured, the maximum jet angle θ_{jet} was restricted to 145°.

As was observed in earlier analyses to determine α_S [25, 73], the jet rate predicted by PROJET NLO calculations is much smaller than the measured rate, especially at lower Q^2 values. The reason for this is the emission of multi gluon radiation from the initial state, which is modeled by parton showers as described in section 6.1.1. The Monte Carlo generator can therefore also be used to determine cuts which suppress this effect.

With decreasing Q^2, also lower values of x are reached. In order to reduce the higher order effects, i.e. parton showers, efficiently, an additional jet cut is necessary.

Introducing the quantity for (2+1) jets

$$z_p \equiv \frac{1}{2}(1 - \cos\theta^\star_{jet}), \tag{7.1}$$

with $\theta^\star_{jet}$ being the smaller angle of the two jets in the photon parton center of mass system and $0 < z_p < 0.5$, one can reduce the effect of parton showers considerably, if one applies a cut of $z_p > 0.1$. This can be seen in figure 7.1 for the LAr sample and for $Q^2 > 100$ GeV^2, where $\theta_{jet} > 10^\circ$ was required. The curves are normalized to the number of events. It is demonstrated that the shape of the data is well reproduced by the detector simulation and also by the MEPS model on parton level. The PROJET calculation predicts however less (2+1) jet events with small z_p values ($z_p < 0.1$) compared to the MEPS model. A cut in z_p alone is not sufficient because (2+1) jet events originating from parton showers are also concentrated at small jet angles. This can be seen in fig. 7.1b where the distribution of the smallest jet angle in a (2+1) jet event is plotted.

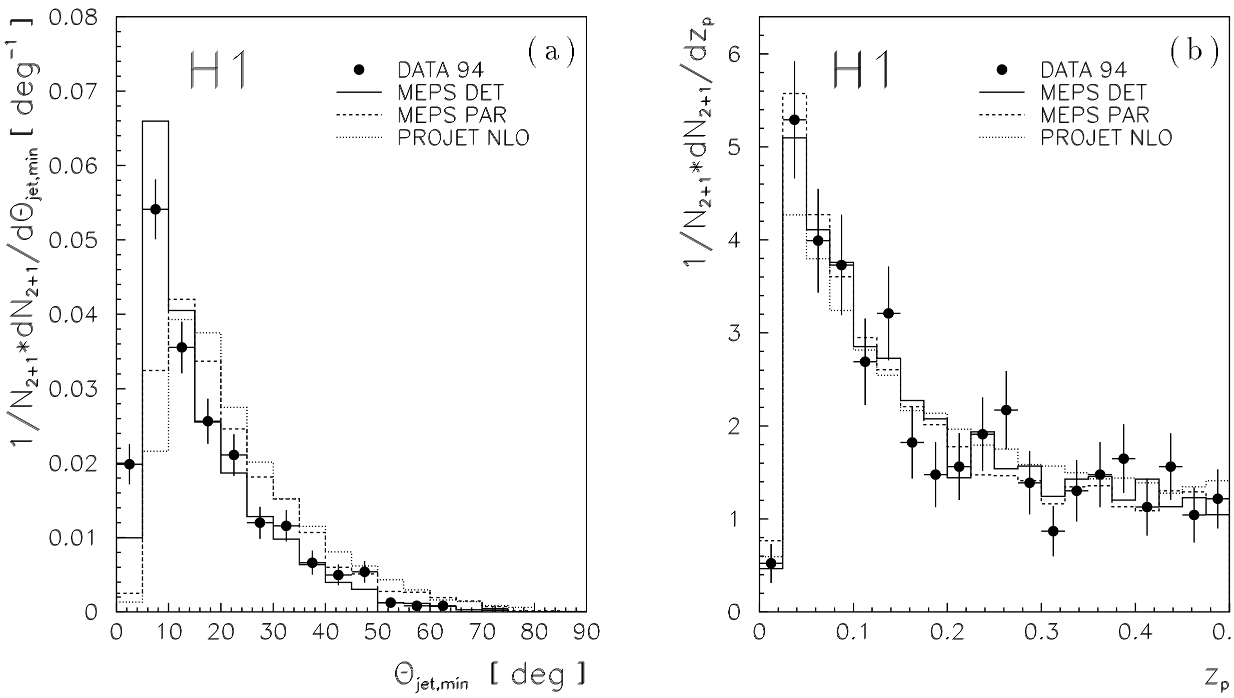

Figure 7.1: (a) The $\theta_{jet,min}$ distribution of the $(2+1)$ jet events for $Q^2 > 100$ GeV^2, $z_p > 0.1$ and $\theta_{max} = 145°$; (b) The z_p distribution of the $(2+1)$ jet events for $Q^2 > 100$ GeV^2, $\theta_{jet} > 10°$ and $\theta_{max} = 145°$. In both figures the data are represented by the points with statistical error bars only. The solid line represents the prediction of the MEPS model at the detector level and the dashed line the prediction of the same model at the parton level. The PROJET calculation is given by the dotted line [75].

As motivated in [70], the cut optimization was performed by using the following criteria:

- The jet rates predicted by PROJET should be close to the jet rates in the MEPS model on parton level, both in absolute value and shape.
- The data should be described well by MEPS on the detector level.
- The correction factor applied to correct back the to parton level from the detector level should be small.

In order to be able to go to lower values of Q^2, where both the gluon induced part of the cross section and the influence of the parton shower increase, the cuts in θ_{jet} and z_p do not suffice to fulfill the criteria mentioned above.

An additional cut in θ_q has been found [74]. It is defined in the laboratory frame as the angle of the recoiling quark in the quark parton model and is calculated from the electron variables alone, being very efficient in removing excess parton shower events. The effect of this cut can be seen in figure 7.2. For the further analysis, only events with $\theta_q < 100°$ were accepted.

The combination of the three cuts θ_{jet}, z_p and θ_q removes parton shower effects efficiently and allows for the extension of the sample to lower Q^2. The distribution in the (x, Q^2) plane

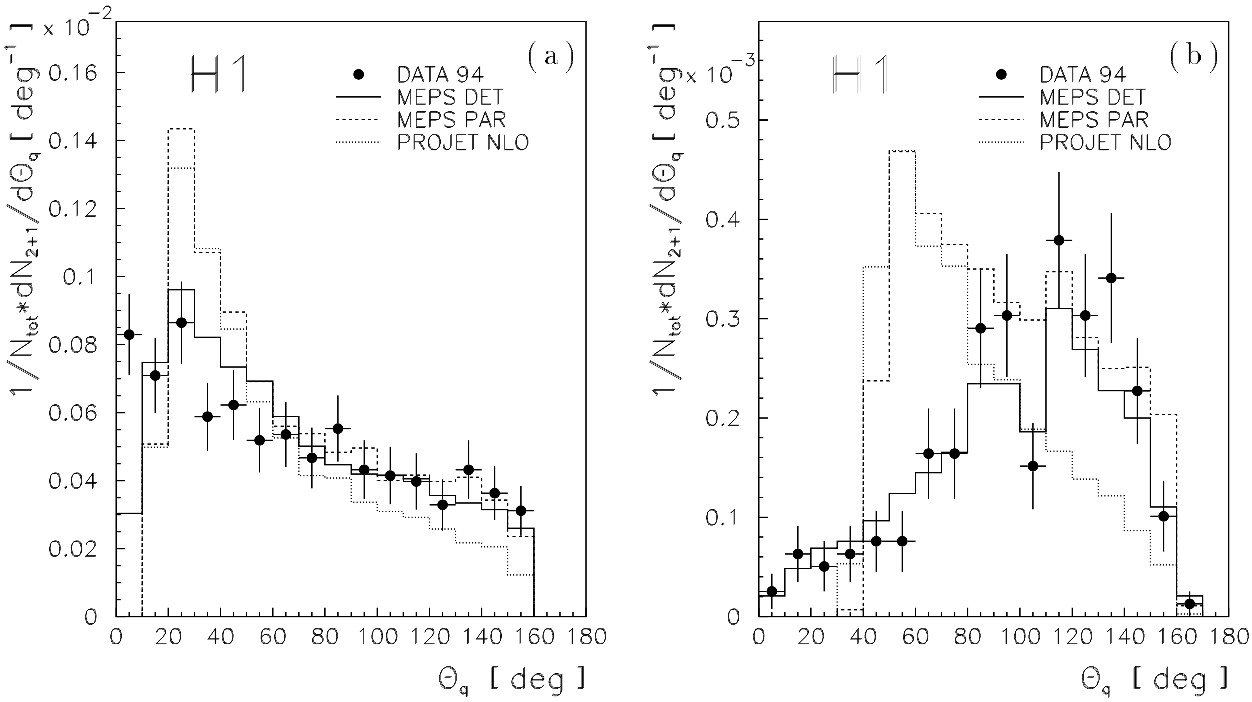

Figure 7.2: The θ_q distribution of the $(2+1)$ jet events. (a) for $Q^2 > 100$ GeV^2 and $z_p > 0.1$. (b) for $40 < Q^2 < 100$ GeV^2, $z_p > 0.1$ and $\theta_{jet} > 10°$. All curves are normalized to the total number of events. The error bars of the data (black points) correspond to the statistical errors only [75].

can be found in figure 7.3. Examples of a (1+1) and a (2+1) jet event are given in figures 7.4 and 7.5, respectively. Apart from the side and front view of the events, the energy deposition is plotted in the (η, φ) plane.

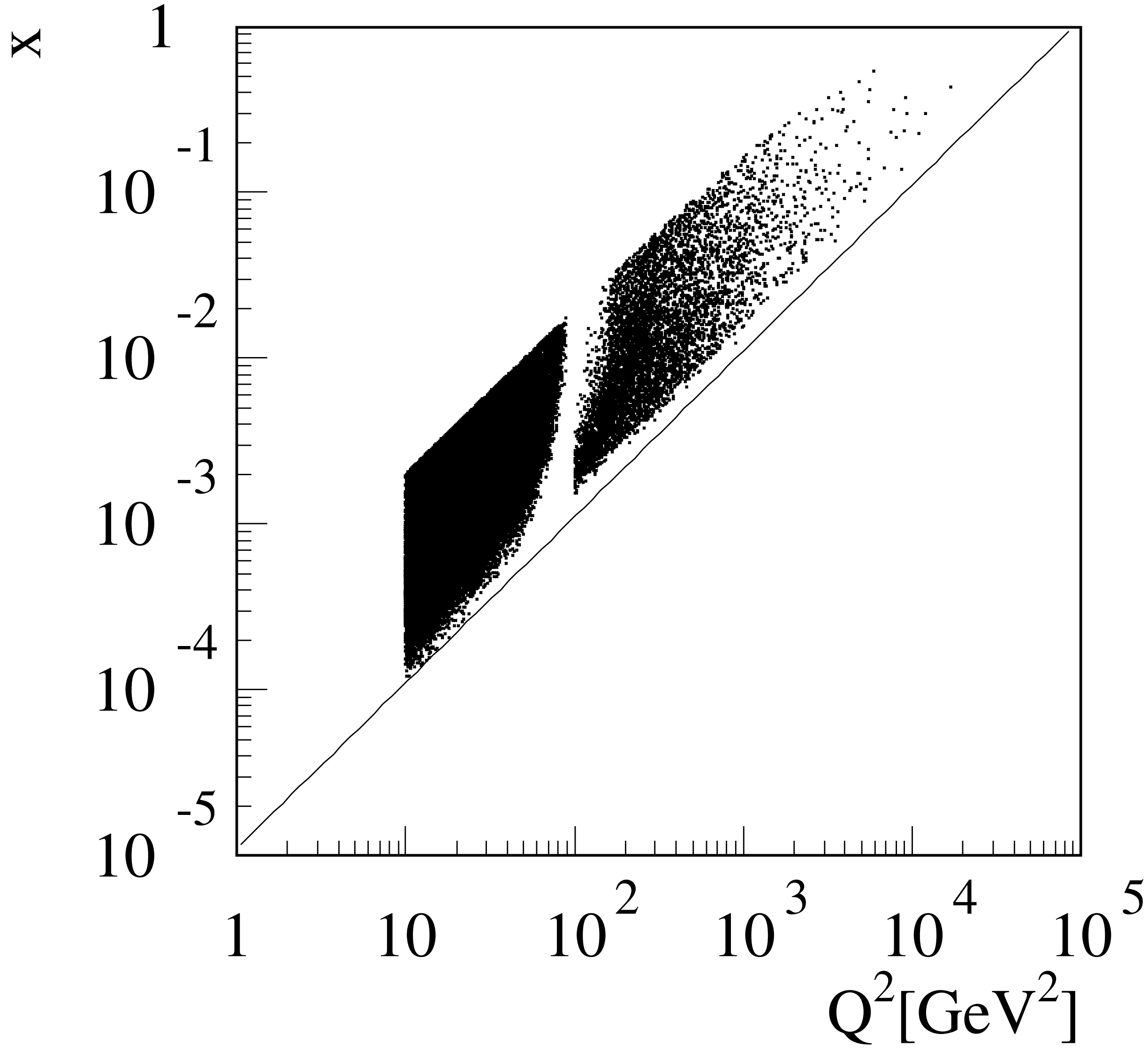

Figure 7.3: Event distribution of the data sample in the (x, Q^2) plane [76].

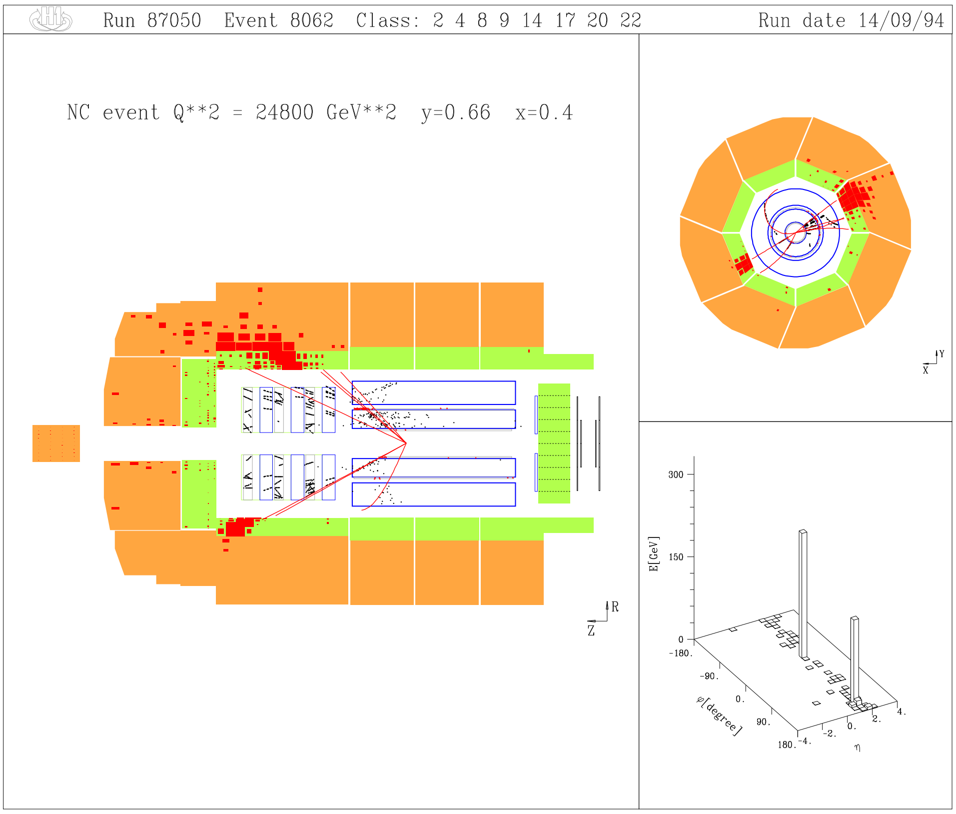

Figure 7.4: Example of a (1+1) jet event.

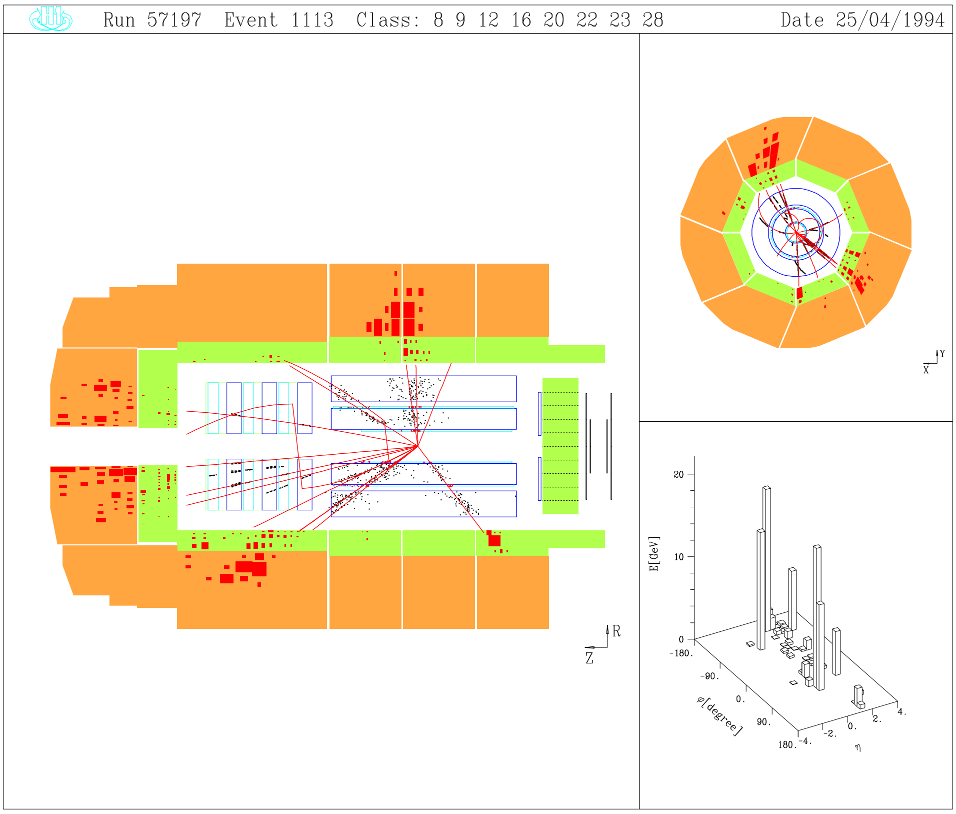

Figure 7.5: Example of a (2+1) jet event.

Chapter 8

Results

8.1 Jet rates

With the data sample described in chapter 7 and the Mellin transform technique as introduced in chapter 4, the fitting of the gluon density can be performed. Analogously to the α_S analysis, data were corrected to parton level using correction factors determined by Monte-Carlo simulation.

The uncorrected and corrected jet rates, as well as the PROJET calculations for different Λ_{QCD} (as used in the α_S fit) for the JADE scheme are shown in figure 8.1 [75].[1]

The "gap" between the lowest bin and the higher bins in Q^2 can be explained by the θ_q cut. The Q^2 binning follows [32].

8.2 Error Analysis

The determination of the errors follows a similar procedure as in [70, 71]. However, to be applicable to the determination of the gluon density, the errors were translated into jet rate errors per Q^2 bin, according to three categories: statistical, systematic experimental and theoretical error.

To determine the systematic experimental error, the following studies were made [75, 77]:

- The cut in z_p was varied between 0.1 and 0.2 for $\theta_{jet} > 10°$, while leaving the other parameters at their central values. In addition, the cut in θ_{jet} was varied between 8° and 15°, and θ_{max} between 140° and 150°, with the other parameters fixed at their central value, respectively.
- The cut in θ_q was varied between 95° and 120° with the other parameters fixed at their central values.
- The hadronic energy scale in the detector simulation and data reconstruction was varied by $\pm 4\%$ for $\theta_{jet} > 10°$.

The final experimental systematic error was taken to be the maximum spread of the rate deviations from the scenarios discussed above. This automatically takes into account correlations between the different scenarios and constitutes an upper bound of the "true" error.

[1] An analogous demonstration of the different parameters of the gluon fit in one plot is not feasible, since three parameters constitute a complicated three-dimensional space. A discussion of related features is given in section 8.3.

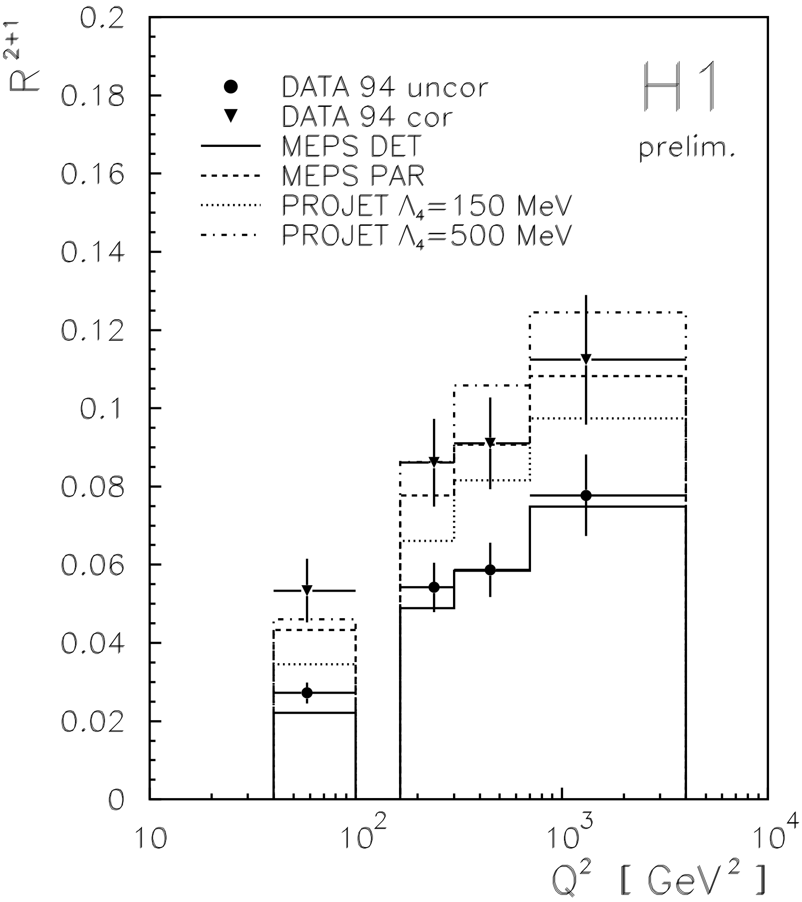

Figure 8.1: Jet rates obtained with the JADE scheme [75]. Only statistical errors are shown. In addition, PROJET calculations obtained with different Λ_{QCD} are plotted.

The theoretical error was determined by the following studies, performed on generator level:

- The model dependence in the JETSET fragmentation was studied by varying the parameters a of the LUND model functions between 0.1 and 1, the σ_{pt} parameter and the intrinsic k_t of the struck quark between 0.44 and 0.7 GeV. In addition, the cut-off parameters which control the parton shower generation were varied between 1 and 4 GeV and the lowest value y_{cut} for which the ME calculations were carried out, was varied between 0.005 and 0.015.

- Instead of LEPTO the HERWIG [68] Monte-Carlo model with its entirely different treatment of parton showering and hadronization was used to calculate the correction factors. The Q^2 and y_{cut} dependence of the jet rates is described at the 10–20% level.

- The factorization scale μ_f^2 and the renormalization scale μ_r^2 were varied between $Q^2/4$ and $4Q^2$.

- The uncertainty of the α_S measurement was taken into account by varying the jet rates by the error of the world average [27] transformed to the mean scale Q^2 of the bin under consideration.

	Q^2 [GeV^2] / Error			
Error source	40...100	100...300	300...700	700...4000
Statistics	0.00814	0.01122	0.01174	0.01658
θ_{jet} and z_p cut	0.01792	0.02526	0.02544	0.04115
θ_q	0.00766	0.00717	0.00778	0.00352
Hadronic Energy Scale	0.00522	0.00504	0.00830	0.00882
Parton Shower and Hadronization Param.	0.00998	0.00871	0.00740	0.01168
QCD Monte Carlo Model	0.00405	0.00739	0.00569	0.00705
μ_r^2, μ_f^2	0.01056	0.01642	0.00532	0.00562
α_S	0.00259	0.00553	0.00673	0.00758

Table 8.1: Changes in jet rates by different scenarios, used to determine the error. Values taken partly from [75, 77].

The uncertainty induced by the different parton density function in the calculation of the quark induced cross sections can be neglected, since the quark densities are reasonably well known in the phase space region under consideration. The uncertainty stems mainly from the gluon density.

Again, the theoretical error per bin was determined by taking the spread of the rate uncertainty. The total error was determined by adding quadratically the statistical, the systematic experimental and the theoretical error. Details can be found in table 8.1.[2]

To fix the uncertainty in β for "high" ξ, where no data are available from H1 (see figure 7.3),[3] an additional point was introduced into the fit at $\xi = 0.2$ and $Q^2 = 20$ GeV^2, taking the spread of the world error as determined in [21] into account. This increased the fit stability.

As a MINOS analysis is not possible due to the accuracy of the Mellin transforms of a few per cent, the error was estimated by varying the parameters within their errors and taking the spread as the error band. Details of the stability discussion can be found in section 8.3.

The χ^2 is low (< 0.5), indicating that the error is overestimated. Note that a "crossover" is expected for varying the parameters to determine the error [78]. This is caused by the fact that the resulting error band is an enveloppe of the extreme gluon densities which intersect. Since the band is essentially an upper estimate of the true error, the resulting "kink" in the band can be accepted.

To facilitate a comparison, several parton density parameterizations are plotted in figure 8.2. The gluon density with the total error band is plotted in figures 8.3 for $Q^2 = 20$ GeV^2 and $Q^2 = 100$ GeV^2, obtained with the JADE scheme. As can be seen, the error band decreases with increasing Q^2. On one hand, this is an evolution effect, but on the other hand, this is also amplified by the fact that the fit is dominated by an input around $Q^2 = 100$ GeV^2.

8.3 Stability of the Fit

The reason why the MINOS error determination from [59] cannot be used lies in the particular parameter-space properties. They are illustrated in figures 8.5 and 8.6, which were produced by plotting the χ^2 distribution for two parameters and one parameter, respectively, while the

[2]It should be noted that figure 8.3 uses slightly larger errors due to a different treatment of the variation of θ_{jet} and z_p. This is, however, not of real importance for the discussion presented here.

[3]Since $\xi > x$, this figure can illustrate the lack of data for high ξ.

remaining parameters were held fixed at a value near the expected fitting result. As one can see, the resulting shapes are rather complicated. In the case where only one parameter was varied, a clear parabola like behaviour emerges. Taking three dimensions, the picture is less clear. Then non-diagonal effects of the correlation matrix distort the rotational-paraboloidal shape and produce even absolute minima at the edges of the parameter-space.

When the error is determined by MINOS, each time one parameter is varied in such a way that the χ^2 is changed by $+1$, and then the others are refitted to produce a new minimum. This procedure is only safe if the minimum under consideration is "deep" enough and a refitting does not find new minima and thus destroys the fit.

Therefore, the procedure HESSE of [59] is used which explicitly recalculates the error matrix by determining the second derivative matrix with finite differences and subsequently inverting it. This method is much more stable, since finite differences are used and a refitting is avoided. It is not as accurate as MINOS, but gives an upper boundary of the error. Therefore, it can be employed for the purpose of fitting the gluon density. A more detailed discussion of error treatment can be found in [58, 59].

These features of the χ^2 function can also be used to explain why a fit using only the three upper bins in Q^2 cannot necessarily be used. Apart from the fact that the gluon induced contribution is smaller, the system is not overconstrained as in the four bin case. Then a fit can still lead to a satisfactory minimum. However, a HESSE analysis is normally not possible anymore. Therefore, the errors obtained in the three bin case can only be taken from the minimum search and are an estimate of the order of magnitude, but no longer accurate. Then, only the approximation of parabolic errors can be given. Interestingly, it is of the same order of magnitude.

The discussion above also motivates why it is important to give the right initial step size and error estimate as starting conditions for the fit, as only properly chosen parameters will ensure that the local minimum is not left and the desired result is achieved.

8.4 Recombination Scheme

Since the development of the program MEPJET, one is able to study NLO cross sections for various jet algorithms. Since Mellin transforms can be calculated presently only with PROJET, there is no feasible procedure at the moment to perform a gluon density fit with MEPJET.

However, since the recombination scheme in PROJET is not unambiguous, it has been shown that recalculating the NLO cross sections with MEPJET and redetermining α_S yields large discrepancies to PROJET [71]. This is in part due to the fact that the recombination schemes used on the experimental side and the theoretical side are not the same with PROJET. The smallest deviation has been found for the P recombination scheme.

In addition, in PROJET, terms proportional to $y_{cut} \cdot W^2/\text{scale}^2$ are neglected, and increasing deviations are therefore found with increasing W^2.

The α_S determination from jets is becoming more and more a precision measurement. Therefore, these differences are important and have to be taken into account. For the gluon density, however, the errors are still rather large, and so the effects of these deviations are much smaller at the moment.

Since this direct measurement can only use PROJET, a remedy has to be found to circumvent the problems described above. One immediate consequence is that the analysis has to be performed in the P scheme. When this is done, the stability of the fit improves, and also the two error bands representing the inclusion of statistical and systematic experimental error on one

Q^2 [GeV^2]	PROJET	MEPJET (p scheme)	Data (p scheme)
40 ... 100	0.0377	0.0508	0.04159
100 ... 300	0.0718	0.0756	0.07869
300 ... 700	0.0889	0.0869	0.08587
700 ... 4000	0.1054	0.0979	0.09168

Table 8.2: Jet rates obtained by PROJET and MEPJET compared with data for the JADE algorithm. The cuts as described in the text were applied. Taken partly from [75].

side, and the theoretical error additionally on the other side lie within each other much better, see figure 8.4.

If one then estimates the deviation of PROJET from MEPJET by comparing the (2+1) jet rates and takes this error into account for the lowest Q^2 bin by adding it quadratically, the error band is modified only slightly. The resulting fit can be seen in figure 8.7, the different jet rates are shown in table 8.2. The resulting error band itself is partly reduced, even though the total error in the lowest bin increases. This can be traced back to the error determination procedure and mirrors the effect of a different fit result and a subsequently different parameter-space for the error determination as discussed above.

Another possible remedy is the introduction of a "correction factor" for the (2+1) cross section into the fit. Doing this globally, again the error band is not changed much, see figure 8.8. This indicates that the deviation from MEPJET is still within the error range already determined independently, and thus does not make a big effect. Of course, when this analysis is studied further, the decrease of errors will necessitate a much closer look at these discrepancies. However, the resulting "kink" is much more pronounced. This can be due to the chosen mathematical form of equation 4.17, since the choice of a particular function introduces a bias into the capability to describe the desired functional behaviour. Then, the intersection of the possible functions in the error determination procedure can stem from the inherent limitations. It has become pronounced by the improved understanding of the errors and deserves further study.

A more sophisticated correction factor approach would be the correction in bins of W^2 in the Mellin transform calculation. This could be done in one run of PROJET, if one determines W^2 for each cross section weight being calculated, and modifies the weight according to the correction determined in the W^2 bin under consideration [79]. Even if this procedure takes the implicit ξ integration much better into account, which is important from a theoretical point of view, the effects should be small at the current level of experimental accuracy. But it should improve the stability of the fit and smoothen the error band, indicating a more stable situation.

In addition, different cuts in kinematical and jet definition variables could be looked for which reduce the discrepancy between PROJET and MEPJET. One possible cut could be in x, since the agreement for higher x is much better between the two programs. And relying on lower values in W^2 would ensure that the terms neglected in PROJET do not distort the cross section. With the statistics available today, this does not seem to be feasible, because the remaining number of events is too small to perform a meaningful measurement.

Therefore, it would be very desirable to have additional integration programs to study these effects further. Since MEPJET is still recent and cannot be cross checked with independent calculations, the need for additional programs is evident. A new program based on the dipole formalism [47] will shed new light on this issue. In addition, an extension of PROJET is necessary in the future to be able to calculate Mellin transforms properly and investigate the effects in more detail.

8.5 x-Distribution

An interesting question is, whether the binning can be changed from Q^2 to x, since this seems to be more natural with respect to the quantity under consideration, the gluon density. However, for several reasons, this does not seem to be advantageous at the moment. As can be seen from figure 8.9, which shows an x distribution for the complete Q^2 range and with the cuts described above, a binning in x would mean the subtraction of large terms to yield a small cross section, as described in [32]. This puts additional requirements on the bin selection and the accuracy with which the Mellin transforms are calculated.

In addition, the shape of the distribution is rather complicated. This stems to some degree from the fact that two samples are used, as can be motivated with figure 8.1, where the BEMC and LAr sample are clearly separated, in addition by a cut in θ_q. A consequence is a more difficult search for a useful binning that fulfills the requirements mentioned above.

In general, $g(\xi, Q^2)$ depends on two input quantities, and therefore, it is not clear *a priori*, which binning is to be chosen. A binning in both x and Q^2 cannot be done right now due to missing statistics.

8.6 Higher Statistics

As was described in [80], higher statistics induced by higher luminosity would enable a much more accurate determination of the gluon density and even a discrimination between several of the parameterizations available today. In [80], two scenarios were studied. One essentially consists of a gluon density measurement with today's luminosity and error analysis. However, the improvements in the error analysis induced by MEPJET are not yet included. Figure 8.10 shows the result, which is essentially similar to the study presented above. In a second scenario, it was assumed that due to a higher luminosity (of the order of 250 pb^{-1}) and lower errors, the theoretical error could be neglected and that the systematic error would be halved. Due to much tighter cuts, the systematics would essentially remain the same, but allow for the dramatic reduction in systematic error. The result is shown in figure 8.11, and it is clearly obvious that a discrimination between different parameterizations will be possible.

Comparing these results with the data analysis presented above, it seems that the improvement caused by the recent theoretical development allows already for a much smaller error band. Therefore, the figures 8.10 and 8.11 should be taken as an illustration of what can be achieved with a substantially increased luminosity.

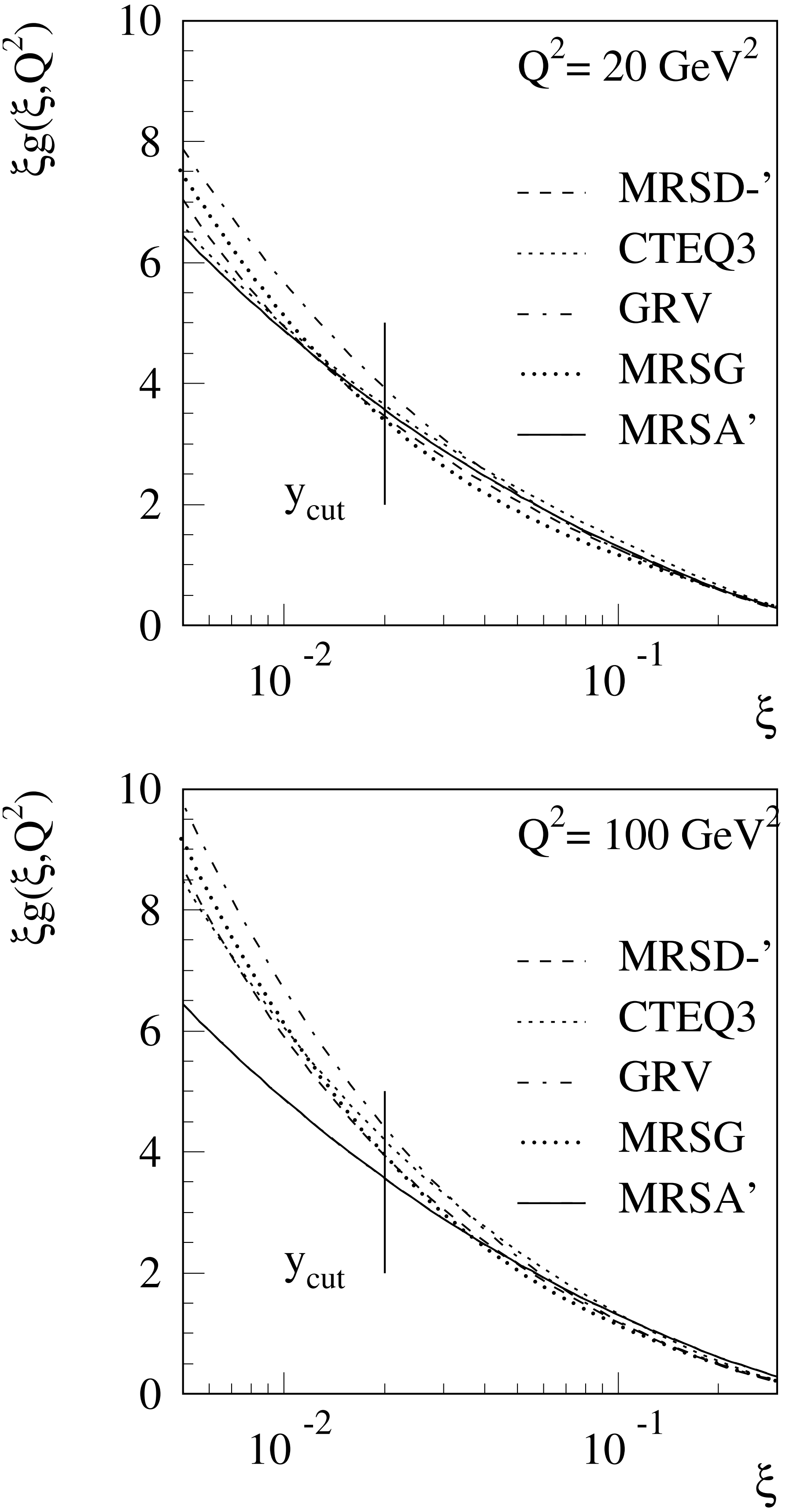

Figure 8.2: Commonly used gluon density parameterizations, plotted for the scales $Q^2 = 20\ \mathrm{GeV}^2$ and $Q^2 = 100\ \mathrm{GeV}^2$.

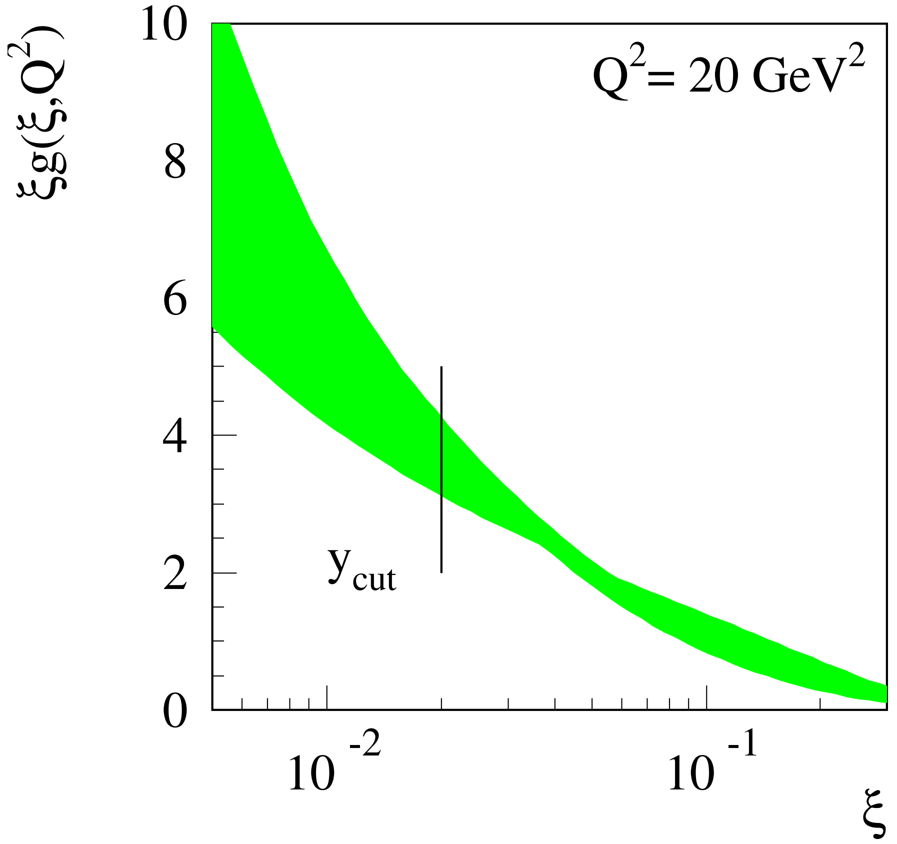

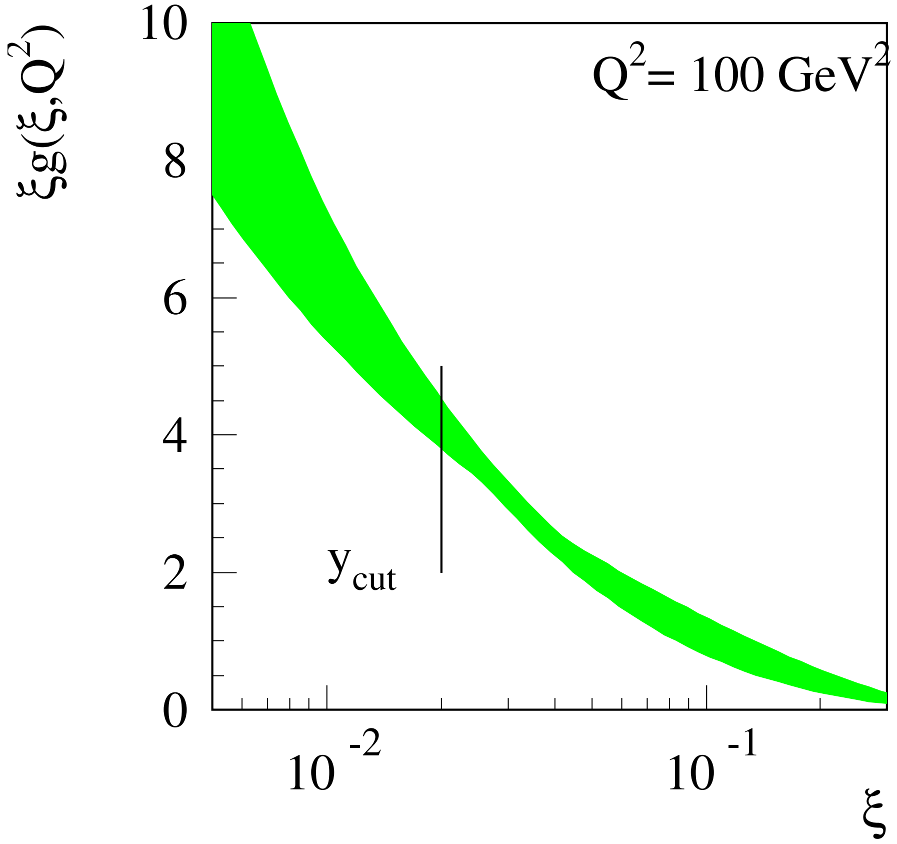

Figure 8.3: Fitted gluon density obtained from data with the JADE scheme, plotted for the scales $Q^2 = 20$ GeV^2 and $Q^2 = 100$ GeV^2. The shaded area denotes the total error band.

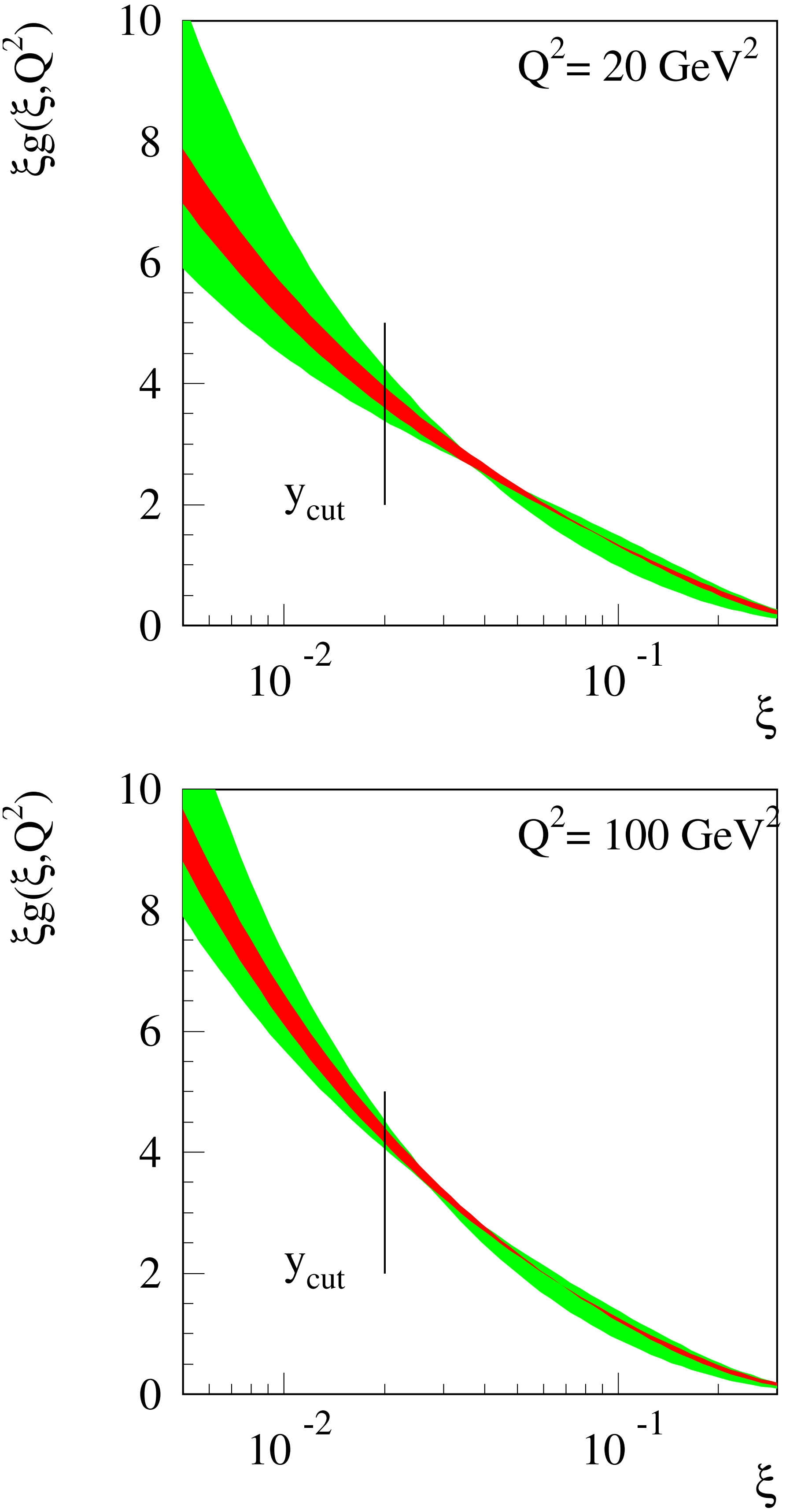

Figure 8.4: Fitted gluon density obtained from data with the P scheme, plotted for the scales $Q^2 = 20$ GeV^2 and $Q^2 = 100$ GeV^2. The inner shaded area includes the statistical and systematic error, the outer band includes the total error.

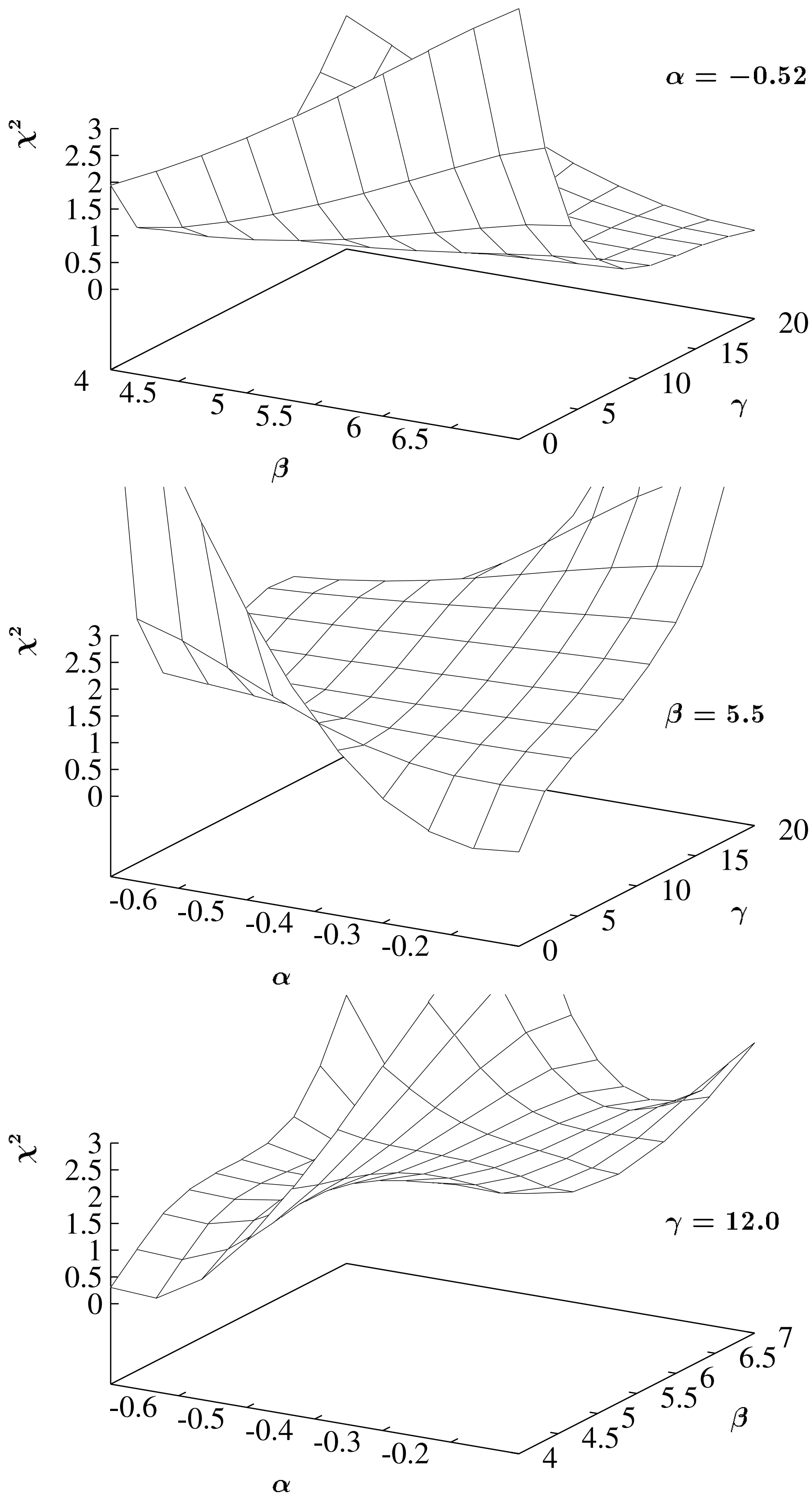

Figure 8.5: Two-dimensional χ^2 distributions for different parameter-space projections obtained for a typical fit close to the minimum. The third parameter was held fixed at the given value.

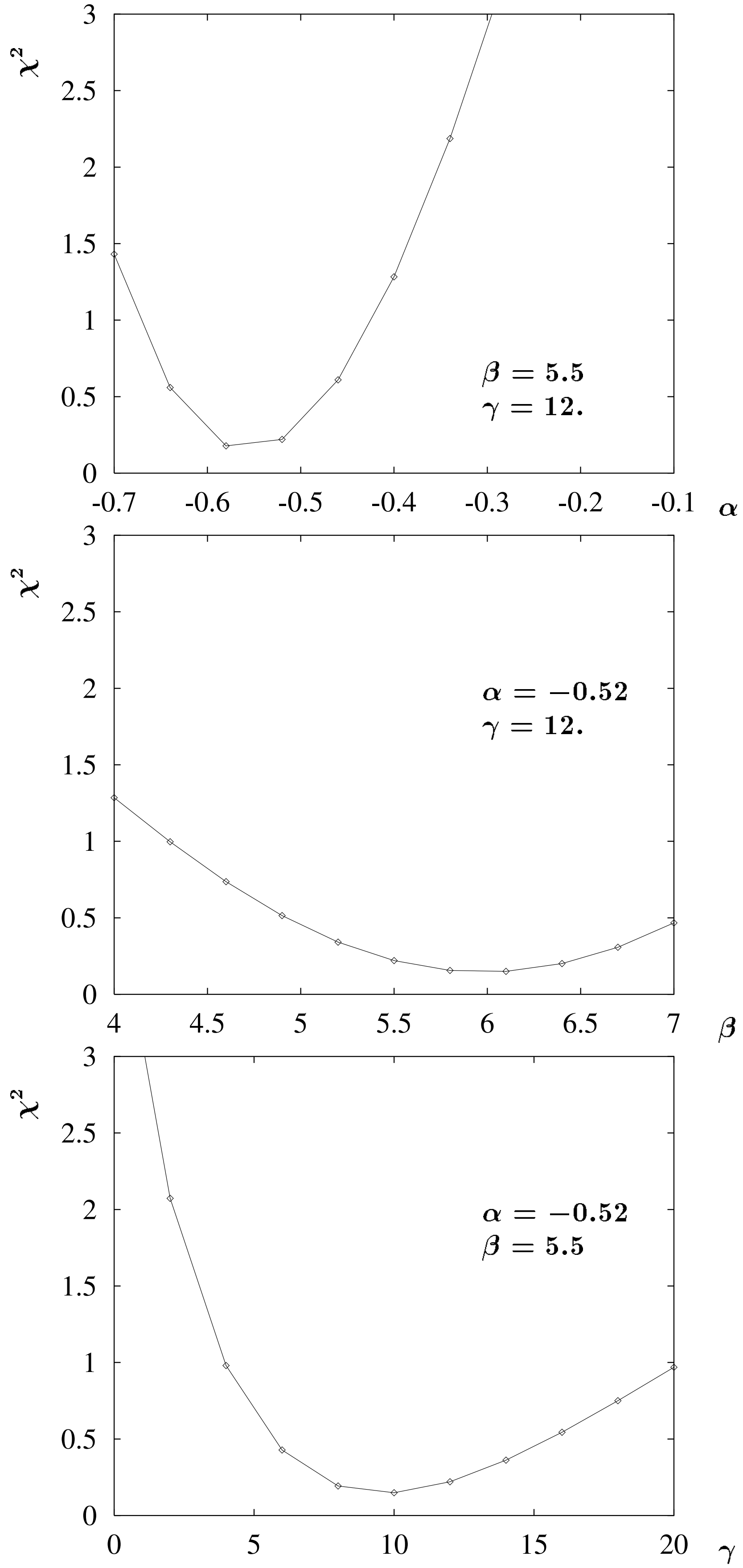

Figure 8.6: One-dimensional χ^2 distributions for different parameter-space projections obtained for a typical fit close to the minimum. The other two parameter were held fixed at the given values.

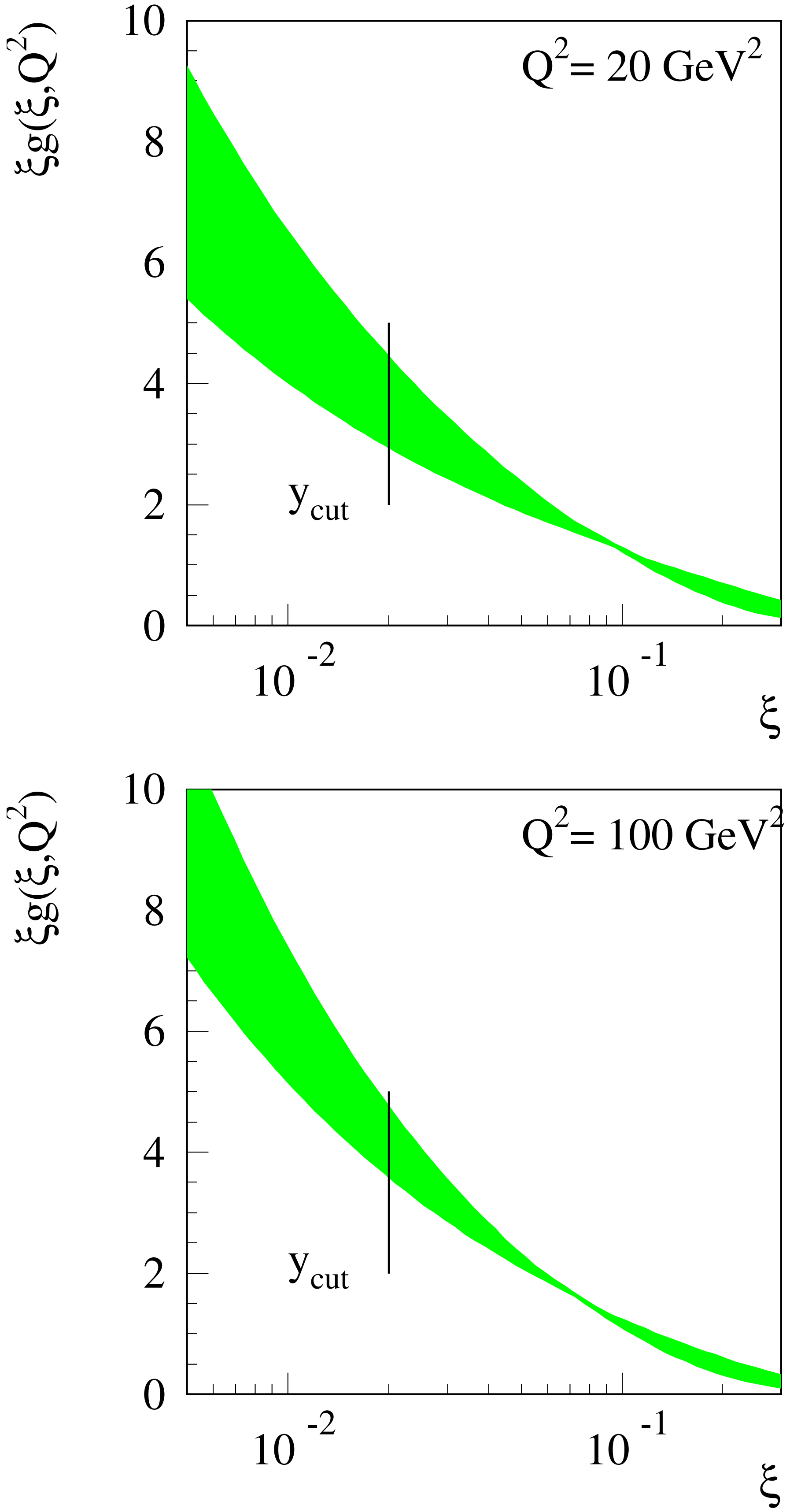

Figure 8.7: Fitted gluon density obtained from data with an additional error for the lowest Q^2 bin as estimated by MEPJET, plotted for the scales $Q^2 = 20$ GeV^2 and $Q^2 = 100$ GeV^2. The shaded area denotes the total error band.

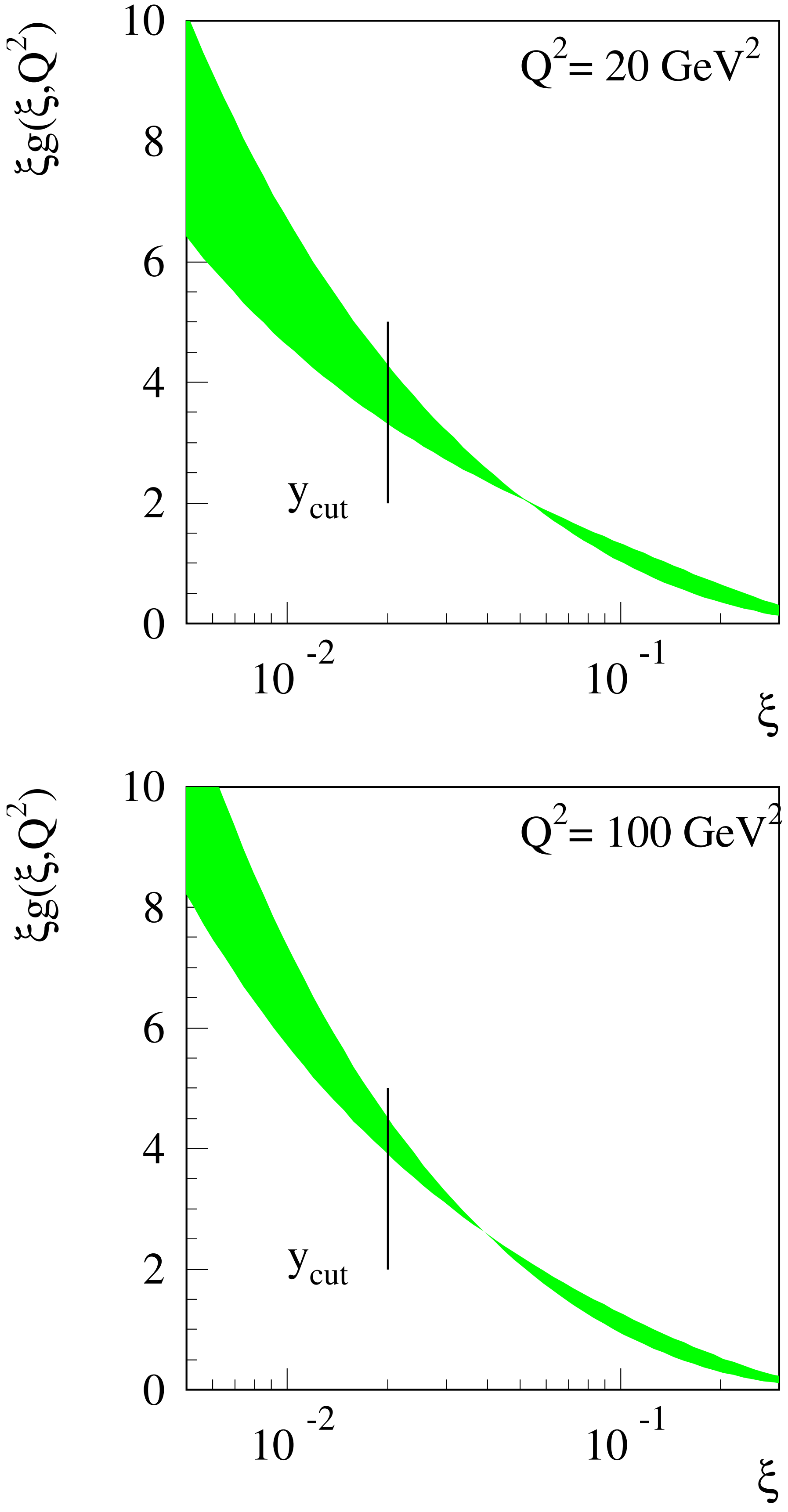

Figure 8.8: Fitted gluon density obtained from data with a correction factor for the lowest Q^2 bin as determined by MEPJET, plotted for the scales $Q^2 = 20$ GeV^2 and $Q^2 = 100$ GeV^2. The shaded area denotes the total error band.

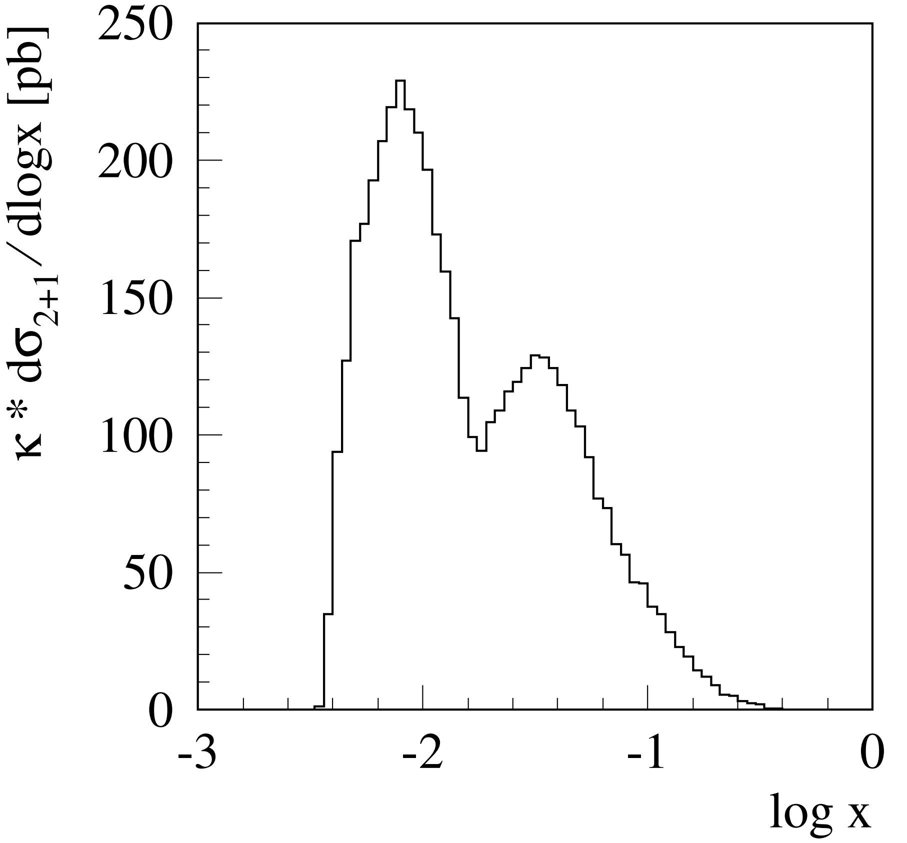

Figure 8.9: The x-distribution of the data sample with the cuts used in this analysis; κ denotes the bin-width factor.

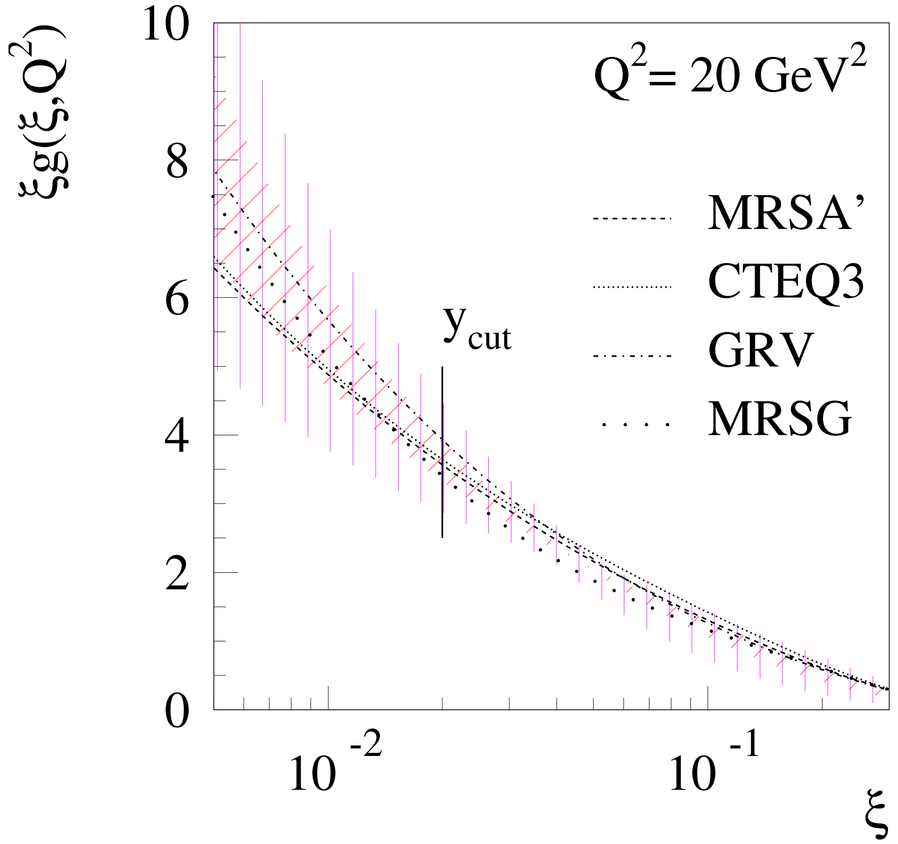

Figure 8.10: Fitted gluon density obtained with a scenario available with today's luminosity, plotted together with commonly used gluon density parameterizations. The inner error band includes statistical and systematic error, while the outer band covers the total error. For details see text and [80].

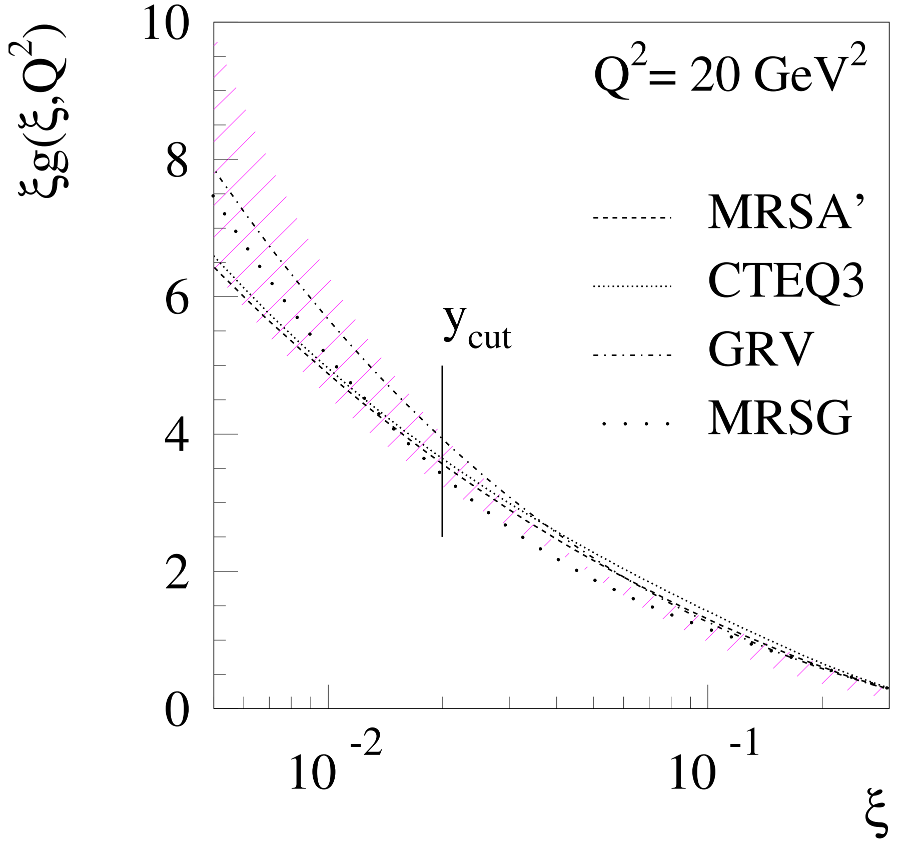

Figure 8.11: Fitted gluon density obtained with the high luminosity scenario, plotted together with commonly used gluon density parameterizations. The error band includes the total error, assuming a large reduction due to tighter cuts. For details see text and [80].

Chapter 9

Conclusion and Outlook

The determination of the gluon density in NLO continues to be a very interesting subject. Since the gluon density is still the least well known parton density, a more precise determination is very desirable for a better understanding of the proton structure.

It has been shown in this analysis that it is possible to directly measure the gluon density in NLO from jets. The Mellin transform method was introduced, and it was shown that it is possible to perform a fit of the gluon density, because the method allows to reduce the large computing time needed for the repeated calculation of NLO cross sections. A fit is the only way to determine $g(\xi, Q^2)$ in NLO, since the gluon momentum fraction cannot be reconstructed any more. In order to be meaningful, parton densities have to be determined at least in NLO because of scale uncertainties.

The Mellin transform technique itself is universal, i.e. can in principal also be applied to other types of collisions. One application might be the extension to the determination of the gluon density from $p\overline{p}$ collisions at the Tevatron.

The measurement was performed and a gluon density was fitted from (2+1) jet data taken by H1. The region covered is $0.02 < \xi \lesssim 0.1$ for a Q^2 range of $40 < Q^2 < 4000\mathrm{GeV}^2$.

The ξ region could previously only be investigated indirectly by performing global fits to world data. This is the first time that an explicit constraint is put on the gluon density in this domain. It connects the measurements performed with fixed-target experiments, direct photon production of pp collisions and the determination of the gluon density via scaling violations of F_2. Furthermore, it is the first direct NLO measurement of this quantity.

Other jet algorithms and a refined theoretical understanding will enable an extension of the phase space region to lower ξ. In addition, a higher luminosity of HERA will allow for much tighter cuts to reduce systematic uncertainties, which will eventually lead to a discrimination between given parameterizations.

Another tool that would be very helpful is a NLO event generator program. Here, much progress will have to be made to deal with negative weights that are used today, but such a generator program would open the door to a complete NLO description on the experimental side. At the same time, the improvement in the correction factor description would reduce systematic uncertainties further.

Since the determination of α_S is maturing into a precision experiment, a simultaneous measurement of the gluon density and α_S will be possible, thus enabling the determination of Λ_{QCD} in one experiment. This combination will necessitate further systematic and theoretical studies, since then the world knowledge of these quantities will not enter the determination anymore, contrary to the determination presented here.

Therefore, the analysis of jets and the extraction of important QCD quantities will be an interesting field in the future, and it is important to continue the investigation.

Appendix A

Moment Relations

The aim of this appendix is to fill in the technical details which have been omitted in [32]. We have to prove the following statements [81]:

- $h_{an} = \int_a^1 \mathrm{d}x \int_x^1 \frac{\mathrm{d}\xi}{\xi} \left(\frac{a}{\xi}\right)^n \sigma_i\left(\frac{x}{\xi}, x\right)$:

$$\begin{aligned}
h_{an} &= \int_0^1 \frac{\mathrm{d}u}{u} u^n h_a(u) \\
&= \int_a^1 \frac{\mathrm{d}u}{u} u^n h_a(u) \quad (\text{since } h_a(u) \equiv 0 \text{ for } u < a) \\
&= \int_a^1 \frac{\mathrm{d}u}{u} u^n \int_a^{a/u} \mathrm{d}x\, \sigma_i\left(\frac{x}{a/u}, x\right) \\
&= \int_a^1 \frac{\mathrm{d}\xi}{\xi} \left(\frac{a}{\xi}\right)^n \int_a^{\xi} \mathrm{d}x\, \sigma_i\left(\frac{x}{\xi}, x\right) \quad (\text{by a change of variables } u = a/\xi) \\
&= \int_a^1 \mathrm{d}x \int_x^1 \frac{\mathrm{d}\xi}{\xi} \left(\frac{a}{\xi}\right)^n \sigma_i\left(\frac{x}{\xi}, x\right). \qquad \text{(A.1)}
\end{aligned}$$

- $\Sigma_a = \Sigma_{aa}$:

$$\begin{aligned}
\Sigma_{aa} &= \int_a^1 \frac{\mathrm{d}\xi}{\xi} f_{i/p}(\xi)\, h_a\left(\frac{a}{\xi}\right) \\
&= \int_a^1 \frac{\mathrm{d}\xi}{\xi} f_{i/p}(\xi) \int_a^{a/(a/\xi)} \mathrm{d}x\, \sigma_i\left(\frac{x}{a/(a/\xi)}, x\right) \\
&= \int_a^1 \frac{\mathrm{d}\xi}{\xi} f_{i/p}(\xi) \int_a^{\xi} \mathrm{d}x\, \sigma_i\left(\frac{x}{\xi}, x\right) \\
&= \int_a^1 \mathrm{d}x \int_x^1 \frac{\mathrm{d}\xi}{\xi} f_{i/p}(\xi)\, \sigma_i\left(\frac{x}{\xi}, x\right) \quad (\text{by observing that } a < x < \xi < 1) \\
&= \Sigma_a. \qquad \text{(A.2)}
\end{aligned}$$

Appendix B

Program Parameters

The program PROJET allows the determination of Mellin transforms and the subsequent writing to a file for further usage. The interface that is necessary to enable PROJET to do this is described below.

Furthermore, the format is documented how the transform file is written, such that it can be read by the evolution and fitting package. A description of the most important routines of this package conclude this appendix.

B.1 PROJET-switches

The steering of PROJET is essentially identical to the "pure" version as described in the PROJET manual. However, in order to enable PROJET to calculate transforms, the main program had to be modified and additional cuts had to be implemented in the function IUSERCUT. These modifications are documented in the code. An overview of the steering parameters is given in table B.1.

The start of the moment calculation loop is indicated by putting the following line into the steering file:

```
-4,0
```

B.2 Special PROJET-COMMONs

In PROJET, the integer variable IHAMPEL must be set to 1 by hand to allow for "negative" parton densities that will occur during moment calculation due to complex transforms. This is done by the steering parameter 10016:

```
      COMMON /HAMPEL/
     &        IHAMPEL
```

It should be noted that the standard PDFLIB package tests parton density values returned from the calculation routine and sets them to zero, if negative values are found. Therefore, the internal private routine in PROJET has to be used to branch to the moment calculation routine which is implemented in STRPRIV.

Other COMMON blocks used internally are documented in the code.

switch #	possible values	default	description
10016	0,1	0	switch for negative allowed pdfs
12001 – 12020	—	0	reserved for PDFLIB steering, not used
12030	0	0	if 0, moment loop can be started by "-4"
12031	-1,0,1	0	internal, determines $\mathcal{R}$e or $\mathcal{I}$m transform part
12032	0	0	internal
12033	1–32	1	start of loop for moment points
12034	1–32	32	end of loop for moment points
12050	-1–2	0	switch for parton distribution in private routine
12052	-1,0	0	internal, has to be 0
12053	-1,1	1	internal, has to be 1
12053	0–2	2	internal, has to be 2
12054	0,1	0	internal, has to be 0
12055	0,1	0	internal, has to be 0
12056	0,1	0	internal, has to be 0
12057	0,1	0	allows only gluon (0) or quark (1) induced σ
12058	0,1	0	if 1, used for the computation of $\tilde{\sigma}$
12099	0,1	0	select normal PROJET (1) or moment version (0)
12151		0.	value a for moment calculation
12152		0.	fixed scale in STRPRIV; if ≤ 0, not used
12155		0.	z_p cut; if < 0, no cut
12156		0.	θ_q cut (in degrees); if < 0, no cut
12157		0.	$\theta_{jet,min}$ (in degrees) according to 12058
12158		180.	$\theta_{jet,max}$ (in degrees) according to 12058
12201			file name to write transforms to
12202			title of fit

Table B.1: Private switches and parameters used for the moment calculation in PROJET. The numbering scheme of PROJET is used. "Default" denotes the standard setting by the steering file. $\mathcal{R}$e and $\mathcal{I}$m represent the real and imaginary part of the transforms, respectively.

B.3 File Formats

To exchange data between the calculation of Mellin transforms in PROJET and the fitting program which uses the evolution code of [82], two files are needed. The first file contains the support points, which can be generated by uncommenting the appropriate lines in the evolution code. Once this file exists, it has to be read by the PROJET main program. The path has to be hardwired in the present version; unit 41 is used.

The second file contains the Mellin transforms. After the fit title, a reference cross section is written as an unformatted double precision variable to unit number 42. It is followed by the error, and subsequently two integer numbers that are set to zero. Then the transforms are written. Each line contains the transform in double precision, the integration error and two integer switches, IUSERPAR(30) and IUSERPAR(31). The first indicates whether the real or imaginary part was written, which alternates. A "1" stands for the real part, while a "2" denotes the imaginary part.

After the last transform is written, the file is terminated in the following way:

```
-1.000000000000000      -1.000000000000000              -1          -1
```

More details can be found in the code, which is amply commented.

B.4 Support Points for Transform Inversion

The numerical inversion of the Mellin transform in equation 4.15 makes use of fixed support points, allowing for a non-adaptive 8-point Gaussian quadrature. Since 32 support points are calculated, four subsequent Gaussian quadratures are computed. The boundaries are listed in table B.2. The points are spaced more closely for small z, since here the influence on the integration kernel is largest. Furthermore, $z_{max} = 9$, $c = 1.8$, and $\phi = \pi/2$. The support points within the Gaussian quadrature can be found in [57]. Of course, the normalization to the lower and upper boundary has to be applied.

# of boundary point	1	2	3	4	5
$z_{min/max}$	0.0	1.5	3.0	6.0	9.0

Table B.2: Support point boundaries $z_{min/max}$ for the numerical inversion of equation 4.15 to calculate cross sections via Mellin transforms.

B.5 The Fitting Program

The fitting program is an independent program that has to be run separately. It essentially works as a frame around the evolution package of [82] and performs the fit.

The program itself reads the transforms from file and initializes MINUIT and the evolution package. Once this is done, only the gluon parameters within the routine INPFIT have to be modified. Then, the cross section can be obtained by calling INV in the fitting procedure.

The modifications that were necessary to calculate the cross section by a product of Mellin transforms are documented in the routine INV. In the code, also the COMMON blocks to transfer information between the routines for fitting purposes, are described in detail.

List of Figures

List of Tables

Bibliography

[1] J.D. Bjorken, S.D. Drell, Relativistic Quantum Mechanics, McGraw-Hill, 1964.

[2] J.D. Bjorken, S.D. Drell, Relativistic Quantum Fields, McGraw-Hill, 1965.

[3] C. Itzykson, J.B. Zuber, Quantum Field Theory, McGraw-Hill, 1980.

[4] D.H. Perkins, Introduction to High Energy Physics, Addison Wesley, 1987.

[5] F. Halzen, A.D. Martin, Quarks & Leptons, An Introductory Course in Modern Particle Physics, Wiley, 1984.

[6] Ch. Berger, Teilchenphysik, Eine Einführung, Springer, 1992 (in German).

[7] V.D. Barger, R.J.N. Phillips, Collider Physics, Addison-Wesley, 1987.

[8] CDF collaboration, Phys. Rev. Lett. 74 (1995) 2626.

[9] D0 collaboration, Phys. Rev. Lett. 74 (1995) 2632.

[10] H1 collaboration, DESY 96-039 (1996).

[11] Ch. Berger, DESY 95-209 (1995).

[12] H1 collaboration, Phys. Lett. B369 (1996) 173.

[13] H1 collaboration, DESY 96-163 (1996).

[14] Proc. Workshop "Physics at HERA," DESY, Hamburg, 1987.

[15] Proc. Workshop "Physics at HERA," DESY, Hamburg, 1991.

[16] Proceedings of the workshop "Future Physics at HERA," DESY, Hamburg, 1996, to be published.

[17] M. Glück, E. Reya, A. Vogt, Z. Phys. C67 (1995) 433.

[18] H.L. Lai et al., CTEQ Collaboration, Phys. Rev. D51 (1995) 4763.

[19] A. Martin, R. Roberts, W.J. Stirling, Phys. Lett. B354 (1995) 155.

[20] H. Plothow-Besch, Comp. Phys. Comm. 75 (1993) 396.

[21] W. Vogelsang, A. Vogt, Nucl. Phys. B453 (1995) 334.

[22] W.J. Stirling, talk presented at the Workshop on Deep Inelastic Scattering and QCD, Paris, April 1995.

[23] S. Riemersma, J. Smith, W.L. van Neerven, Phys. Lett. B282 (1992) 171.

[24] H1 collaboration, Phys. Lett. B449 (1995) 3.

[25] H1 collaboration, Phys. Lett. B346 (1995) 415.

[26] S. Bethke, PITHA 95/14, Aachen, 1995.

[27] Particle Data Group, Review of Particle Properties, Physical Review D54 (1996) 1.

[28] U. Bassler, G. Bernardi, Internal H1 note H1-03/93-274 (1993).

[29] U. Bassler, G. Bernardi, DESY 94-231 (1994).

[30] A. Mendez, Nucl. Phys. B145 (1978) 199.

[31] M. Hampel, diploma thesis, PITHA 93/16, Aachen, 1993 (in German).

[32] D. Graudenz, M. Hampel, A. Vogt, Ch. Berger, Z. Phys. C70 (1996) 77.

[33] S. Catani, Y.L. Dokshitzer, B.R. Webber, Phys. Lett. B285 (1992) 291.

[34] B.R. Webber, J. Phys. G19 (1993) 1567.

[35] D. Graudenz, N. Magnussen, in: Proc. Workshop "Physics at HERA," DESY, Hamburg, 1991.

[36] JADE Collaboration, W. Bartel et al., Z. Phys. C33 (1986) 23.

[37] R. Nisius, Ph.D. thesis, PITHA 94/21, Aachen, 1994.

[38] S. Catani, Yu.L. Dokshitzer, B.R. Webber, Phys. Lett. B285 (1992) 291.

[39] J.E. Huth et al., Fermilab-Conf-90/249-E.

[40] Th. Hadig, diploma thesis, PITHA 96/31, Aachen, 1996 (in German).

[41] D. Graudenz, Comp. Phys. Comm. 92 (1995) 65;
D. Graudenz, PROJET4.1, CERN-TH.7420/94.

[42] D. Graudenz, Phys. Lett. B256 (1991) 518;
D. Graudenz, Phys. Rev. D49 (1994) 3291.

[43] G.P. Lepage, Journal of Comp. Phys. 27 (1978) 192.

[44] G. Lepage, Cornell preprint CLNS-80/447 (1980).

[45] T. Brodkorb, E. Mirkes, DISJET manual, Univ. of Wisconsin, MAD/PH/821 (1994);
T. Brodkorb, E. Mirkes, Univ. of Wisconsin, MAD/PH/820 (1994).

[46] E. Mirkes, D. Zeppenfeld, MADPH-95-916.

[47] S. Catani, M.H. Seymour, NLO calculations in DIS at HERA based on the dipole formalism, to be published in the proceedings of the workshop "Future Physics at HERA," DESY, Hamburg, 1996.

[48] J.F. Owens, W.K. Tung, Annu. Rev. Nucl. Part. Sci. 42 (1992) 291.

[49] E. Reya, Phys. Rep. 69, No. 3, (1981) 195.

[50] Handbook of Perturbative QCD: Version 1.0. By CTEQ Collaboration (Raymond Brock, et al.), Fermilab-Pub-93-094, Apr 1993. 233pp. Published in Rev. Mod. Phys. 67 (1995) 157.

[51] M. Glück, E. Reya, A. Vogt, Z. Phys. C53 (1992) 127.

[52] M. Glück, E. Reya, A. Vogt, Z. Phys. C67 (1995) 433.

[53] M. Glück, E. Reya, A. Vogt, Phys. Rev. D45 (1992) 3968, D46 (1993) 1973.

[54] J. Blümlein et al., DESY 96-172, to be published in the proceedings of the workshop "Future Physics at HERA," DESY, Hamburg, 1996.

[55] J. Blümlein et al., DESY 96-199, DESY, Hamburg, 1996.

[56] R. Courant, D. Hilbert, Methoden der Mathematischen Physik, Springer Verlag, Berlin, 1924 (in German).

[57] M. Abramowitz, I.A. Stegun (eds.), Handbook of Mathematical Functions, National Bureau of Standards, 1964.

[58] Frodesen, Skjeggestad, Tøfte, Probability and Statistics in Particle Physics, Universitetsforlaget, 1979.

[59] F. James, Minuit Program Manual, CERN Program Library Long Writeup D506, Version 94.1.

[60] A.D. Martin, R.G. Roberts, W.J. Stirling, Phys. Rev. D47 (1993) 867.

[61] A.D. Martin, R.G. Roberts, W.J. Stirling, Phys. Lett. B306 (1993) 145.

[62] H1 collaboration, DESY H1-96-01, to appear in Nucl. Instr. and Meth.

[63] H1 Calorimeter Group, Nucl. Instrum. Meth. A336 (1993) 460.

[64] H1 Calorimeter Group, Nucl. Instrum. Meth. A336 (1993) 499.

[65] G. Ingelman, LEPTO version 6.3, unpublished program manual; see also: LEPTO 6.1, Proc. Workshop "Physics at HERA," DESY, Hamburg, Vol. 3 (1991) 1366.

[66] T. Sjöstrand, PYTHIA 5.7 and JETSET 7.4, CERN-TH.7112/93;
T. Sjöstrand, Comp. Phys. Comm. 82 (1994) 74.

[67] L. Lönnblad, ARIADNE version 4, Comp. Phys. Comm. 71 (1992) 15.

[68] G. Marchesini et al., Comp. Phys. Comm. 67 (1992) 465.

[69] H. Spiesberger, DJANGO6 version 2.3, unpublished program manual; see also: G.A. Schuler, H. Spiesberger, Proc. Workshop "Physics at HERA," DESY, Hamburg, Vol. 3 (1991) 1419.

[70] H1 Collaboration, talk on α_S at EPS HEP '95, 27/7 to 2/8/1995, Brussels, Belgium.

[71] K. Rosenbauer, on behalf of the H1 collaboration, Determination of α_S and the gluon density, talk given at Workshop on Deep Inelastic Scattering and Related Phenomena (DIS 96), Rome, Italy, Apr. 15 – 19, 1996.

[72] M. Hampel, on behalf of the H1 and ZEUS collaborations, Direct Measurements of the strong coupling constant α_S at HERA, talk given at the XI Topical Workshop on $p\overline{p}$ Collider Physics, Abano Terme, Italy, May 26 – June 1, 1996.

[73] ZEUS collaboration, Phys. Lett. B363 (1995) 201.

[74] K. Flamm, Ph.D. thesis, Hamburg, DESY FH1-96-04, 1996 (in German).

[75] Ch. Niedzballa, private communication.

[76] Th. Hadig, private communication.

[77] K. Rabbertz, private communication.

[78] A.D. Martin, R.G. Roberts, W.J. Stirling, Phys. Rev. D43 (1991) 3648.

[79] K. Rosenbauer, private communication.

[80] D. Graudenz, M. Hampel, A. Vogt, CERN-TH/96-236, to be published in the proceedings of the workshop "Future Physics at HERA," DESY, Hamburg, 1996.

[81] D. Graudenz, private communication.

[82] A. Vogt, private communication.

Danksagung

An erster Stelle möchte ich Herrn Prof. Dr. Christoph Berger für die intensive Betreuung meiner Dissertation danken. Er hat mich auf ein sehr interessantes Thema aufmerksam gemacht und selbst einen großen Anteil an der erfolgreichen Umsetzung. Andererseits ließ er mir stets die Freiheit, eigene Wege zu gehen und unterstützte dies nachdrücklich.

Herrn Prof. Dr. Sigfried Bethke danke ich für die Übernahme des Korreferates.

Dr. Dirk Graudenz und Dr. Andreas Vogt gebührt mein Dank für ihren theoretischen Beistand und große Kooperations- und Diskussionsbereitschaft. Insbesondere danke ich Dirk Graudenz für das Gegenlesen des Manuskriptes.

Darüber hinaus gilt mein Dank den Mitgliedern der Aachener "QCD-Gruppe" für Ihre Kooperation und die kritische Begleitung des Projektes: Dipl.-Phys. Thomas Hadig, Dipl.-Phys. Christian Niedzballa, Dipl.-Phys. Klaus Rabbertz und Dr. Konrad Rosenbauer.

Außerdem habe ich den "Mitinsassen" unseres Aachener Zimmers am DESY zu danken, die neben einem guten Arbeitsklima durch Hilfsbereitschaft und Diskussionsfreude zum Gelingen dieser Arbeit beigetragen haben: Cand.-Phys. Simone Baer und Dipl.-Phys. Claus Keuker.

Des weiteren haben mir viele Mitglieder des Institutes und der H1-Kollaboration geholfen, von denen hier nur Dr. Albert de Roeck exemplarisch genannt sei.

Meinen Eltern möchte ich für ihre aufopferungsvolle Erziehungsarbeit danken, die mein Interesse an der Physik nicht nur weckte, sondern auch in jeder nur erdenklichen Hinsicht förderte. Leider können Sie dies nicht mehr miterleben.

Nicht zuletzt danke ich der Studienstiftung des deutschen Volkes, die mich sowohl in materieller als auch ideeller Hinsicht während des gesamten Studiums und der Promotion sehr unterstützt hat.

Meiner Frau Susan Kassouf kann ich nicht genug dafür danken, daß sie in dieser schwierigen Zeit die Geduld aufgebracht hat, die nötig war, um eine "transatlantische" Ehe zu führen.

Lebenslauf

15.01.1966	Geboren als erster Sohn des Elektronikers Horst Hampel und der Einzelhandelskaufmannsgehilfin Barbara Hampel, geb. Böhm, in Unna/Westfalen.
1972 – 1976	Besuch der Grillo-Grundschule Unna.
1976 – 1985	Besuch des Geschwister-Scholl-Gymnasium Unna bis zum Abitur.
07/85 – 09/86	Ableistung des Grundwehrdienstes.
10/86	Begin des Physikstudiums an der RWTH Aachen.
04/87	Aufnahme in die Studienstiftung des deutschen Volkes aufgrund eines Schulvorschlages.
10/88	Vordiplom in Physik von der RWTH Aachen.
1989 – 1990	Studium an der State University of New York at Stony Brook im Rahmen eines Fulbright-Stipendiums und eines Stipendiums der Friedrich-Wilhelm-Stiftung der RWTH Aachen. Dort Mitarbeit am D0-Projekt beim Fermilab/Chicago.
20.05.1990	Abschluß des Master of Arts in Physics von der SUNY at Stony Brook.
04/91	Beginn der Diplomarbeit am I. Physikalischen Institut der RWTH und Mitarbeit in der H1-Kollaboration.
27.04.1993	Diplom in Physik von der RWTH Aachen.
05/93 – 12/93	Wissenschaftliche Hilfskraft am I. Physikalischen Institut der RWTH.
Seit 01/94	Promotionsstipendiat der Studienstiftung des deutschen Volkes.